UNIVERSITY OF SOUTHAMPTON
FACULTY OF ENGINEERING, SCIENCE AND MATHEMATICS

School of Ocean and Earth Science

The Role of Diapycnal Mixing in Coupled Atmosphere-Ocean General Circulation Models

by
Clotilde Dubois

Thesis for the degree of Doctor of Philosophy

September 2006

UNIVERSITY OF SOUTHAMPTON

ABSTRACT

SCHOOL OF OCEAN AND EARTH SCIENCE

Doctor of Philosophy

THE ROLE OF DIAPYCNAL MIXING IN COUPLED ATMOSPHERE-OCEAN GENERAL CIRCULATION MODELS

by Clotilde Dubois

The value of ocean diapycnal diffusivity (κ_v) sets the rate at which dense bottom water can be mixed up through the stratified water column and thus plays an important role in the meridional overturning circulation (MOC). Previous idealised experiments and simplified theory suggest that the strength of the MOC and the ocean heat transport scale with the κ_v. This study investigates the dependence of the MOC and other parameters on κ_v using atmosphere-ocean general circulation models (AOGCM).

Firstly, the dependence of the MOC strength on κ_v is studied using a low resolution AOGCM with realistic geometry, FORTE, with spatially constant κ_v values ranging from 0.1 cm^2/s to an unrealistic high value of 5 cm^2/s. At the cyclostationary state, global MOC strength is found to scale with κ_v (in agreement with previous studies) according to a power law of 0.5. No power law is found for the MOC in the individual basins. The increase in MOC strength in the Atlantic and Pacific Oceans is associated with an increase in the ocean heat transport. The atmosphere responds to the change in the ocean state by a decrease of its energy transport and surface winds. Only a partial compensation is found between the ocean and atmosphere energy transport. The strength of κ_v is found to have a strong impact on coupled phenomena, such as a cessation of El Niño at high κ_v.

Secondly, similar experiments are conducted with a state-of-the-art AOGCM, ECHAM5/ MPI-OM. In this model, κ_v is derived from a constant background diapycnal diffusion (κ_b), wind induced mixing, the Richardson number and the convective adjustment. A set of 3 coupled experiments is conducted, with κ_b = 0.1, 0.25 and 1 cm^2/s. The scaling law from simple theory and the previous experiments with FORTE is not observed with this coupled model. At the cyclostationary state, the MOC strength weakens by 16$\%$ as κ_b increases from 0.1 to 1 cm^2/s. This behavior is not found when the experiments are repeated with an ocean-only model. The reduction in MOC in the coupled model is linked to a strong reduction in the convective mixing at high latitudes. The convective mixing is reduced by a continuous strong freshening in the Arctic region due to an increase in surface air temperature and melting of the sea-ice in the coupled experiments, which is not observed in the ocean-only experiments.

The responses of the two coupled models show many similarities as κ_b increases. Both models show convection in the Pacific for high values of κ_b. The main difference is the response of the MOC in the Atlantic is linked to the different locations of the deep convection and their relative changes in the models.

I conclude that the diapycnal mixing and the ocean-atmosphere interactions both control the strength of the MOC, and their influences cannot be considered separately.

Contents

List of Figures

List of Tables

Declaration of authorship

I, Clotilde Dubois, declare that the thesis entitled *"The role of diapycnal mixing in ocean-atmosphere coupled general circulation models"* and the work presented in it are my own. I confirm that:

1. this work was done wholly or mainly while in candidature for a research degree at this University;
2. where any part of this thesis has previously been submitted for a degree or any other qualification at this University or any other institution, this has been clearly stated;
3. where I consulted the published work of others, this is always clearly attributed;
4. where I have quoted from the work of others, the source is always given. With the exception of such quotations, this thesis is entirely my own work;
5. I have acknowledged all sources of help;

6. where the thesis is based on work done by myself jointly with others, I have made clear exactly what was done by others and what I have contributed myself;

7. parts of this work have been published as listed in the references.

   Chapter 4 has been submitted to Climate Dynamics as:

   Dubois, C., Smith, R.S. and Marotzke, J., 2006: Sensitivity to the ocean diapycnal diffusivity in an ocean-atmosphere general circulation model. *Climate Dynamics*, submitted.

Signed :

Date :

Acknowledgements

I would like very much to thank my supervisor, Profesor Jochem Marotzke for his encouragement, advice and support throughout my time in Southampton and in Hamburg and who also gave me the opportunity to go to sea to see how measurements are taken. Many thanks also should go to Dr. Robin S. Smith, who gave me invaluable advice and technical help in particular with the FORTE model, and also was foolish enough to run the Berlin marathon 2005 with me.

Special thanks to the members of my advisory panel: Professor Harry Bryden and Dr. Neil Wells, who ensured that my research project was heading in the right direction even after I moved to Germany. Also many thanks to Professor John Shepherd and Dr. Richard Wood for carrying out my PhD.'s oral examination.

At the National Oceanographic Centre in Southampton, I would like to thank John Stark for setting up the FORTE model and making it more up to date, Dr. Joël Hirschi for his enthusiasm in all aspects of oceanographic problems. Also many thanks to Marc Lucas and Matt Palmer for their friendship and their kindness in proof-reading my thesis.

At the Max Planck Institute in Hamburg, I would like to thank Dr. Johann Jungclaus and Dr. Helmuth Haak for their help with the ECHAM5/MPI-OM model and any questions that I had. Thanks also to all the fellow students and post-docs: Dirk, Felix, Malte, Miren, Robin, Xiuhua and all the others for providing a jovial social environment within and outside the institute.

Special thanks to Fiona McLay who has been in the same boat during my PhD. experience from Southampton to Hamburg and for her relentless contagious enthusiam!

Finally, I would like to thank my mother, my brother and my familly for their support, mostly distant but nevertheless invaluable. And of course many thanks to Michael who walked all this road and future ones with me.

Chapter 1

Introduction

1.1 Climate Dynamics

The climate is a highly complex non-linear system of different processes and feedbacks between its components. The ocean and atmosphere are two fundamental components of the climate system. The interactions between the ocean and the atmosphere, the mechanisms governing them and their stability are important issues in understanding the present climate and its possible changes.

The main external source of energy to the climate system is solar radiation, incident on the top of the atmosphere, which varies with latitude, seasons and solar cycles. The atmosphere is largely transparent to the incoming radiation, therefore most of the heating takes place at the Earth's surface, with greater heating at the Equator and weakening towards the poles. The lower atmosphere is heated at the bottom, which creates large convective cells, with heating and rising of warm air

around the equator. The rising air creates a zone of low pressure at the equator called the equatorial low and Intertropical Convergence zone (ITCZ). The upward motions that dominates the region favor the formation of heavy rain. These convective cells migrate north and south of the equator according to the inclination of the Earth and seasons, with dry air implying high pressure. The colder air from higher latitudes is transported equatorward known as the trade winds. These convective cells are known as Hadley cells, the motion of these cells is affected by the rotation of the Earth and the monsoons (Wells, 1997). Unlike the atmosphere, the ocean is heated from the top which tends to make the ocean very stable vertically, with light warm water at the surface and cold dense water in the deeper ocean. The atmosphere puts the ocean into motion, with windstress at its surface inducing an Ekman transport. The Ekman divergence/convergence influences the density field, which results in a mean circulation through geostrophy. The resulting circulations are the ocean gyres. Intense surface cooling or high salinity can cause convection of dense surface water (Marshall and Schott, 1999). Diffusion and mixing are responsible for the upwelling of deep water to the surface through the stratified thermocline, as well as the wind which causes isopycnals to outcrop to the surface (Webb and Suginohara, 2001).

Both the atmosphere and the ocean redistribute the heat around the globe (figure 1.1). Because energy is transported from the equator to the poles the net outgoing radiation is higher at high latitudes than the incoming radiation. The atmosphere, with very fast motions with timescales of few minutes to a few months, allows the transport of heat from the equator to the poles, under the influence of the Earth's rotation. The ocean, with its high heat capacity, slowly moves heat poleward under the influence of rotation with timescales of a few months to a few centuries. The heat stored in the upper 2.5 m of the ocean is equal to the total heat storage capacity of the whole atmosphere. The huge heat capacity of the ocean reduces the daily and seasonal temperature variability of the atmosphere by heat exchange, as well as acting as a climate buffer on longer timescales. On the long timescales, the top of the atmosphere fluxes are constant and highly symmetric from the equator. The heat is brought poleward by the energy transport from the ocean and atmosphere (figure 1.2). The total energy transport is assumed to be constant and if one energy component becomes larger due to internal variability or external forcing then the other component will weaken to compensate (Bjerknes, 1964). This assumption about the total energy transport is not well understood and is a subject of current

research (Czaja and Marshall, 2006).

Each component has internal modes of variability such as multi-decadal oscillations of the thermohaline circulation (THC) in the ocean (Delworth et al. (1993) and Delworth and Greatbatch (2000)) or the Quasi-Biennual Oscillation in the atmosphere (Gray, 1984a). The coupled system are also exhibits modes of variability which interact with each other through momentum, heat and freshwater fluxes, such as El Niño phenomena (Philander, 1990) or the North Atlantic Oscillation (NAO) (Hurrell et al., 2003b). Understanding these modes of variability is an active domain of climate research necessary to separate the natural variability of the climate system from the anthropogenic signal.

1.2 Ocean Circulation

The ocean circulation consists of two main motions, as described by Wunsch (2002). The first motion is driven by the wind in the upper ocean, which is also responsible for the surface currents. The windstress (force per unit area exerted by the wind on the ocean), due to the mainly zonal motion of the atmosphere above each ocean basin, results in shallow horizontal ocean recirculations known as gyres, with strong and narrow western boundary currents. The western boundary currents in the northern hemisphere are known as the Gulf Stream and the Kuroshio currents in the North Atlantic and North Pacific respectively. Figure 1.4 illustrates the ocean surface circulation in a simplified drawing. In 1947, Sverdrup (1947) calculated that the circulation in the upper ocean is proportional to the curl of the wind stress. Later, Stommel (1948) calculated the steady-state solutions for a flow in a rectangular basin adding a friction term and assuming that the Coriolis force varies with latitude. The solution is assymetric with a western intensification, and Stommel suggested that it could explain why the Gulf Stream is found in the Atlantic. The wind can also drive strong circulations in the absence of any boundaries, such as around the Antarctic continent, where the Antarctic Circumpolar Current (ACC) is found.

The second motion is a downward motion from the surface to the deep ocean found only at high latitudes in the North Atlantic and Southern Ocean. These regions are associated with strong heat loss to the atmosphere, where dense water

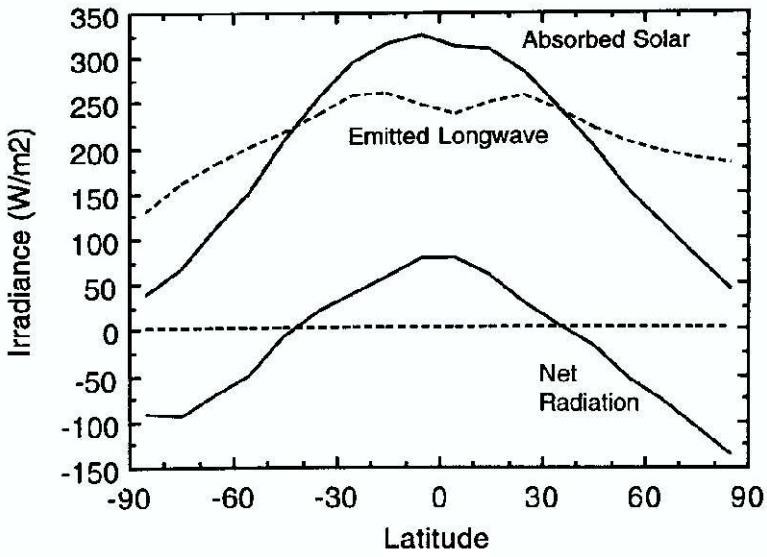

Figure 1.1: *Radiative balance of the Earth for each latitudes from Gill (1982)(Chap.*1*). The upper solid curve shows the average flux of solar energy reaching the outer atmosphere. The dashed line shows the average amount of outgoing radiation. The lower solid curve shows the difference between the shortwave solar energy and the emitted longwave. Values are in* W/m^2*.*

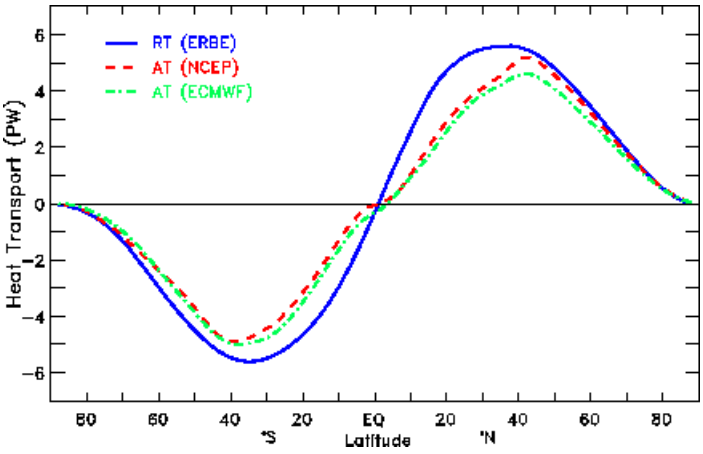

Figure 1.2: *The total energy transport derived from the top of the atmosphere (TOA) radiation (in blue), along with the estimates of the total atmospheric transport from NCEP (in red) and ECMWF reanalysis (in green) in PW from Trenberth and Caron (2001).*

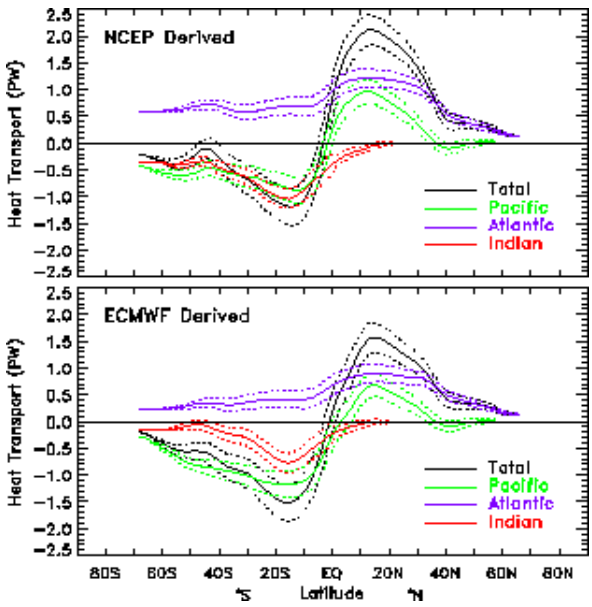

Figure 1.3: *Implied zonal averaged transports based upon the surface fluxes for February 1985 to April 1989 for the total Atlantic, Indian and Pacific basin for NCEP and ECMWF atmospheric fields in PW. One standard error bars are indicated by the dashed curved from Trenberth and Caron (2001).*

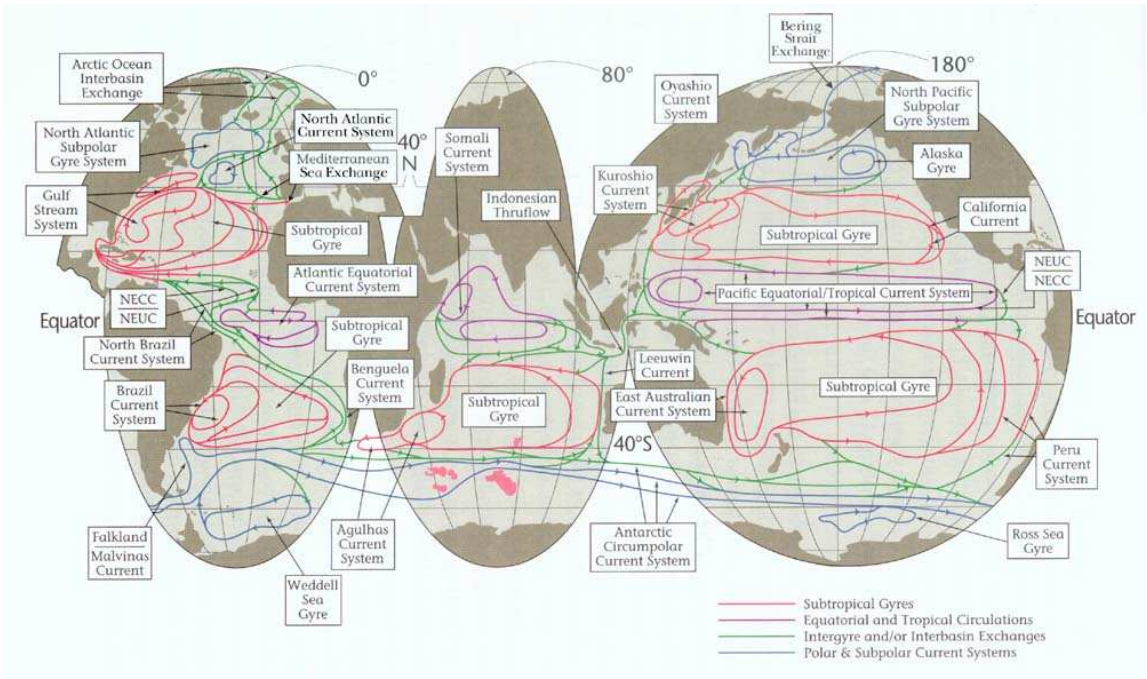

Figure 1.4: *Surface current circulation in the different ocean basins, from Schmitz (1996).*

is formed and descends through convection. The deep water formed in the North Atlantic is called the North Atlantic Deep Water (NADW) and flows to the south as a deep western boundary return current at a depth of 2000 m and upwells in the rest of the oceans. The lower salinities in the Pacific prevent deep sinking in the North Pacific (Warren, 1983). Antarctic Bottom Water (AABW) is formed in the Southern Ocean, mainly in the Weddell Sea by strong heat loss and brine rejection as surface water freezes and flows northward as the deepest water in the Atlantic, Pacific and Indian Oceans. Gordon (1986) and Broecker (1991) popularised the notion that the Atlantic overturning is part of a great conveyor belt or ocean circulation called today the meridional overturning circulation (MOC), spread across the Atlantic, Indian and Pacific Oceans, as illustrated in a cartoon drawing in figure 1.5. The MOC is the zonally integrated flow. They suggest that the conveyor is mainly driven by a build up of salt and heat loss in the surface water of the North Atlantic. This theory suggests that the Atlantic overturning circulation is driven by a north-south density gradient created when the North Atlantic's salty surface water is cooled in the high northern latitudes. The density forced flow is known as the Thermohaline Circulation (THC). The THC and the Ekman circulation together form the MOC.

The northward surface current in the Atlantic and other ocean basins are responsible for ocean heat transport. In the Atlantic Ocean a maximum of about 10^{15} W of heat is transported to the north of the Atlantic ocean, through its northward transport of warm tropical waters by the Gulf Stream and North Atlantic Current. This northward heat transport in the Atlantic contributes to the warming of Northern Europe (figure 1.3). The stability of the heat transport is important in the context of future and/or abrupt climate change (Manabe and Stouffer, 1994; Broecker, 1997; Alley et al., 2003). This could have strong impacts on the climate, ecology and economy of the countries surrounding the North Atlantic.

1.2.1 The Buoyancy-Driven Circulation.

The driving force of the THC is the combined heating/cooling and freshwater fluxes known as buoyancy forcing. In the current regime, the thermal forcing dominates the haline forcing, and the ocean system can be mainly treated as a heat engine. The first person to examine the ocean as a heat engine was Sandström, who conducted a series of laboratory experiments with thermal forcing at different levels (Sandström, 1908; 1916). He concluded that:

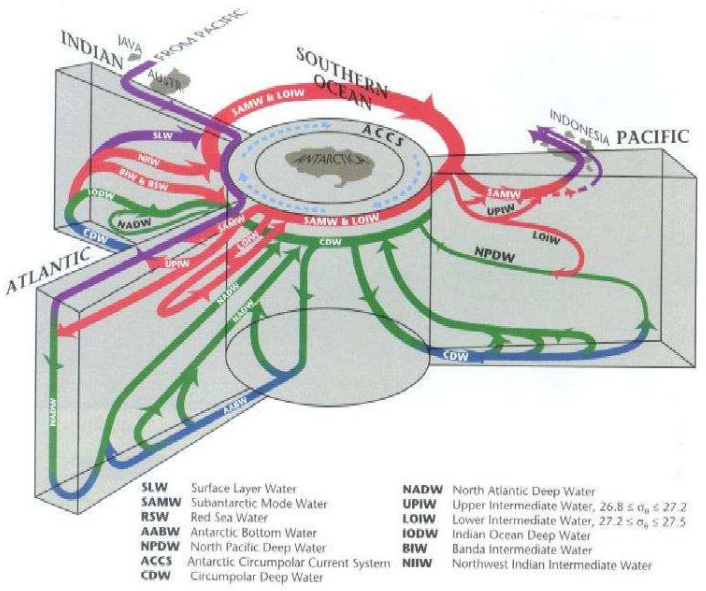

Figure II-8: A three-dimensional interbasin flow schematic with "typical" meridional–vertical sections for the indicated oceans, and their horizontal connections in the Southern Ocean and the Indonesian Passages. The surface layer circulations are in purple, intermediate and SAMW are in red, deep in green, and near bottom in blue.

Figure 1.5: *3-D meridional overturning circulation in the different basins from Schmitz (1996).*

"a closed steady circulation can only be maintained in the ocean if the heat source is situated at a lower level than the cold source." (Sandström, 1908)

Considering the structure of the ocean with the heating source at the tropics, energy from the surface would not be able to maintain a vigorous overturning. These conclusions are valid also for a pure haline flow and forcing. Sandström's error was the lack of significant diffusion and friction in his idealised physical setup. Jeffreys (1925) discussed the validity of Sandström's theorem in the context of the general circulation. He found that if diffusion terms are considered, a circulation can be induced even if the heat source is situated at a higher level than the cold source. In 1961, Defant (1961) concluded that the ocean does not satisfy the conditions of having a deeper heat source in equatorial regions and therefore the thermohaline circulation must be limited to the top layer of the ocean. Colin de Verdiere (1993) and Huang (1999) found that the circulation is controlled by mixing when the heat source is above the level of the cooling.

Significant changes in the strength of the Atlantic THC have been inferred from paleodata (McManus et al., 2004). It has been predicted that, under CO_2 increase,

the freshwater distribution could be severely altered and a slowdown or, in extreme scenarios, a shutdown of the northward heat transport in the Atlantic might result (Manabe and Stouffer, 1994; Houghton et al., 1996; Cubasch et al., 2001; Vellinga and Wood, 2002).

The stability of the THC has attracted a lot of attention in the last few decades in the literature. Broecker et al. (1985) suggested from paleorecords that the deep ocean circulation could switch from an *"on"* mode (present circulation) to an *"off"* mode (no circulation) under changes of the freshwater input at high northern latitudes. Multiple equilibrium states for the MOC were found by Stommel (1961) under same surface boundary conditions in a simple two box model, with each box taken to have its own temperature and salinity. Stommel's imaginary laboratory setup avoids the cold water reaching the deep ocean to completely fill the abyssal ocean all the way to the surface. Wunsch and Ferrari (2004) suggested that the ocean circulation, instead of being a heat engine, is governed by energy dissipation from the forcing of the wind field and deep water tides.

1.3 Mixing

1.3.1 Diapycnal Mixing

For both the buoyancy-driven and wind driven circulation, diapycnal mixing plays an important role in determing the stratification of the present oceanic structure by providing vertical displacement which works against the buoyancy force. The diapycnal mixing is the amount of mixing between two layer of different density. The more stable the water column is, the more energy is required by vertical mixing to break down that stratification. The diapycnal mixing controls the rate at which deep water eventually reaches the surface at mid and low latitudes. In the ocean, mixing by eddies is more important than molecular diffusion (Munk, 1966). In models, this is parameterised by the vertical eddy diffusivity, denoted by κ_ν. The equation of a tracer (temperature or salinity) for vertical diffusivity by eddies for each water parcel is:

$$\frac{\partial T}{\partial t} + w\frac{\partial T}{\partial z} = \frac{\partial}{\partial z}\left(\kappa_\nu \frac{\partial T}{\partial z}\right) + S \tag{1.1}$$

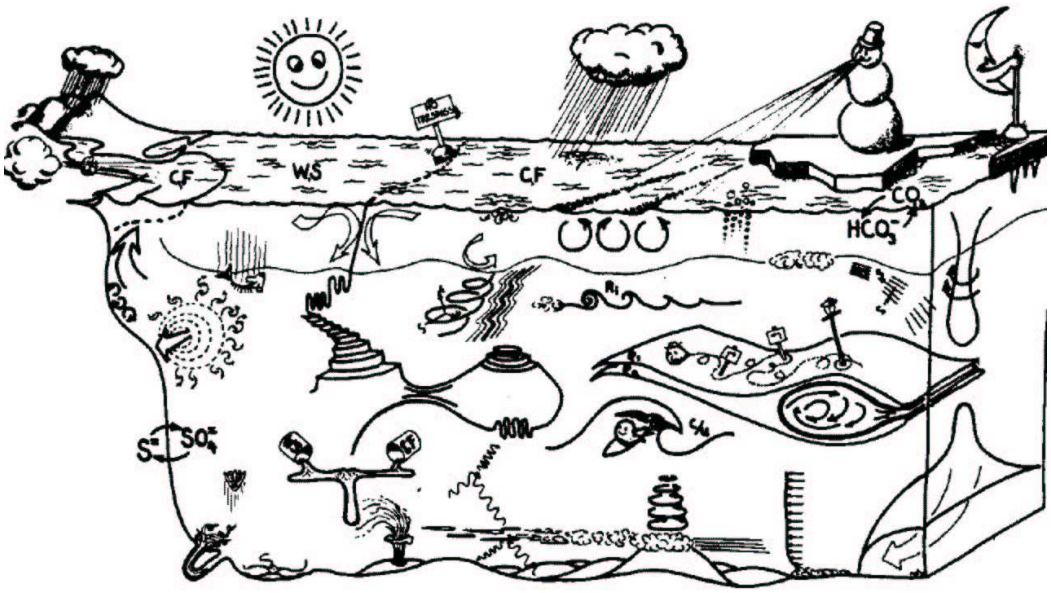

Figure 1.6: *Different mixing processes in the ocean, cartoon by Greg Holloway.*

Where, T is the tracer, κ_ν is the vertical diffusivity and S is a source term, w is a vertical velocity, t is the time and z is the vertical axis.

1.3.2 Sources of Mixing

The processes responsible for the small scale mixing in the ocean are numerous and occur at different locations and depths. Their relative contributions are not clear as potential candidates to close the THC (Munk, 1966) (figure 1.6). This cartoon suggests potential candidates, such as double diffusion, unstable mean shears, entrainment through gravity waves in the depth ocean, windstress at the surface, laminar flows, tidal energy, eddies, Kelvin-Helmholz instability, Ekman pumping, fronts and the breaking of internal waves or also processes like double-diffusive instabilities (e.g., (Toole and McDougall, 2001)) and tropical cyclones (Nilsson (1996) and Emanuel (2001)). Munk and Wunsch (1998) suggested that enhanced tidal turbulent mixing near bottom topography and winds are the main source of abyssal mixing and that their contribution can resolve the "missing energy problem" (Wunsch, 1998) (figure 1.7). They calculated that 2.1 TW (terawatt=10^{12}W) are required to maintain the global abyssal density distribution and upwell the 30 Sv of deep water formed. About half of this source, 0.6 to 0.9 TW, comes from the tidal dispersion

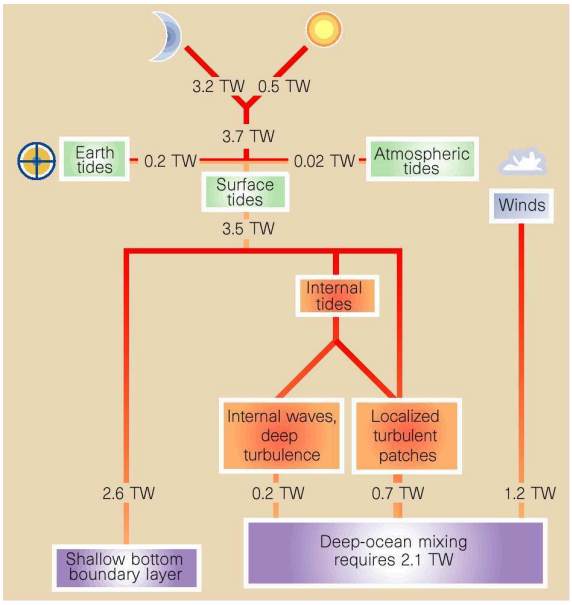

Figure 1.7: *A budget of tidal and wind energy input fluxes as generator of internal waves from Munk and Wunsch (1998).*

available for abyssal mixing; this has been confirmed by altimetry data (Egbert and Ray, 2000). The second half of this source, 1 TW, comes from wind-driven mixing power. Webb and Suginohara (2001) proposed a smaller value of the total energy of 0.6 TW, as between 9 and 12 Sv of deep water is brought to the surface by Ekman pumping in the Southern Ocean. They argued that since the slope of the isopycnals is usually small (no outcrop appears from below 1300 m) the AABW only needs to mix up to mid depth and not to the surface before being upwelled by the ACC to the surface. The energy needed for this is 0.6 terawatts and this reduces the global average diapycnal mixing to 0.3×10^{-4} m^2/s, far less than the values found by Munk and Wunsch (1998). All these different sources of energy are very difficult to parameterise in a model. Recently, Simmons et al. (2004) tested the effect of tidal energy budget on the MOC in a global ocean. Their energy flux estimates agreed well with independent estimated observations for generation sites for tidal energy.

1.3.3 Estimates of Mixing

The great difficulty of adequately sampling the ocean in situ means that data are very limited in time and space, and estimated values of κ_v vary in order of magnitude. Not enough observations of the diapycnal diffusivity are available to form a global map and a great uncertainty of the strength of the diapycnal mixing in the real ocean still remains.

Munk (1966), in his classic paper, used observations of vertical distribution of ^{14}C in the Pacific to suggest that the thermocline depth has not changed over time and can be considered to be in a steady state. He suggested that the temperature and salinity can be fitted by exponential-like solution when the top and bottom kilometre is excluded and one can assume a constant upward velocity (w). Therefore the equation 1.1 in the thermocline can be written in a steady state as:

$$w\frac{\partial T}{\partial z} = \kappa_v \frac{\partial^2 T}{\partial z^2} \tag{1.2}$$

Where, w is the vertical velocity, κ_v is the diapycnal mixing, T is the tracer (in this case Munk (1966) used the temperature) and z is the vertical axis.

In the ocean interior, the upward transport of heat by the vertical current w is balanced by the downward mixing of heat by the eddies. Munk estimated the vertical mixing of $1.3 \times 10^{-4}\ m^2/s$ for the global ocean, which is now taken as the canonical value of κ_v=1 cm^2/s. Similar values $\mathcal{O}(10^{-4}m^2/s)$ have been found when spatially averaged density is considered (Munk and Wunsch, 1998).

This value is only an average and does not reflect the spatial variability obtained from direct measurements at different locations. Very little mixing is observed in the thermocline - $\mathcal{O}(10^{-5}m^2/s)$, while values - $\mathcal{O}(10^{-4}m^2/s)$ and higher - of mixing have been measured near rough topography (Polzin et al., 1997). The different direct measurements in the ocean obtained at different locations are shown in table 1.1. It can be concluded that κ_v has a strong spatial dependence and is linked to the topography, as mentioned in early papers by Munk (1966) and Armi (1978). Munk (1966) suggested that mixing is enhanced near the continental margins and bottom boundaries by the dissipation of tidal and wind energy (Munk and Wunsch, 1998; Wunsch, 1998; Naveira Garabato et al., 2004).

Location	Value of $\kappa_v(10^{-4}m/s)$	Method
Ocean interior (Brazil Basin, South Atl.) (Polzin et al., 1997)	0.1	ocean microstructure data
Abyssal Ocean (Toole et al., 1994)	0.1	ocean microstructure data
Atlantic North Abyssal (Whitehead and Worthington, 1982)	$1-4$	
Atlantic North Abyssal (Saunders, 1987)	$1-4$	-
Atlantic North (Ledwell et al., 1993)	0.1	Direct tracer dispersion
Mid-Atlantic ridge (Polzin et al., 1997)	5	
Atlantic (bottom) (Ganachaud and Wunsch, 2000)	9 ± 4	inverse model
Atlantic (deep) (Ganachaud and Wunsch, 2000)	3 ± 1.5	inverse model
Pacific (bottom) (Ganachaud and Wunsch, 2000)	9 ± 2	inverse model
Pacific (deep) (Ganachaud and Wunsch, 2000)	4 ± 1	
Indian Basin (McCarthy et al., 1997)	35 ± 14	
Indian (bottom) (Ganachaud and Wunsch, 2000)	12 ± 7	
Indian (deep) (Ganachaud and Wunsch, 2000)	4 ± 2	
Brazil Basin (Hogg et al., 1982)	$3-4$	
Brazil Basin (Durrieu de Madron and Weatherly, 1994)	$3.6-7.2$	
Brazil Basin (Ledwell et al., 2000)	$2-4$	
Brazil Basin (Morris et al., 2001)	3 ± 2	
Samoan Passage (Roemmich et al., 1996)	$50-500$	
Somali Basin (Barton and Hill, 1989)	10.6 ± 2.7	
Amirante trench: Discovery Gap (Saunders, 1987)	$1.5-4$	
Romanche Fracture Zone (Ferron et al., 1998)	100	
Southern Ocean: Scotia Sea (Heywood et al., 2002)	39 ± 10	

Table 1.1: *Estimated values of the diapycnal mixing from observations.*

1.4 Scaling Argument

Early work on relating the strength of the circulation to the vertical diffusivity was done by Robinson and Stommel (1959) and Welander (1971). Consider a simple ocean basin with no wind stress where the meridional overturning circulation is driven by the zonal surface density gradient: $\Delta\rho$. An expression for the thermocline depth D can be obtained from the following equations:

Thermal wind relation for the zonal flow which was found to hold for the zonally averaged meridional flow (Bryan, 1987).

$$f\frac{\partial v}{\partial z} = -\frac{g}{\rho_0}\frac{\partial \rho}{\partial x} \tag{1.3}$$

Where, $\Delta\rho$ is the equator to pole density difference, z is the vertical height, x is the horizontal size, ρ_0 is the reference density, f is the Coriolis parameter, g is the gravitational acceleration.

Scaling to:

$$\frac{V}{D} \sim \frac{g}{f\rho_0}\frac{\triangle\rho}{L} \tag{1.4}$$

Where, D is the thermocline depth, L is the horizontal length, v is the horizontal velocity,

The thermal wind relation depends on zonal rather than meridional density gradients. This scaling implies the assumption that there is a linear relation between the velocity for the zonal and meridional directions. Marotzke (1997) showed analytically that this was the case which was confirmed by Park and Bryan (2000) in numerical experiments. The meridional density gradient is prefered as it is more sensitive to heat transport changes and changes in sea surface temperature due to climate change.

The flow at the boundary layer has horizontal advection compensated by vertical advection (if the horizontal diffusion is negligible):

$$\frac{\partial v}{\partial y} = -\frac{\partial w}{\partial z} \tag{1.5}$$

Where, w is the vertical velocity, y is the horizontal size.

Scaling to:

$$\frac{V}{L} = \frac{W}{D} \tag{1.6}$$

and from the vertical advective-diffusive balance below the thermocline

$$w\frac{\partial \rho}{\partial z} = \kappa_v \frac{\partial^2 \rho}{\partial z^2} \tag{1.7}$$

Where, κ_v is the vertical diffusivity.

Scaling to:

$$W = \frac{\kappa_v}{D} \tag{1.8}$$

The previous equations can be rearranged and give the following expressions for:

$$W = \kappa_v^{\frac{2}{3}} \left(\frac{g\Delta\rho}{f\rho_0 L^2} \right)^{\frac{1}{3}} \tag{1.9}$$

$$D = \kappa_v^{\frac{1}{3}} \left(\frac{f\rho_0 L^2}{g\Delta\rho} \right)^{\frac{1}{3}} \tag{1.10}$$

The THC can be defined as the overturning streamfunction, ψ which is scaled in the meridional vertical section as:

$$\Psi = VDL = wL^2 = \kappa_v^{\frac{2}{3}} \left(\frac{g\Delta\rho L^4}{f\rho_0} \right)^{\frac{1}{3}} \tag{1.11}$$

Assuming that the meridional velocity is proportional to the zonal velocity.

Numerical simulations have been done to test the dependence of the strength of the MOC on the vertical mixing. Using an OGCM, Bryan (1987) confirmed that the THC strength is sensitive to the mixing. He varied κ_ν from 0.1 to 5×10^{-4} m^2/s and found a power dependence of the $\psi \propto \kappa_\nu^{1/3}$. Later, sensitivity experiments carried out by Marotzke (1997), Zhang et al. (1999), and Park and Bryan (2000) in single hemisphere OGCMs with idealised configurations found a power dependence where

$\psi \propto \kappa_\nu^{2/3}$ in agreement with their scaling arguments. In other experiments, however, Wright and Stocker (1992) and Weber (1998) found a dependence where $\psi \propto \kappa_\nu^{1/2}$. So far, little attention has been paid to whether the scaling argument applies in models which are fully coupled to the atmosphere and/or with realistic topographies. In particular, models with an ACC which allows a wind induced upwelling of deep water have not been used (Gnanadesikan, 1999; Wright and Stocker, 1992). There has been one recent study with two ocean basins and a $2-D$ atmosphere (Dalan et al., 2005). He found that the overturning in the Atlantic does not scale to the power $\psi \propto \kappa_\nu^{2/3}$, whereas the Pacific basin seems to.

The meridional heat transport by the Atlantic ocean can be estimated through the contribution of the meridional overturning and can be written as:

$$HT = \rho C_p \Psi \Delta T \tag{1.12}$$

Where, HT is the meridional heat transport, C_p is the specific heat at constant pressure, ΔT is the temperature difference between the surface and deep equatorward MOC branch.

Scott (2000) highlighted that the D used in the scaling laws of the different equations represents both the depth of the level of no-motion for the thermal wind equation and the base of the thermocline for the advection-diffusion balance. These assumptions are thus, not justified and are inconsistent. Furthermore, depending on the authors, the depth of the thermocline is found to be calculated using different equations. Bryan (1987) computed an e-folding thermocline depth ($\sigma_\theta(ze)$) defined from the potential density at each location by:

$$\sigma_\theta(ze) \equiv \sigma_\theta(-H) + [\sigma_\theta(0) + \sigma_\theta(-H)]/e \tag{1.13}$$

Where, σ_θ is the potential density and H the depth at the bottom.

In contrast, Park and Bryan (2000) computed a weighted thermocline depth by:

$$\delta_T(x,y) = \frac{\int_{-H}^{0}(T - T(-H))z dz}{\int_{-H}^{0}(T - T(-H))dz} \tag{1.14}$$

Park and Bryan (2000) showed that the basic assumption behind the thermocline scaling is that an increase in the vertical diffusion only changes the vertical scale of

the thermocline and that the horizontal patterns are self-similar. This implies that the zonal and meridional pressure gradients are proportional.

Other hypotheses have been proposed that the mixing is not the only parameter controlling the thermohaline circulation and advance instead the role of the ACC. In a model, Toggweiler and Samuels (1995; 1998) found that the production of NADW scales with the strength of the wind forcing of the ACC and the rate of upwelling south of the ACC. In regions of strong Ekman transport in the Southern Ocean, deep water masses can upwell along the isopycnal slope, therefore the vertical mixing might not be so important if the large-scale overturning is linked to the ACC (Toggweiler and Samuels, 1998). However Toggweiler and Samuels (1995; 1998) calculated the upwelling in the Southern Ocean by using a horizontal/vertical mixing parameterisation in an ocean model which induces extra diapycnal mixing in regions of sloping isopycnals such as the ACC. Toggweiler and Samuels (1995; 1998) and Webb and Suginohara (2001) showed the importance of the Southern Ocean Ekman pumping due to the absence of geostrophy.

Gnanadesikan (1999) proposed another relationship between the depth of the thermocline and Northern sinking, low latitude upwelling, Southern Ocean winds, eddies and diapycnal diffusivity. The upper Southern Ocean at the latitude of the Drake Passage is composed of a northward Ekman transport driven by the wind and a return flow by mesoscale eddies. The strength of the upwelling in the Southern Ocean is determined by the windstress at this latitude and the eddy transport across the ACC. The transport flux out of the Southern Ocean (T_S) is written as:

$$T_s = (\frac{\tau}{f\rho_o} - \frac{A_I}{L_y^s})L_x \tag{1.15}$$

Where, L_x is the circumference of the Earth at the latitude of Drake Passage, L_y^s is the north-south distance over which the gradient in layer depth in the southern hemisphere, τ is the wind stress in the Southern Ocean, f is the Coriolis parameter and A_I is the diffusion coefficient.

It should be noted that this equation assumes that all the northward transport in the Southern Ocean goes into the Atlantic basin even if the Ekman transport in the Southern Ocean also happens and goes to the Indo-Pacific Ocean. The other transport fluxes are the downwelling water in the north, which travels southward and upwells later in the Southern Ocean and at low latitudes throughout the thermocline.

A cubic equation can thus be obtained for the thermocline depth D - this relates the strength of the NADW to the diapycnal diffusivity κ_v and the wind contribution in the Southern Ocean (Ekman transport minus an eddy transport:

$$\kappa_\nu A = \frac{Cg}{L_y^n} D^3 + \frac{A_I L_x}{L_y^s} D^2 - \frac{\tau L_x}{\rho f} D \tag{1.16}$$

Where, A is the surface area of the low-latitude box, g is the reduced gravity, L_y^n is the north-south distance over which the gradient in layer depth in the northern hemisphere and C is a constant that incorpporates effects of geometry and boundary layer structure.

These scaling arguments are idealised and it is not clear whether they are applicable in a multi-basin setup with a full wind forcing over all of the basins and at all latitudes (not only the ACC region). Furthermore, the scaling analysis only considers a circulation with sinking at high latitudes and upwelling into the thermocline at low and mid-latitudes. The scaling has only been observed in models with a single ocean basin without Drake Passage or an ACC; this configuration forces the overturning to downwell at high northern latitudes and upwell at low and mid latitudes as this is the only pathway available. Whatever the driving force of the MOC is, the diapycnal mixing still plays an major role in the configuration of the ocean as we see it today (Klinger et al., 2003).

1.5 This Study

Great progress has been made in understanding the role of small- and meso-scale processes in the large-scale structure and circulation of the oceans. The diapycnal diffusivity is usually assigned *ad hoc* in simple, global ocean models, as a means of tuning the ocean model to observed meridional heat and mass transports. However, the sensitivity of the large-scale ocean and climate to the strength of the mixing remains poorly known. So far, most previous studies of the sensitivity of the climate system to the diapycnal ocean diffusivity restore surface temperatures to climatology, which does not allow for much feedback between the model overturning and surface temperature. Also, until recently, most ocean models used a constant value over the ocean basin for κ_v, which is far from what is observed in the ocean. The values

used in different ocean models vary from 0.1 to 20 cm^2/s as the vertical diffusitivity is usually tuned so that the ocean model reproduces an ocean state close to reality (e.g. Coupled Model Intercomparison Project, CMIP). Ocean models run without an interactive atmosphere misses important air-sea interaction processes which can significantly affect deep water formation and heat transport. Previous studies such as Weber (1998); Dalan et al. (2005); Mignot et al. (2006) used simplified atmosphere models or idealised topography. Specifically, the objectives of this study are:

1. To systematically examine the sensitivity of the climate system to a uniformly distributed κ_ν in a coarse resolution atmosphere-ocean general circulation model (AOGCM) over long integration periods.

2. To examine the coupled feedbacks on κ_ν in a state-of-the-art coupled AOGCM.

In Chapter 2 the two different models used are described, with an emphasis on the differences in the parameterisation of κ_v.

In Chapter 3 the spin-up done for each experiment are described. The fundamental properties of the model control climate and some of the modes of variability in the control runs are compared to observational data.

In Chapter 4, the sensitivity experiments using FORTE, a coarse resolution AOGCM model from the National Oceanography Centre, Southampton are analysed as κ_ν is varied between 0.1 and 5 cm^2/s.

In Chapter 5, the sensitivity experiments using the state of the art ECHAM5/MPI-OM model in a coupled and ocean-only set-up are described. The representation of the vertical diffusivity parameterisation is more realistic and only the κ_b is changed.

In Chapter 6, a summary, discussion and conclusions of the results is given and possible future work is presented.

Chapter 2

Models

This chapter introduces the two different models used in this study. Both models are coarse resolution coupled atmosphere-ocean general circulation models (AOGCMs). An important difference between them is the parameterisation of oceanic diapycnal mixing.

2.1 FORTE

The low resolution FORTE (Fast Ocean, Rapid Troposphere Experiment) model has been developed at NOCS (National Oceanography Centre, Southampton) by Bablu Sinha and Robin Smith (Sinha and Smith, 2002; Smith, 2004). It consists of an ocean and an atmosphere General Circulation Model (GCM). The ocean model is MOMA, a version of MOM: Modular Ocean Model (Pacanowski and Griffies, 1998) optimised for array computers (Webb, 1996). The atmosphere model is IGCM3: Intermediate

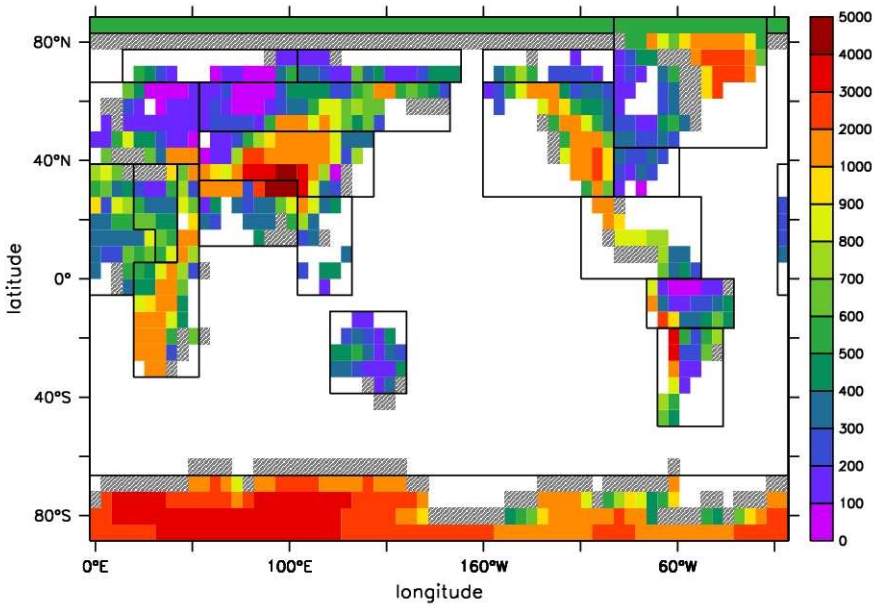

Figure 2.1: *Map showing the IGCM3 orography (color scale, in meters), the run-off catchment (black boxes) and the dumping run-off zones in the ocean for each catchment areas (grey shaded) (Smith, 2004).*

GCM version 3 (Forster et al., 2000). MOMA and IGCM3 are coupled together using OASIS (Ocean Atmosphere Soil Ice System) (Terray et al., 1999), which allows the models to pass data information between each other when running. At each time step, the ocean passes its sea surface temperature (SST) field to the atmosphere, which passes to the ocean its heat flux, (shortwave, longwave, latent and sensible) windstress and a freshwater flux fields, calculated in response to the SST field from the previous coupling step. A land tiling scheme is added to correctly match the different ocean and atmosphere grids to each other and to ensure conservation of energy. The runs are done with a topography derived from the US Naval 1/6° dataset, the surface topography of the model on the atmospheric grid is shown in figure 2.1.

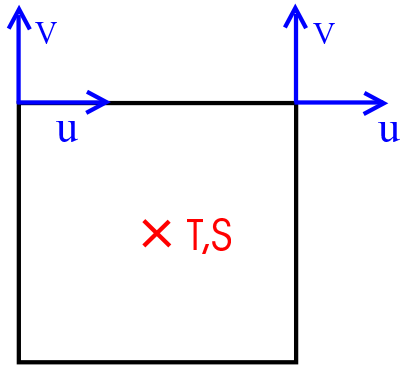

Figure 2.2: *Schematic of the Arakawa B grid used in the FORTE model. The velocity vectors u, v are situated at each corner of the grid box, and the tracers T, S are situated in the centre of each grid box.*

2.1.1 MOMA

The ocean model is MOMA (Webb, 1996), an array version of the widely used the Modular Ocean Model (MOM) code (Pacanowski and Griffies, 1998) which is based on the GFDL (Geophysical Fluid Dynamics Laboratory) code (Bryan, 1969; Semtner, 1974).

The *"primitive equations"* describe the time evolution of the ocean state based on the Navier-Stokes equation for fluid flow with the following assumptions.

1. Mass conservation
$$\nabla \cdot \mathbf{u} + \frac{\partial w}{\partial z} = 0 \tag{2.1}$$
where $\mathbf{u}$ is the horizontal velocity, w is the vertical velocity and z is the vertical height.

2. The vertical velocities are far smaller than horizontal ones, and the vertical accelerations can be neglected.

3. Boussinesq approximation: the density is nearly constant in the ocean except when it is multiplied by g in calculations of pressure in the ocean (g the gravitational acceleration (about 9.8 m/s^2)).

These assumptions give the following equations in numerical model from Bryan (1969) and describing the evolution of horizontal momentum and tracer fields:

$$\frac{\partial \mathbf{u}}{\partial t} + (\mathbf{u} \cdot \nabla)\,\mathbf{u} + w\frac{\partial \mathbf{u}}{\partial z} + f \times u = -\left(\frac{1}{\rho_0}\right)\nabla p + D_u + F_u \tag{2.2}$$

$$\frac{\partial \Theta}{\partial t} + (\mathbf{u} \cdot \nabla)\,\Theta + w\frac{\Theta}{\partial z} = D_\Theta + F_\Theta \tag{2.3}$$

Where, Θ is the tracer (potential temperature T or salinity S), f is the Coriolis parameter, p is the pressure, t is the time, D_u and D_Θ are a diffusion term and F_u and F_Θ are the external forcing. ρ is the density taken to be a function of model pressure, temperature and salinity according to the equation of state polynomial defined by the Joint Panel on Oceanographic Tables and Standard UNESCO (1983).

These equations are integrated forward in discrete timesteps. Further improvements such as a free surface scheme (Griffies et al., 2001) have been made. The use of the free surface scheme requires the use of short timesteps to resolve the gravity waves.

MOMA uses an Arakawa B grid (Arakawa, 1966; Mesinger and Arakawa, 1976). The model is divided into boxes along longitude, latitude and depth, where the vectors u, v are placed at each corner of each box along the latitude and longitude axis and the tracer T, S are placed at the centre of each box, as shown in figure 2.2. This grid scheme is often used in coarse resolution models because of its better representation of Rossby wave propagation, if the grid spacing is greater than the Rossby radius (Griffies et al., 2000). In the present study, MOMA is used in a coarse resolution setting with a $4^\circ \times 4^\circ$ horizontal grid with 15 vertical levels.

A simple sea ice model is included in MOMA. When the temperature of the ocean drops to -1.96°C (the freezing temperature of sea water for an average salinity of 35 PSU at the ocean surface), a 2 m layer of ice forms. The heat capacity and the albedo change accordingly and insulate the polar oceans from $\leq$ -1.96°C air temperatures. The freshwater forcing is kept as before: precipitation falling on the sea ice is passed directly to the ocean. As long as the sea ice is present, there is no heat flux exchange between the ocean and the atmosphere.

Parameter control run	Values (cm^2/s)
Isopycnal tracer diffusivity	2×10^7
Isopycnal thickness diffusivity	2×10^7
Horizontal eddy viscosity	1×10^9
Diapycnal eddy viscosity	20
Diapycnal diffusivity	1

Table 2.1: *Mixing parameters in MOMA used in the control run.*

Mixing in MOMA

An area of great scientific effort is the parameterisation of small scale processes in numerical global ocean models. The simplest choice of a mixing scheme in a z-coordinate model is along the vertical/horizontal axes, which, at the resolution used in this study, does not represent the small scale mixing features well. The choice of vertical/horizontal mixing scheme leads to extra, artifical mixing across sloping isopycnals (as mixing in the real ocean tends to be along isopycnals and not through them (Veronis, 1975)). The vertical/horizontal diffusion mixing scheme in MOMA has been changed to the more realistic isopycnal scheme of Redi and Gent and McWilliams (Redi, 1982; Gent and McWilliams, 1990; Gent et al., 1995). The Gent-McWilliams (GM) parameterisation also includes an explicit parameterisation of the eddy transports, which are not otherwise represented in coarse resolution models such as FORTE. The use of the isopycnal mixing parameterisation gives a better representation of the ocean when compared to observations (Danabasoglu and McWilliams, 1995). It usually results in colder bottom temperature, as less heat from the surface diffuses down, and a sharper thermocline than models with vertical/horizontal mixing, as a consequence of the reduced diapycnal mixing (Kamenkovich and Sarachik, 2004).

The parameter values chosen for the GM parameterisation are shown in table 2.1. These values are uniform over the ocean basin, although in reality mixing is far from uniform (e.g. Ledwell et al. (2000)). This is an important source of error in the model.

Convective adjustment

The convective adjustment of the water column towards static stability uses the simple Cox scheme (Cox, 1984), whereby homogenisation between two vertically

adjacent boxes occurs when they are unstable. For a finite number of passes over the water column, this scheme cannot be guaranteed to converge to a gravitionally stable column (Marotzke, 1991). FORTE uses only one pass through the water column, for reasons of computational affordability.

2.1.2 IGCM3

The atmosphere model is Version 3 of the Intermediate General Circulation Model (IGCM3), developed at Reading University (Hoskins, 1975; Forster et al., 2000). It is a primitive equation spectral atmosphere model. It has a multi-band radiation scheme which includes the effects of water, carbon dioxide and ozone, a cloud parameterisation with five cloud types and uses a convective adjustment scheme based on Betts (1986). The cloud parameterisation has five distinct cloud types (Slingo, 1987), the cloud fraction of three of them is calculated on exceeding a critical value of relative humidity at either low (σ>0.7), middle (0.35<σ<0.7) or high (σ<0.35) altitudes. The 4^{th} type, deep convective cloud is parameterised from precipitation rates and the last type, shallow convective cloud, is set to a low constant value based on climatology. The cloud particle size is set to an average, constant value. The CO_2 concentration is constant, at 358 ppm. The solar short wave radiation repeats a single annual cycle which is give daily values with no diurnal cycle. The solar short wave forcing at the top of the atmosphere stays the same in all the different experiments. A land surface scheme is incorporated which is able to hold moisture and to track soil temperature. The surface is assigned a roughness length and an albedo based on a vegetation index, which is changed by the presence of snow or ice. The radiative transmittance is affected by the presence of water and ozone (the ozone is based on a monthly climatology) in the model. The version of the model used has 22 layers in the vertical. It is a spectral model, which means that the fields in each horizontal layer are represented as a series of suitably combined orthogonal base functions: spherical harmonics based on Legendre functions. The spectral model has a T21 resolution, where T denotes a triangular truncation and 21 denotes the largest wavenumber mode to appear in the representation. To deal with the non-linear terms, the model uses also a 64×32 grid transforming the spectral model via Fourier transform. Therefore, the atmosphere model in FORTE has 64×32 points, which correspond to about 5.625°×5.625°.

2.1.3 Flux Adjustments

Coupling

The two model components need some boundary conditions. The atmosphere needs to receive daily the ocean's SST and the ocean needs daily the heat flux, water flux and the windstress from the atmosphere. Although the component atmosphere and ocean GCMs may independently reproduce acceptable simulations when forced at the surface with a climatology (e.g. (Levitus, 1998)), significant errors can appear when the two components are coupled (Sausen et al., 1988; Manabe and Stouffer, 1988). Deficiencies in the model's physics are not always seen when the model is forced by non-interactive boundary conditions and has fewer degrees of freedom. When the components of FORTE are coupled, the ocean model drifts from the realistic present day climate with a trend of 0.14°C/century in the averaged ocean temperature. Only a very long integration of several thousand years would allow the model to reach an equilibrium state. Inaccuracy in representing the climate can be observed at various locations: the equator to pole temperature gradient is too weak compared to the climatology (Levitus, 1998) due to extra heat transferred from the atmosphere to the ocean in the southern ocean when coupled and due also to the simplified sea-ice parameterisation (the ice extent is too small around Antarctica). An excessively strong cold tongue in the Equatorial Pacific is observed as a result of excessive upwelling at this resolution (figure 2.3). The coupled model also shows a strong overturning cell in the North Pacific, which has a similar pattern to the North Atlantic overturning. Unrealistically, fresh water is observed at locations where the run-off scheme dumps excess rainwater into the sea (figure 2.3). The Baltic Sea and Hudson Bay have negative salinities whereas the Red Sea (closed seas in the model) has a salinity of 300 PSU. The salinity flux is calculated by multipling the precipitation minus evaropation plus run-off (P-E+R) water flux by a constant global reference salinity. In regions with an always positive freshwater input (such as the Baltic and Hudson Bay) and without a good way of mixing the input water away to the rest of the ocean, this will result in a negative salinity. In the Baltic Sea and Hudson Bay or any other region enclosed with areas of one or two gridboxes wide, the water cannot advect properly and the constant freshwater flux will result in a negative salinity. This scheme is not ideal but the unrealistic salinities usually stay confined to the local region and should not affect the large scale circulation.

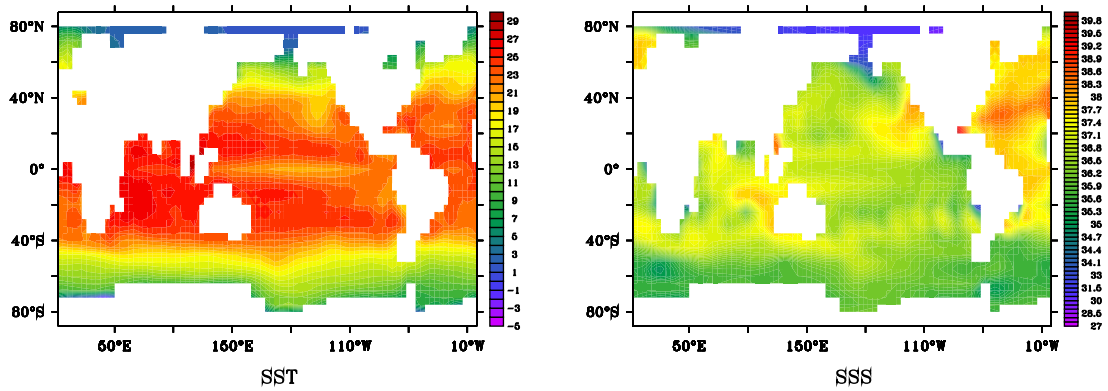

Figure 2.3: *Annually average SST (in °C) (left) and SSS (in PSU) (right) obtain without flux adjustments with the FORTE model.*

If the representation of the climate system is unrealistic, the sensitivity to the vertical diffusivity might be biased. To obtain a better control run, additional "flux adjustments" are used in FORTE.

Flux Adjustments

Therefore, additional fluxes of heat and fresh water are added or subtracted to the original physical atmospheric surface fluxes passed to the ocean to prevent this drift (Sausen et al., 1988). Flux adjustments are applied to force an unrealistic climate state towards a more realistic one. As the adjustments added are temporally constant over the integration, climate perturbations are still passed onto the climate system, which is able then to respond to them (Sausen et al., 1988; Marotzke and Stone, 1995). This ensures that any perturbation in the forcing is applied to a realistic reference surface climate, so that distortions to the major climate feedback processes are minimised (Marotzke and Stone, 1995). The coupling of the two models can highlight discrepancies in the surface fluxes which causes the climate to drift away from the desired state.

To calculate the flux adjustment fields, the two model components are first run in coupled mode, but the ocean is actually forced by climatological fields (a daily field

is calculated from the nearest two monthly fields, based on the day of the month). The sea surface temperatures (SST) obtained are passed to the atmosphere. The atmosphere adjusts to the SSTs and creates fluxes that would normally be passed to the ocean. Here instead, the fluxes are stored, and the ocean is forced at the next timestep by a climatological field again Levitus (1998). It is forced by monthly climatological fields (a daily restoring field is calculated from the nearest 2 monthly fields based on the day of the year) with monthly fields from Levitus (1998) and the European Centre for Midrange Weather Forecasting. The adjustment fluxes are then calculated by subtracting the stored atmospheric fluxes from the climatological fluxes. This is done using monthly averages of all fields. In the fully coupled model, the flux adjustments are added to the fields passed to MOMA before they are used to force the ocean. The flux adjustment fields have been calculated over 50 years to average over the interannual and interdecadal variability and thus stop the model from drifting (Furevik et al., 2003).

Different sets of flux adjustments have been tested and run over 50 years (only two are detailed below). The first one is calculated as explained above, with the yearly mean value of the fluxes with values above the following thresholds removed: heat flux above 300 W/m^2, and value of the water flux above 10 m/year (figure 2.4). Values above these thresholds are considered not to have any physical meaning and are usually located in closed seas. The heat flux adjustment obtained has the strongest corrections in the ACC region, east of the coast of Canada and Red Sea. The water flux adjustment obtained has the stongest corrections east of the coast of Canada, west north tropical Pacific, in Arctic region and Indian Ocean. The SST and sea surface salinities (SSS) obtained are more realistic than without the flux adjustment (figure 2.6). Nevertheless, the equatorial Pacific is too cold and the east Pacific warm pool is too small. The SSS has high values in the Atlantic and Pacific ocean and the equator to north differences are poorly represented.

The second set of flux adjustment fields are obtained from zonally integrating the first set of fields flux over each basin (figure 2.7). This enables errors in the meridional transport to be corrected, whilst reducing the amplitude of the flux adjustments (Weaver and Hughes, 1996). The resultant SST fields obtained using the flux adjustments are shown in figure 2.9, which is satisfactory and give a better representation of the real climate when compared with the climatology. The SST obtained has a stronger equator to pole gradient with a warm pool in the Indo-West-Pacific ocean. The SSS shows a fresh region at the equator, and are saltier in

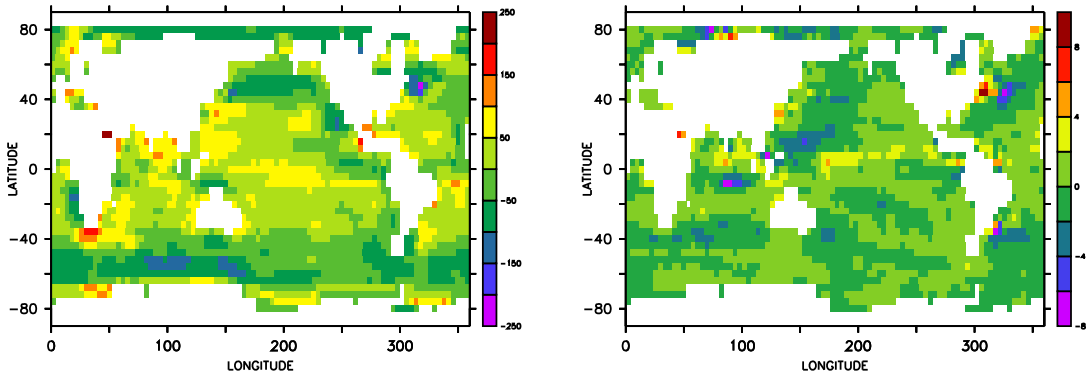

Figure 2.4: *Annual average flux adjustment fields, left: heat flux in W/m^2, and right: water flux in m/year with extreme values removed.*

subtropical regions. The strength of the overturning in the different basins is also more realistic (not shown). The global, total average heat flux is 1.27 $W/m^2/year$ and the water flux is 0.0835 m/year. This is expected to contribute to the drift of the system over long time integrations. The second setup with the zonally integrated flux is used throughout the following experiments. In this setup, the model drifts at 0.072°C/century for globally averaged temperature in the ocean (half of the drift obtained in a run without flux adjustments).

2.1.4 Periodic Coupling

Theory

In the setup of FORTE used herein, the atmosphere model is the most computationally expensive part of the system and needs more time during the integration per timestep than the ocean. The atmosphere needs 64 timesteps a day, as the physical processes are much faster in the atmosphere than in the ocean. If the ocean is run alone only four timestep a day are required. A straightforward, fully coupled integration would take several real-time years if run to equilibrium from a model started at rest. In our experiments, we use the National Oceanography Centre (NOC) supercomputer Proteus which has 12 processors 24Gb SGI Onyx300 and a desktop

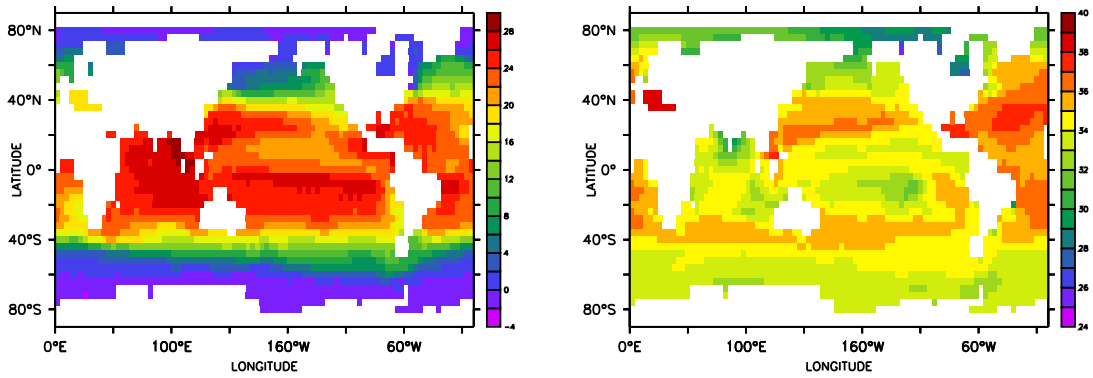

Figure 2.5: *Annual average SST (left) (in °C) and SSS (right) (in PSU) after 50 years integration using the above flux adjustment fields.*

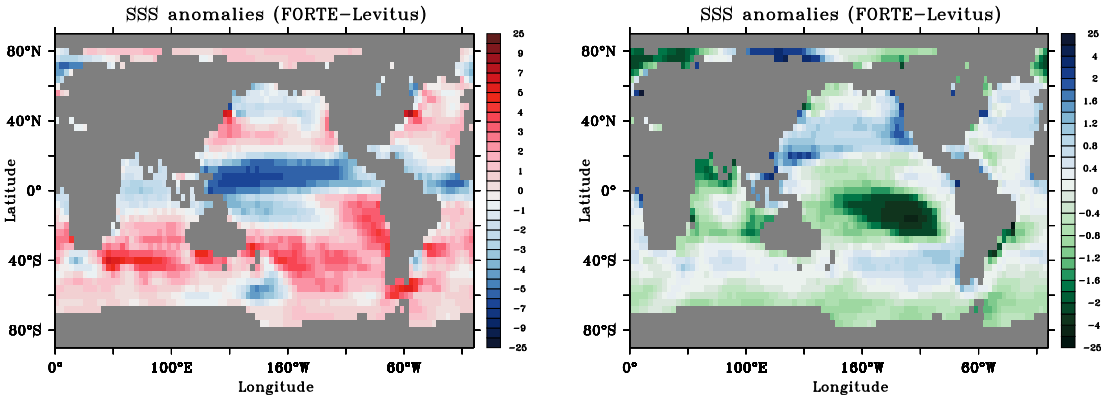

Figure 2.6: *SST difference between the SST obtained with the above flux adjustment and Levitus (left) (in °C) and SSS difference between the SSS obtained with the above flux adjustment and Levitus (right) (in PSU) after 50 years integration.*

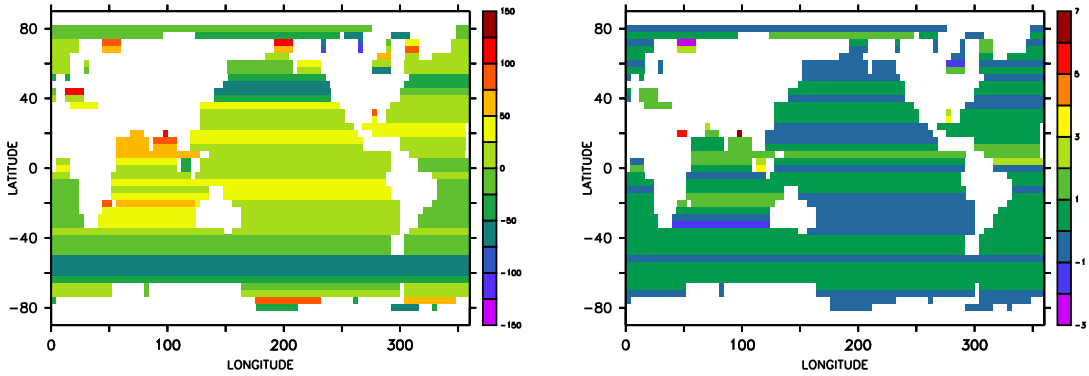

Figure 2.7: *Zonal average flux adjustment fields over each basin for the month of January; left: heat flux field (in W/m^2) and right: water flux (in m/year) adjustment fields zonally averaged over each ocean basin.*

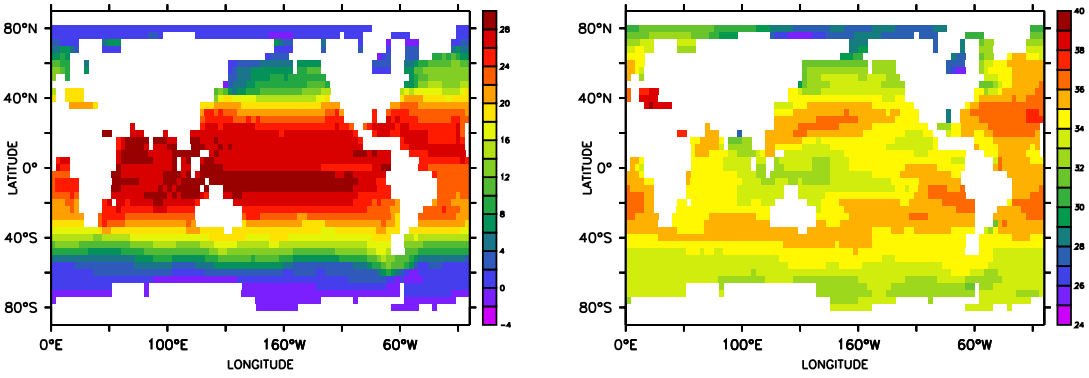

Figure 2.8: *Annual average SST (left) (in °C) and SSS (right) (in PSU) fields obtained from the above flux adjustments after 50 years of integration using the zonally averaged flux adjustment fields.*

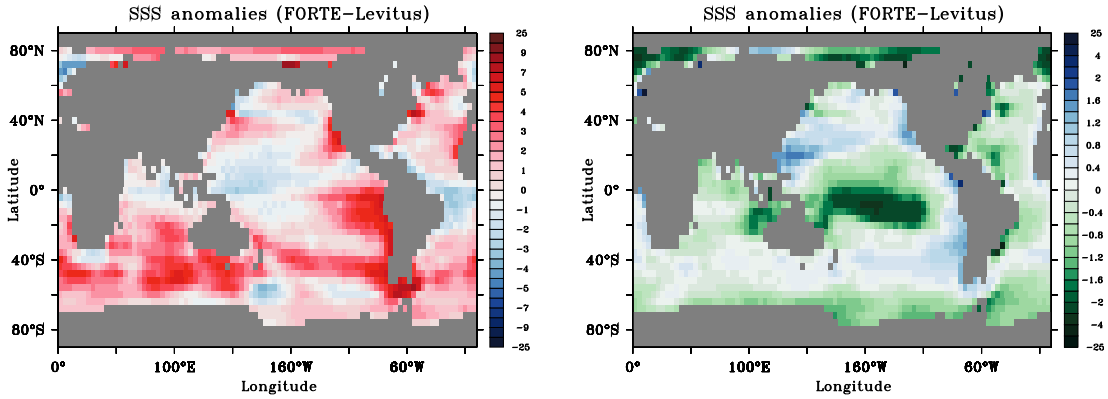

Figure 2.9: *SST difference between the SST obtained with the above flux adjustment and Levitus (left) (in °C) and SSS difference between the SSS obtained with the above flux adjustment and Levitus (right) (in PSU) after 50 years integration.*

PC: 2x Intel Xeon 2.4 GHz 1Gb RAM. To be able to reach an equilibrium state in a shorter time, the model uses the periodically synchronous coupling scheme of Sausen and Voss (1996). The basic scheme is represented in figure 2.10 and calculated for each oceanic grid point. The scheme is divided into three steps:

1. The model is run synchronously to calculate new boundary conditions. The atmosphere adjusts quickly, so it does not need a long time integration to adjust to the new ocean state and calculate valid fluxes. During the last year of synchronously coupled period, the daily values of the heat and freshwater fluxes and the monthly values of the windstress, which are passed over to force the ocean, are stored in the data bank as f_{syn}.

2. At the end of a synchronously coupled period, the new daily and monthly values of the ocean forcing f_{oce} is calculated. First, the new annual mean F_{oce} is calculated by:

$$F_{oce} = \frac{d \cdot F_{oce(prev)} + F_{syn}}{d+1} \tag{2.4}$$

   Where, d is a weighting coefficient of the annual means, and reduces the interannual variability of the atmosphere-ocean fluxes (here, d=2 as used by (Voss 1998)). F_{syn} is the annual mean fluxes of the previous synchronously

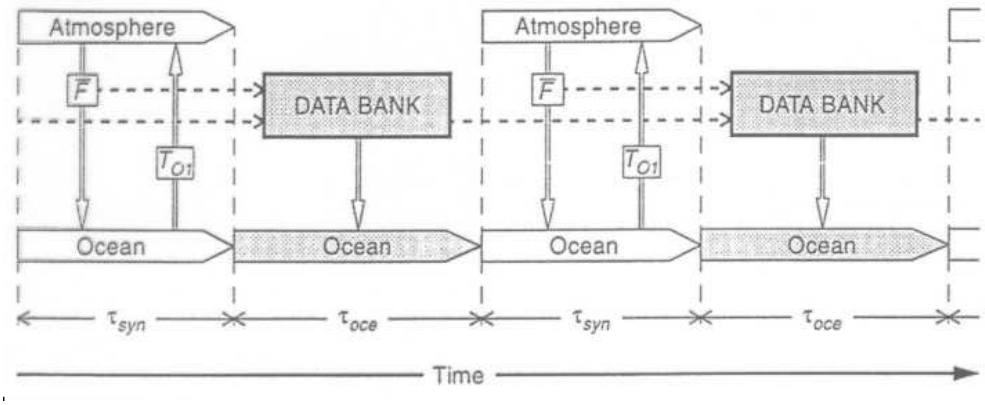

Figure 2.10: *Schematic of the basic periodic coupling scheme from Sausen and Voss (1996).*

coupled period. $F_{oce}(prev)$ is the annual mean fluxes of the last ocean-only period. Then the daily and monthly values of f_{oce} of the annual cycle for the ocean-only period is calculated by:

$$f_{oce} = f_{syn} - F_{syn} + F_{oce} \tag{2.5}$$

3. The forcing f_{oce} is used for each year of the ocean-only run. This is faster as the ocean does not have to wait for the atmosphere. This scheme works because the ocean adjusts on long timescales than the atmosphere, and the boundary conditions can be keep constant over a few years while the deep ocean adjusts.

After a few years, the atmosphere is switched on again to calculate new boundary conditions. The whole procedure is then repeated.

Periodic Ratios

Sausen and Voss (1996) found that it is important when choosing the ratio between the fully coupled integration and the uncoupled integration that the cycle is not a multiple of 6 months. So the following coupling ratio has been chosen: after an initial year in synchronous mode, a cycle of 19 months synchronous run and 60 months ocean-only run are carried out during the spin-up. The cycle of 19 months synchronous is chosen to allow the model 7 months to recover from any small

coupling shock in each cycle before the new boundary conditions are computed. The following scheme is implemented during all the spin-up integrations. The timestep in the ocean can be significantly increased when run on its own, from a timestep of 30 minutes for the tracer and velocity to 6 hrs.

The periodic scheme could induce spurious frequencies into the climate simulation. The spectrum of the THC and the SST during 100 years fully couped run and a run using the periodic coupling are compared. The asynchronous mode show a significant peak at 9 years period for the THC spectrum and at 6 years period for the SST spectrum, (figure 2.11). Neither of these peaks is found in the spectrum of the synchronous runs. To avoid any spurious cycle in the analysis, the data analysed are only from the synchronous integration from the end of the integration (see Chapter 3).

2.2 The MPI Model

2.2.1 Model

The second coupled atmosphere-ocean GCM used as part of this study is ECHAM5/ MPI-OM from the Max Planck Institute for Meteorology, Hamburg.

The atmosphere component ECHAM5 is the 5^{th} version in a series of ECHAM models originating from the spectral weather prediction model of the European Centre for Medium Range Weather Forecasts (ECMWF) (Simmons et al., 1989). ECHAM5 is a spectral model, used here with a T31 horizontal resolution and 19 vertical layers (Roeckner et al., 1996; 2003). The CO_2 concentration is constant, equal to the preindustrial value of 278 ppm. The ocean component, MPI-OM (Max Planck Institute - Ocean Model), is a horizontal Arakawa C-grid model (figure 2.12) (Arakawa and Lamb, 1977), with a vertical discretisation in z-coordinates with 40 levels (Marsland et al., 2003). The grid is curvilinear with the North Pole moved over Greenland, creating a higher resolution grid in the main sinking regions associated with the THC. The grid is approximately equal to $3.75° \times 3.75°$ at the equator (figure 2.13). The sea-ice is a dynamic-thermodynamic Hibler-type model (Hibler III, 1979). The model components are coupled together with the Ocean Atmosphere Sea Ice Soil (OASIS) coupler (Terray et al., 1998) and runs without flux adjustments. The coupled model has already been used in other studies (eg. Pohlmann et al. (2006); Jungclaus et al. (2005); Jacob et al. (2005)).

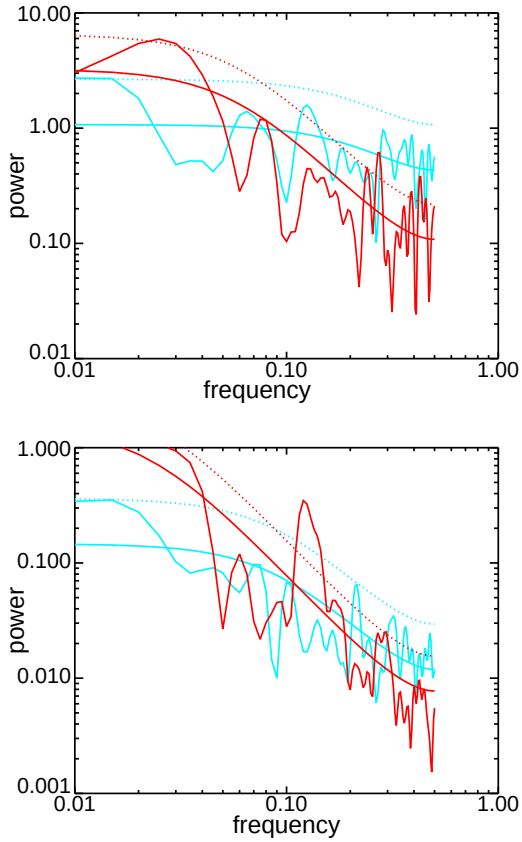

Figure 2.11: *Frequency spectrum of the THC (in Sv^2/year) and SST (in $\circ C^2$ C/year) during a fully coupled (blue lines) and a run using the periodic coupling (red lines) with the FORTE model over a 100 years integration. The line represent the AR(1) and the dotted lines represent the 90% confidence interval (CI).*

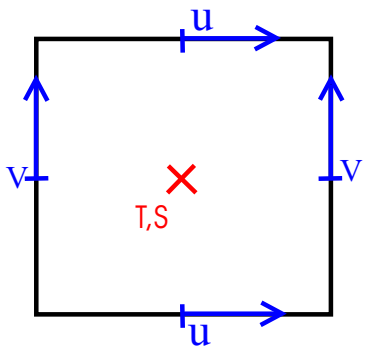

Figure 2.12: *Schematic of the Arakawa C grid used in the MPI-OM model. The velocity vectors u, v are situated at the middle of each side of the grid box, and the tracer T, S are situated at the corner of each grid box. u and v are roughly along longitude and latitude, since the model grid is curvilinear.*

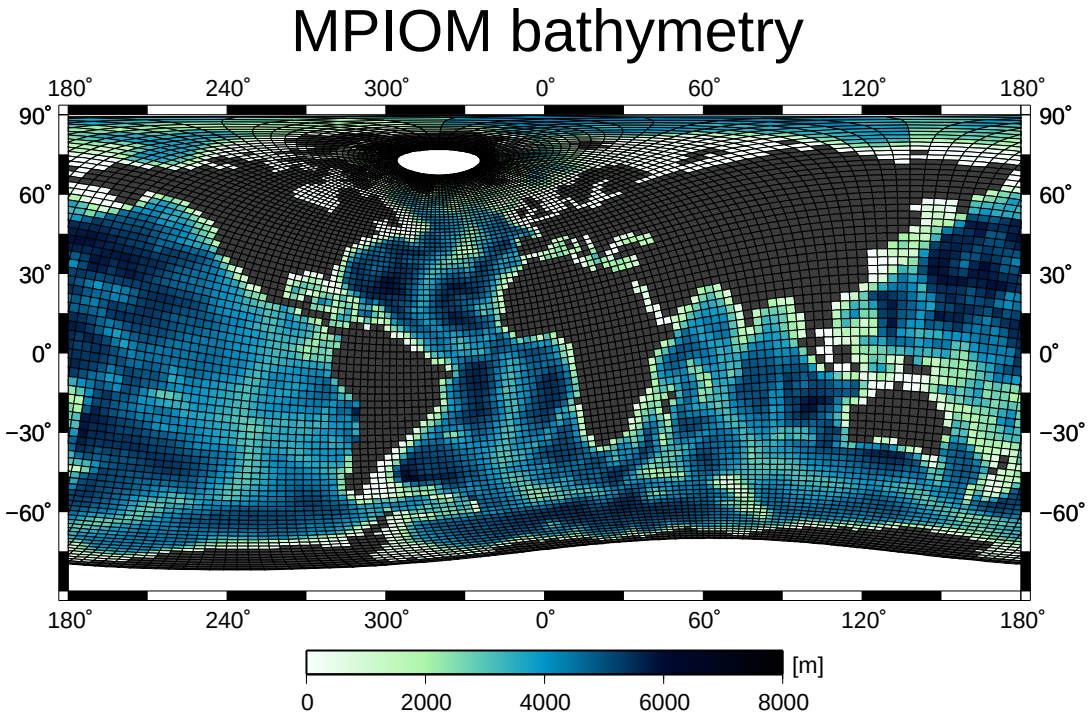

Figure 2.13: *MPI-OM grid and bathymetry.*

Mixing in MPI-OM

The MPI-OM model uses the subgridscale form of mesoscales eddy mixing from Gent et al. (1995). The tracer diffusion follows the Redi (1982) and Gent and McWilliams (1990) transformation and the Griffies et al. (2001) implementation. All the experiments use isopycnal/diapycnal diffusion. The MPI-OM model uses different subgridscale parameterisation to FORTE to obtain a more realistic representation of the mixing processes in the ocean involving bottom boundary layer (BBL) slope transport, isopycnal and diapycnal viscosity, diapycnal and isopycnal diffusivity, eddy-induced mixing, wind-shear, Richardson number and convection. These contributions are now introduced one by one.

The Bottom Boundary Layer

In most cases, dense water masses are formed in marginal seas before the overflow crosses a sill into the ocean basin, or on shelves before sliding down the continental slopes. In z-coordinates models, this process involves horizontally advecting the dense water at the sill into lighter water, inducing an intense unphysical mixing. The Bottom Boundary Layer (BBL) parameterisation of Price and Baringer (1994) is used here. The BBL parameterisation redirects the dense water masses to the neutral buoyancy level in the adjacent water column as if it had flowed along the slopes (figure 2.14) (Campin and Goosse, 1999).

Convective Adjustment

In the presence of static instability the upper grid cell is mixed with an equivalent thickness of the lower adjacent grid cell by increased diapycnal diffusivity. This is done once per timestep through out the water column. The mixing induced by convection, $\kappa_\nu^n(convection)$, is 500 cm^2/s.

PP-Scheme

The diapycnal mixing also uses the PP-scheme, which is defined by the Pacanowski and Philander (1981) parameterisation to which a wind induced stirring is added. $\kappa_\nu(PP - scheme)$ follows the equation below:

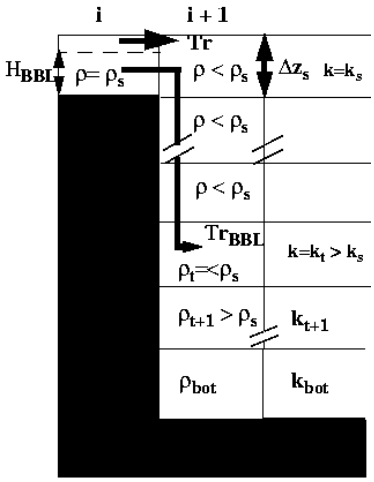

Figure 2.14: *Diagram of BBL advective transport to the level of neutral density ρ_t at depth k in the MPI-OM model. The arrows represent the transport (Tr) at the sill and to the level of neutral density (Tr_{BBL}). i represents the grid cell (Wetzel et al., 2005).*

$$\kappa_\nu(PP - scheme) = \kappa(Richardson) + \kappa(wind) + \kappa(background) \tag{2.6}$$

The wind mixing (κ_w) is calculated using the local wind stress above the ocean surface. The near surface wind mixing is proportional to the cube of the local wind speed at 10 m V_{10m}, and is reduced in proportion to the fractional sea ice cover I. It decays exponentially with depth and depends on the local stability $\delta_z\rho$. κ_w is defined by:

$$\kappa_w\,(1) = (1 - I)\,W_T V_{10m}^3 \tag{2.7}$$

$$\kappa_w\,(k) = \kappa_w\,(k-1)\,\frac{\frac{\lambda}{\Delta z}}{\frac{\lambda}{\Delta z} + \delta_z\rho} e^{\frac{\Delta z}{z_0}} \tag{2.8}$$

Where, k is the vertical level and Δz is the level thickness. λ, z_0 and W_T are adjustable parameters which are tuned for optimal mixed layer depths (here λ=0.05, z_0=40 and W_T=2.3x10^{-6}, V_{10m} is the local ten metre wind speed .

The Richardson number dependent mixing ($\kappa(Richardson)$) is calculated using the Richardson number. The Richardson number R_i is a dimensionless number and

is calculated locally by the ratio of the static stability or Brunt-Väisällä frequency (N) to the the square of the wind shear (S) by the following equation:

$$R_i = \frac{-\frac{g}{\rho}\frac{d\rho}{dz}}{\left(\frac{\partial u}{\partial z}\right)^2 + \left(\frac{\partial v}{\partial z}\right)^2} = \frac{N^2}{S^2} \tag{2.9}$$

Where, ρ is the potential density, g is acceleration due to gravity and u and v are the east and north current amplitude. The higher N is, the more stable the flow is.

R_i may vary rapidly across a sheared boundary, such as the ACC current or the Gulf Stream. Even under statically stable conditions, instability is possible when the current shear is strong enough to break up the stable layer and produce breaking waves which enhance turbulence. This occurs when R_i<0.25. Because the ocean tends to be strongly stratified and currents tend to be weak, turbulent mixing is intermittent and rare.

The full equation of the PP-scheme parameterisation can be written as:

$$\kappa_\nu^n(PP - scheme) = (1 - \Lambda_\kappa)\,\kappa_\nu^{n-1} + \Lambda_\kappa \left(\kappa_{\nu 0}\,(1 + C_{R\kappa} R_i)^{-3} + \kappa_w + \kappa_b\right) \tag{2.10}$$

Where, n indexes the timestep and Λ_κ is a relaxation coefficient. R_i is the local Richardson number. $\kappa_{\nu 0}$ and $C_{R\kappa}$ (=5) are adjustable constant parameters. κ_w is the wind induced mixing term, κ_b is the background diffusivity.

Total Mixing

Figure 2.15 shows the effective diffusivity $\kappa_\nu(total)$ in the control run over the last 10 years of integration (the control run will be defined in the following section). We can notice the total diffusivity shows strong spatial differences. The ocean interior is equal to the background diffusivity. The global ocean shows enhanced mixing in the ACC region, in the surface layer over which the winds blow, near bottom topography and near the Antarctic slope. The Atlantic basin shows enhanced mixing in the region of deep convection where mixing occurs throughout the water column. The higher values in the ocean interior are located in the mid-Atlantic ridge.

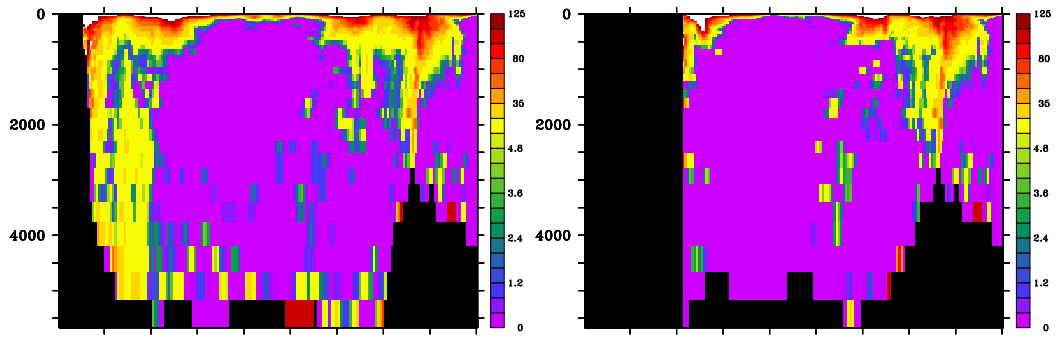

Figure 2.15: *Zonal average total diffusivity in the control run in the MPI-OM model over the last 10 years of the integration with κ_b=0.1 cm^2/s, (in cm^2/s); left: global ocean, right: Atlantic basin. The y-axis represents the depth in metres.*

The total mixing $\kappa_\nu(total)$ in the ocean is found to have strong spatial variations mainly in the surface layers and above rough topography. In the ocean interior, the mixing from MPI-OM is equal to κ_b. At each time step the stability of the water column is calculated and if the water is unstable, $\kappa_\nu^n(total) = \kappa_\nu^n(convection)$, otherwise $\kappa_\nu^n(total) = \kappa_\nu^n(PP - scheme)$. The total mixing has the following form:

$$\kappa_\nu^n(total) = \kappa_\nu^n(convection) + \kappa_\nu^n(PP - scheme) \tag{2.11}$$

The MPI-OM has a background diffusivity, κ_b 10 times smaller than in FORTE but the extra mixing terms present in MPI-OM model give a different basin average diffusivity. In the ocean interior, the FORTE model will diffuse much more than the MPI-OM. At the surface layer and next to near rough topography, the MPI-OM can reproduce the strong mixing values at the surface and rough topography. The extra diffusivity is not spatially constant over the ocean basin but gives on average a very similar mixing to FORTE especially for the ocean-only experiments (table 2.2).

Average diffusivity in cm^2/s	MPI-OM coupled experiments	MPI-OM ocean-only experiments	FORTE
$\kappa_b(background)$	0.1	0.1	1
$\kappa_\nu^n(PP-scheme)$	0.763	0.9301	0
$\kappa_\nu^n(total)$	3.23	4.103	n/a

Table 2.2: *Diffusivity in MPI-OM and FORTE models, obtained in their respective control run.*

Chapter 3

Spin-up and Control Run

This chapter introduces the different spin-up experiments used in this study. The fundamental properties of the model control climate and some of the modes of variability in the control runs are shown and compared to observational data.

3.1 FORTE

3.1.1 Spin-up

The spin-up of the control run is done by integrating the atmosphere and ocean models independently with climatological forcing before coupling them together. The ocean has been integrated for 4200 years with restoring to surface salinity and temperature fields interpolated from an annual cycle from Levitus (1998) and a wind

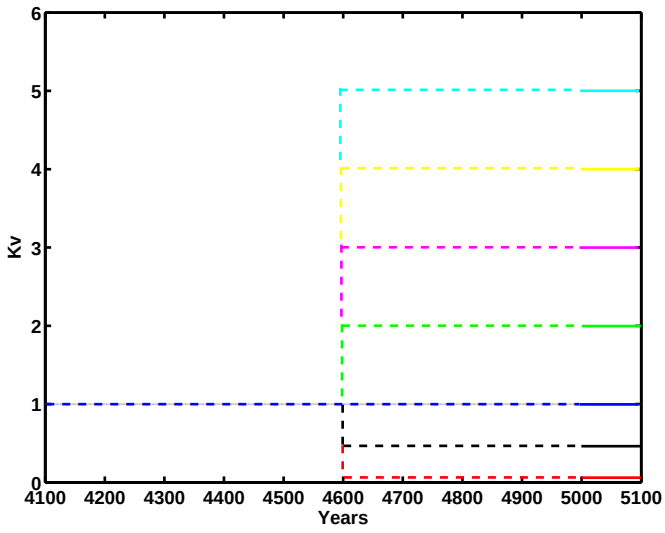

Figure 3.1: *Sensitivity experiments for the different vertical diffusivities. The dotted lines represent the periodic (asynchronous + synchronous) mode and continuous lines the synchronous mode. Red: κ_ν=0.1 cm^2/s, black: κ_ν=0.5 cm^2/s, blue: κ_ν=1 cm^2/s, green: κ_ν=2 cm^2/s, purple: κ_ν=3 cm^2/s, yellow: κ_ν=4 cm^2/s, and turquoise: κ_ν=5 cm^2/s.*

forcing field from Hellerman and Rosenstein (1983). The atmosphere has been spun-up for 20 years using SST fields from Levitus (1998). The two components are then coupled together for 400 years using the periodic coupling, with a standard diapycnal diffusivity of 1 cm^2/s and with the flux adjustments using the zonal average fluxes, to obtain the spin-up for the control run. The sensitivity experiments are started from this coupled reference: κ_ν is changed instantaneously to a value of 0.1, 0.5, 2, 3, 4 or 5 cm^2/s and the integration is continued for another 400 years, still using the periodic coupling (figure 3.1). Then a 100 year fully coupled period is appended. The runs are shown to be close to a cyclostationary state after 500 years integration even the ones with low diffusivity (figure 3.2). The surface fields do not show any drift and the strength of the meridional overturning is nearly stabilised after the 400 years. A complete equilibrium is very difficult to obtain due to the long adjustment time-scale of deep water to the new diffusion coefficient. All final states have a global mean heat budget imbalance and a small temperature drift in the average global ocean temperature (table 3.1).

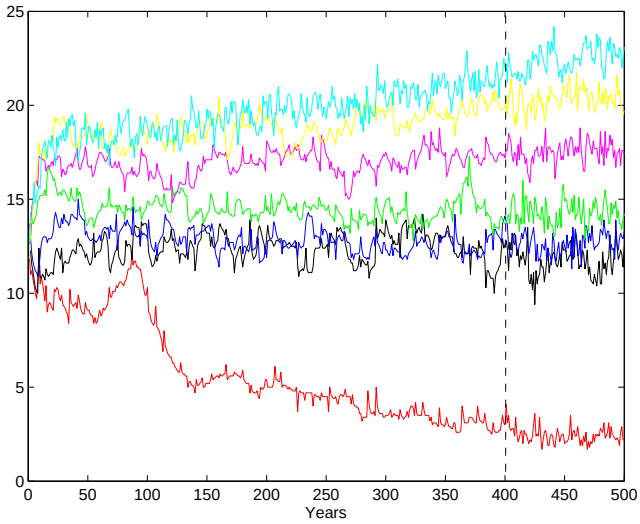

Figure 3.2: *Time series of the maximum strength of the MOC during the 500 years run (spin-up + 100 years fully control) (in Sv) with the FORTE model; red: κ_ν=0.1 cm^2/s, black: κ_ν=0.5 cm^2/s, blue: κ_ν =1 cm^2/s, green: κ_ν=2 cm^2/s, purple: κ_ν=3 cm^2/s, yellow: κ_ν=4 cm^2/s, and turquoise: κ_ν=5 cm^2/s.*

κ_ν (cm^2/s)	top of the atmosphere heat budget imbalance (W/m^2)	average ocean temperature (°C)	temperature drift (°C/century)
0.1	-0.03	3.764	-0.004
0.5	0.61	4.304	0.113
1	0.39	4.831	0.072
2	0.96	6.068	0.179
3	2.09	7.61	0.392
4	2.92	8.942	0.548
5	3.63	10.08	0.678

Table 3.1: *Globally averaged heat budget and temperature drift in the ocean for the different experiments with the FORTE model.*

3.1.2 Mean State of the Control Run

In this section, the mean state of the control run (named KV1 from hereon) over the last 100 years of coupled integration is described. The use of flux adjustments gives a more realistic meridional temperature gradient and salinity distribution than without. The SST in KV1 reproduces a surface climate close to the observations but the model is nevertheless unable to reproduce some of the small scale features (figure 3.3). There are a number of differences between the control run and the observations: at the surface: the Southern Ocean and high latitudes are too warm by 2-5°C (up to 8°C at some points) and the western tropical Pacific and Atlantic oceans are too cold by 1-2°C. The sea surface salinity (SSS) field is too fresh at some very localised and isolated grid cells in run-off regions and is too salty at the eastern boundary of the Pacific (figure 3.3). The deep ocean is too warm by around 2°C, due to a too a high value of the mixing in the ocean interior (κ_ν=1 cm^2/s), which is greater than observed in in-situ data. The northern high latitudes are characterised by convection in the Irminger Sea and Norwegian Sea but not in the Labrador Sea (figure 3.4).

The water mass transport is characterised by the MOC. The MOC in the Atlantic basin transports up to 13 Sv northward in the upper ocean and moves North Atlantic Deep Water (NADW) southward below 600 metres with sinking between 40°N and 60°N (figure 3.5). Only about 5 Sv is exported south of 30°S to the Southern Ocean, lower than observed (Talley, 2003). The shallow, wind-driven tropical cells transport around 13 Sv in the Atlantic and 30 Sv in the Indo-Pacific, with surface transport northward in the northern hemisphere and southward in the southern hemisphere. A weak overturning cell of Antarctic Bottom Water (AABW) can be seen in the deep Atlantic ocean with a maximum strength of just over 1 Sv. In the Indo-Pacific basin an overturning of strength 12 Sv reaches intermediate depths and upwells at low latitudes. The Deacon cell in the Southern Ocean transports 28 Sv southward at the surface.

3.1.3 Variability of the Control Run

The annual average maximum MOC in the North Atlantic has a mean value of 13 Sv with a temporal standard deviation of 0.6 Sv. Spatial patterns of SSTs

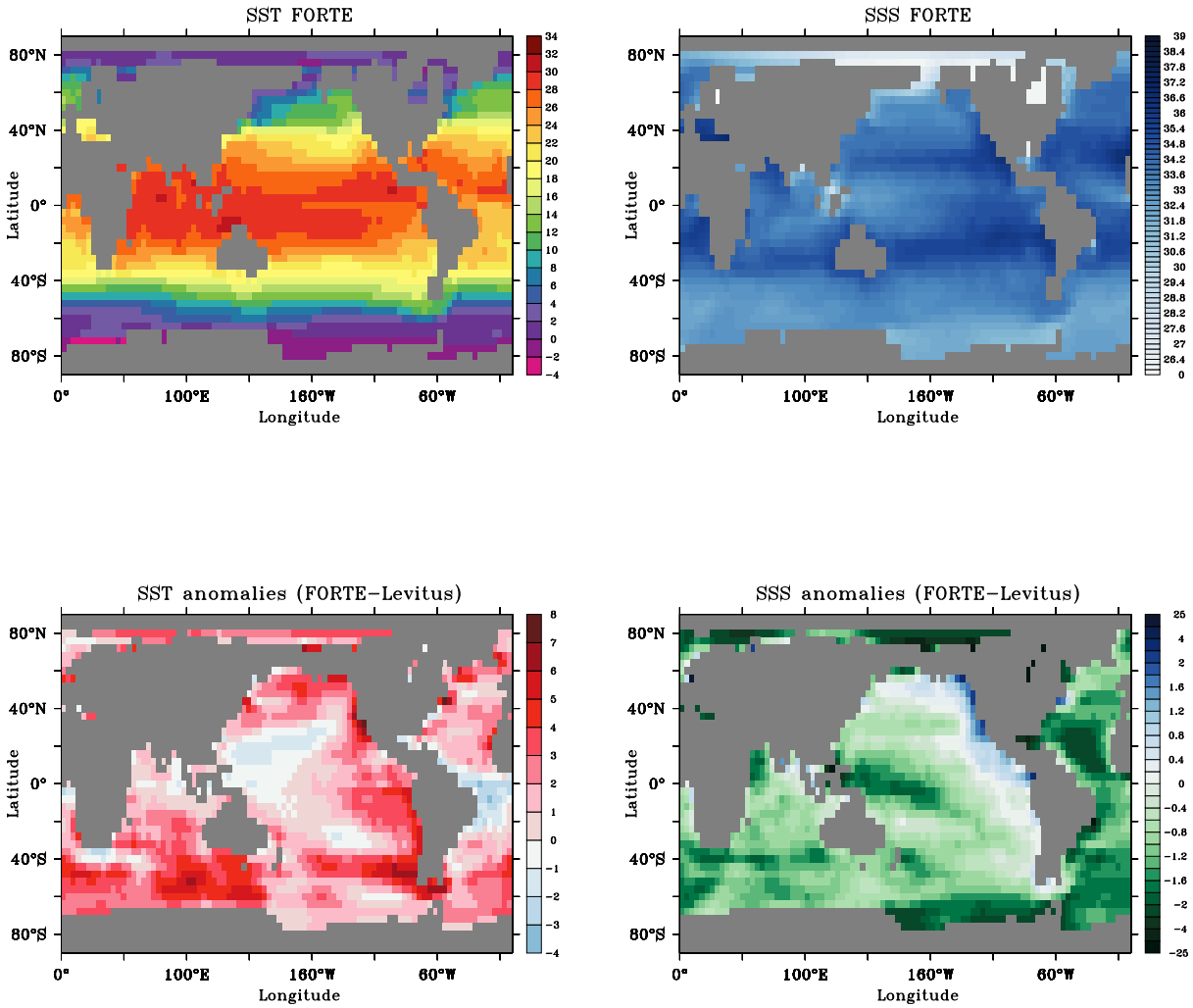

Figure 3.3: *Average SST (top left) (°C) and average SSS (top right) (PSU) of the last 100 years of the control run integration with the FORTE model. Difference between the above SST field and Levitus (Conkright et al., 1998) in °C (bottom, left) and difference between the above SSS field and Levitus in PSU (bottom, right).*

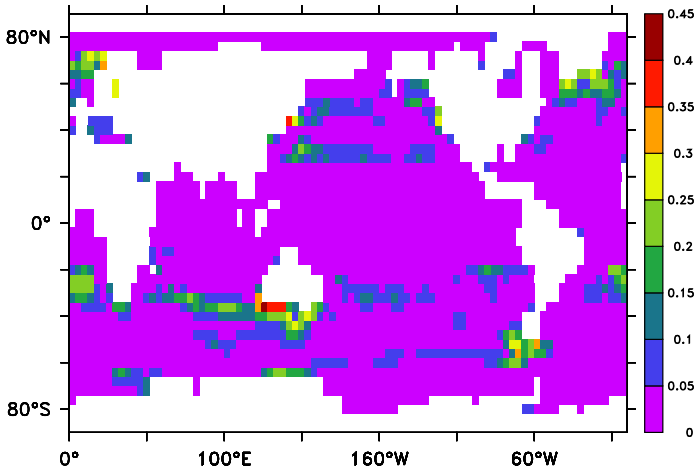

Figure 3.4: *Convection frequency per timestep in the control run (KV1) average over 100 years with the FORTE model.*

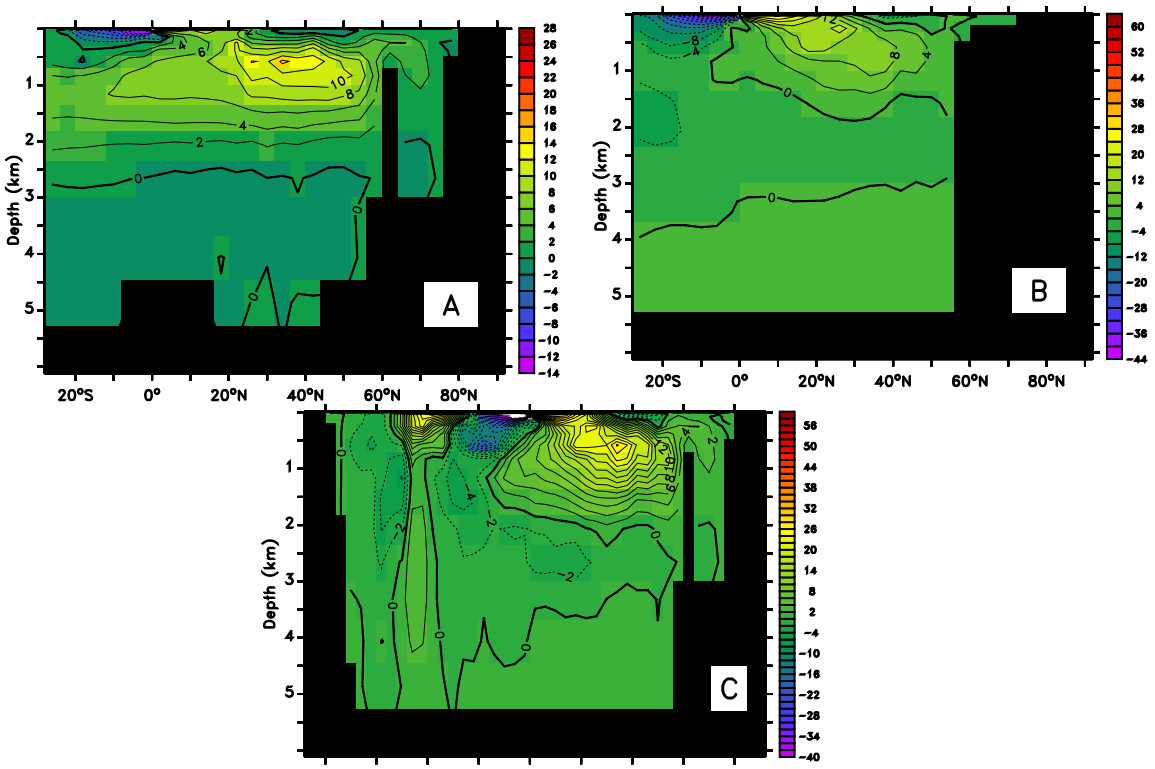

Figure 3.5: *Meridional overturning strength in Sv with the FORTE model for the Atlantic ocean (A) (contour interval: 2 Sv), for the Indo-Pacific ocean (B) (contour interval: 2 Sv) and for the global ocean (C) (contour interval: 4 Sv), for* $\kappa_v = 1 cm^2/s$*; positive values denote clockwise circulation, negative values denote counter-clockwise circulation.*

resembling the NAO (North Atlantic Oscillation) (Hurrell et al., 2003a) and ENSO (El-Niño Southern Oscillation) (Philander, 1990) are found. ENSO is defined in the equatorial Pacific by surface temperature anomalies compared to the long term mean temperature in this region. We have anomalies of 1.5°C between the warm and cold phases; the spectrum of these temperature anomalies shows a peak at 11 years within the 95% confidence interval and 6 years within the 90% confidence interval (figure 3.6). These anomalies are associated with an ENSO-like pattern, with warm anomalies in the eastern part of the basin for El Niño and cold anomalies for La Niña, but the periods in the model are longer than those observed. This can be explain by slow equatorial waves propagation in FORTE (N. Wells personnal discussion).

3.2 The MPI Model

3.2.1 Spin-up

The influence of the diapycnal mixing in the ocean on the coupled system is investigated by instanteneously changing the value of the background vertical diffusivity coefficient κ_b to 0.1, 0.25 and 1 cm^2/s from a spin-up control run with a value of κ_b=0.1 cm^2/s. Each experiment is run for 260 years, at which time the ocean is close to a cyclo-stationary state (figure 5.2). Only the last 10 years are used in the equilibrium state analysis, when the model is drifting the least (Table 3.2).

In addition to these runs, the same sensitivity experiments are done with only the ocean component of the coupled model. The ocean is provided every day with heat, water and momentum fluxes interpolated onto the model grid. The forcing is from the Ocean Model Intercomparison Project (OMIP) (Röske, 2001) and has developped in collaboration between MPI-Meteorologie, the German Climate Computing Centre (DKRZ) and the Alfred Wegener Institute for Polar and Marine Research. It provids a 365 day climatological forcing derived from the ECMWF 15 year reanalysis dataset (Gibson et al., 1997). The forcing was constructed by Gaussian filtering of the ERA data to produce a low-frequency and high-frequency component. The low-frequency components from all years were averaged to create a single mean year. Then the high-frequency component of a single year was superimposed onto the mean year to maintain quasi-realistic synoptic scale space-time variability.

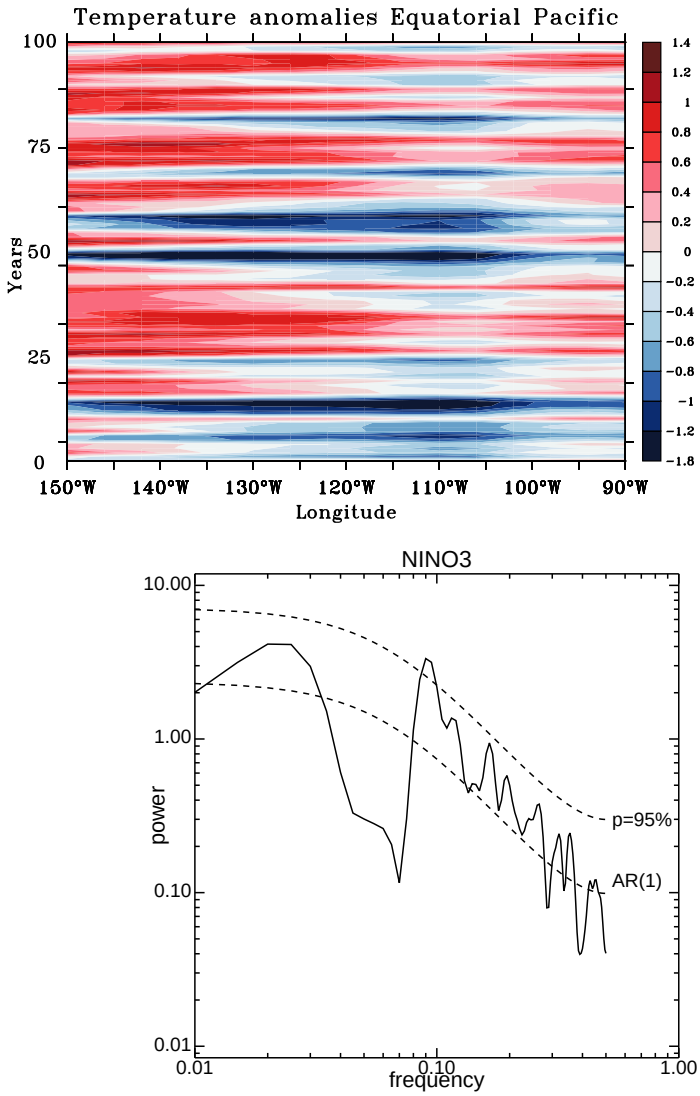

Figure 3.6: *Top: Yearly mean sea surface temperature anomalies in °C between 6° N and 6° S and from 152° W and 90° W in the eastern equatorial Pacific as a function of time in the FORTE model. Bottom: Spectrum of the sea surface temperature anomalies with confidence interval of 95% in the FORTE model .*

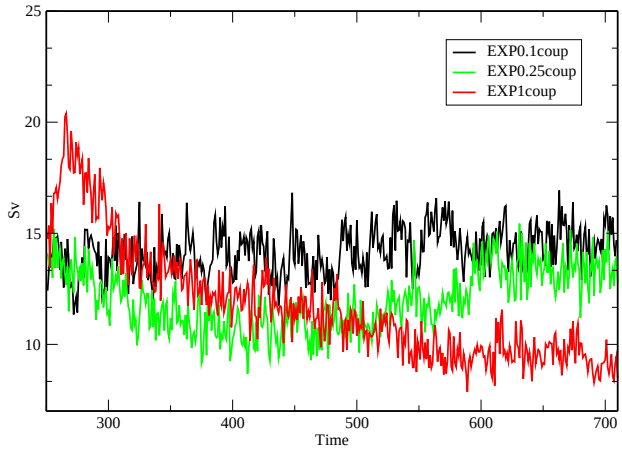

Figure 3.7: *Timeseries of the maximum strength of the MOC at 30-35 ^0N in the coupled experiments using the ECHAM5/MPI-OM model. Black: κ_b=0.1 cm^2/s, green: κ_b=0.25 cm^2/s and red: κ_b=1 cm^2/s.*

κ_ν (cm^2/s)	top of the atmosphere heat budget imbalance (W/m^2)	average ocean temperature (°C)	temperature drift (°C/century)
0.1	-9.13	17.5	0.004
0.25	-9.6	17.8	0.05
1	-12.5	19.2	0.4

Table 3.2: *Globally averaged heat budget and surface temperature drift in the ocean for the different experiments with the ECHAM5/MPI-OM model.*

The criterion for choosing a particular year for the high-frequency component was to maximise the variance of the OMIP-forcing relative to the variance of the original ERA data. For dynamical consistency it was considered desirable to choose only one hgh-frequency year for all forcing products (winds, temperatures, etc). As different products have maximum variance in different years, the maximization of variance was arbitrarily limited to zonal wind stress. This resulted in the choice of the year 1982, with preservation of 78

3.2.2 Mean State

In this section, we describe the mean state of the control run over the last 10 years of the coupled integration with ECHAM5/MPI-OM. The surface temperature and salinity fields are similar to the observed spatial patterns, see figure 3.8. The coarse resolution is unable to accurately represent the separation of the Gulf Stream and Kuroshio and strong temperature differences from the Levitus data are observed (Levitus, 1998) (eg. in the coastal upwelling regions, shown in figure 3.9). The surface salinity field is too salty in the Arctic regions, and differences are also found in the run-off regions. The temperature stratification is close to observations with a thermocline depth at 1000 m, but it is still too warm by 1-2°C in the deep ocean.

In the Atlantic basin, the maximum MOC transports 14.2 Sv and sinking occurs in the Irminger and Norwegian Seas and moves the North Atlantic Deep Water (NADW) southward below 1000 metres (figure 3.11). Strong shallow subtropical cells are observed in each ocean basin, with strengths of 20 Sv in the Atlantic basin and 40-60 Sv in the Pacific Ocean, with northward surface transport in the Northern Hemisphere and southward transport in the Southern Hemisphere. A weak overturning cell of Antarctic Bottom Water (AABW) can be seen in the deep Atlantic ocean, with a maximum strength of 2 Sv. The Deacon cell in the Southern Ocean transports 30 Sv southward at the surface. No deep convection is observed in the Pacific.

3.2.3 Variability of the Control Run

The annual average maximum MOC in the north Atlantic has a mean value of 14.2 Sv with a temporal standard deviation of 1.04 Sv. Park and Latif (2005) in a previous study, using a similar configuration of the ECHAM5/MPI-OM, looked at the NAO pattern using a 400 years integration. They calculated the leading EOF (empirical orthogonal function) mode of low-pass filtered SLP (sea level pressure) anomalies over the North Atlantic (figure 3.12). The first EOF, accounting for about 43% of the variance, is the NAO. The second most energetic EOF mode explains about 17% of the variance and resembles the East Atlantic Pattern (EAP). The EAP is structurally similar to the NAO, and consists of a north-South dipole of anomaly centers spanning the North Atlantic from east to west. The anomaly pattern is displace southeastward compared to the NAO pattern. Positive patterns are assiciated

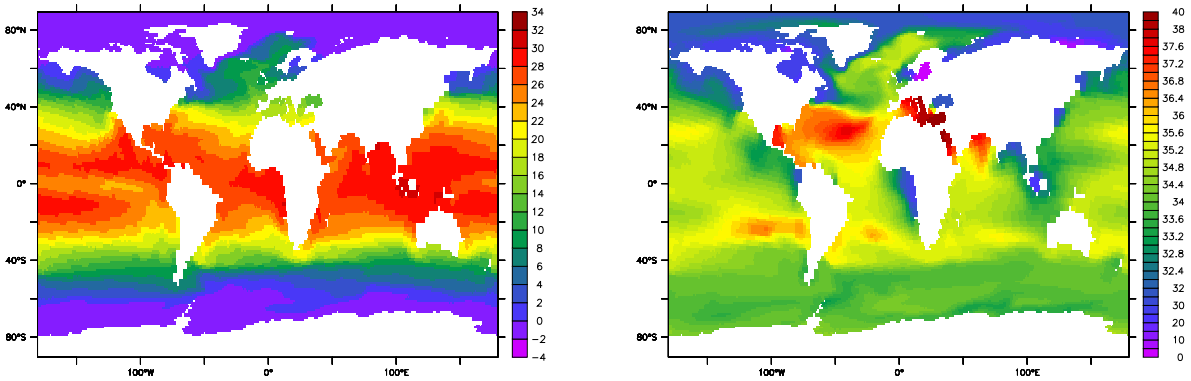

Figure 3.8: *Annual average SST (left) (°C) and average SSS (right) (PSU) of the last 10 years of the control run integration using the ECHAM5/MPI-OM model.*

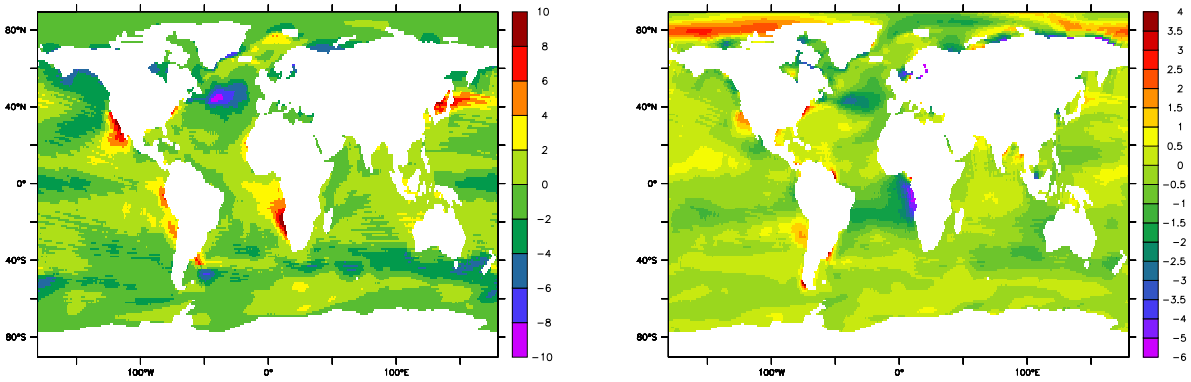

Figure 3.9: *SST (left) (°C) and SSS (right) (PSU) difference between the last 10 years of the control run from the ECHAM5/MPI-OM model and Levitus data.*

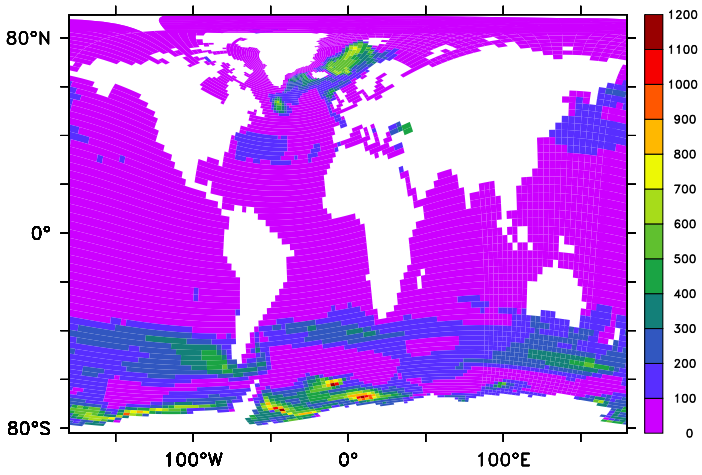

Figure 3.10: *Convection in the control run (EXP0.1) in metres in the ECHAM5/MPI-OM model.*

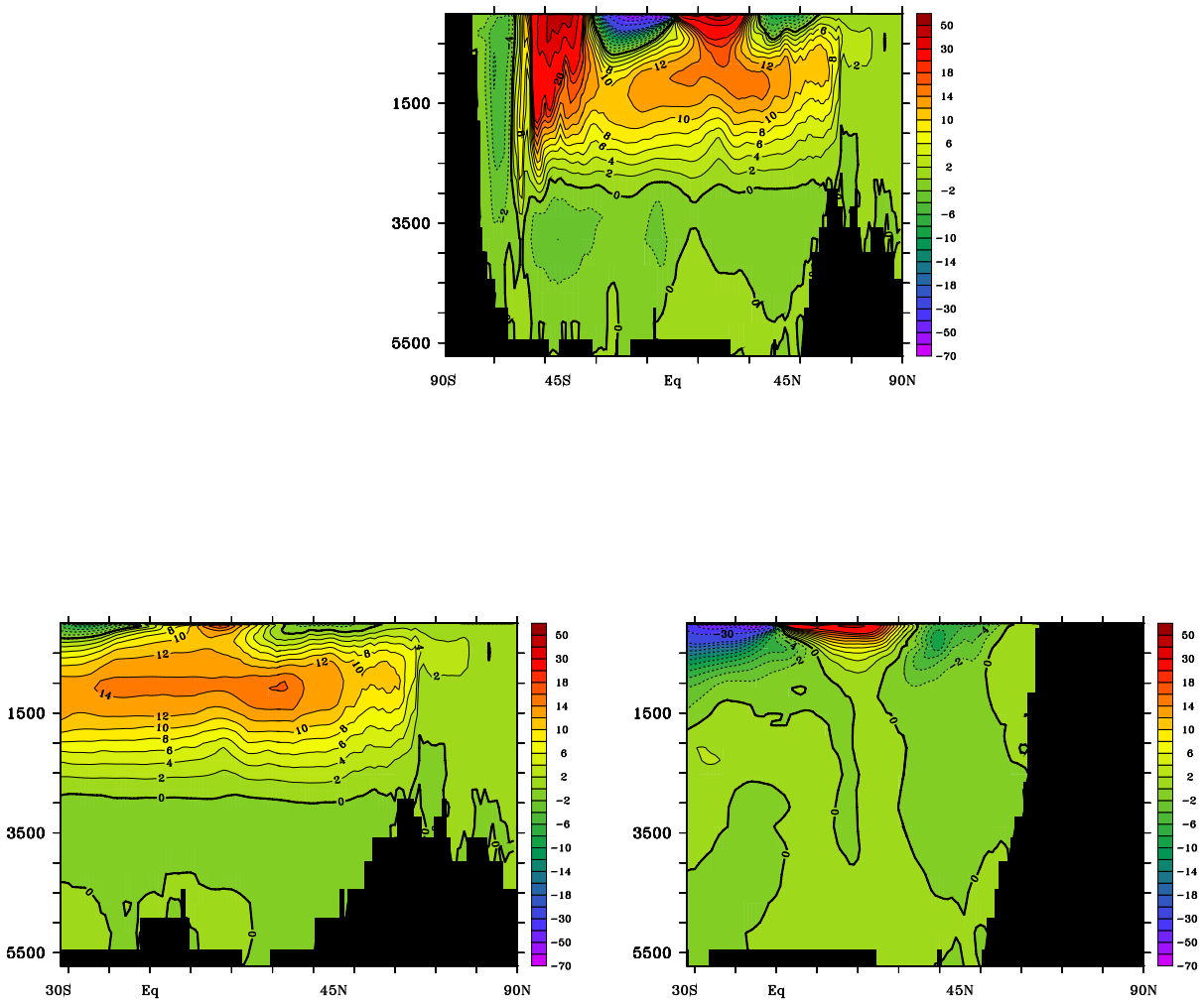

Figure 3.11: *In the coupled experiments using ECHAM5/MPI-OM, overturning strength in the global (top), Atlantic (bottom left) and Pacific (bottom right) ocean, contour interval 2 Sv. y-axis: depth in metres.*

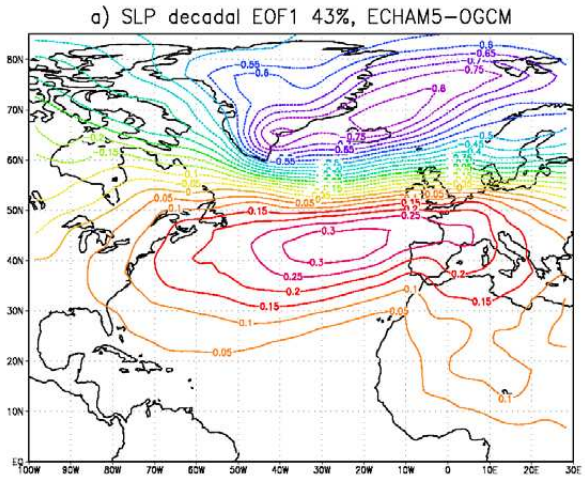

Figure 3.12: *NAO pattern in the ECHAM5/MPI-OM model from sea level pressure (SLP).*

with above-average surface temperature in Europe in all months and below average temperature over the southern US citetBarnston1987, citetWallace1981. They found that the principal component of the latter is correlated to the THC in the North Atlantic. Using the last 100 years of the control run, the ENSO signal in the equatorial Pacific is plotted using SST anomalies between 5°N and 5°S. There is a 2.5°C fluctuation between the warm and cold phases; the spectrum of these temperature anomalies shows a broad peak between 3-5 years within the 95% confidence interval (figure 3.13).

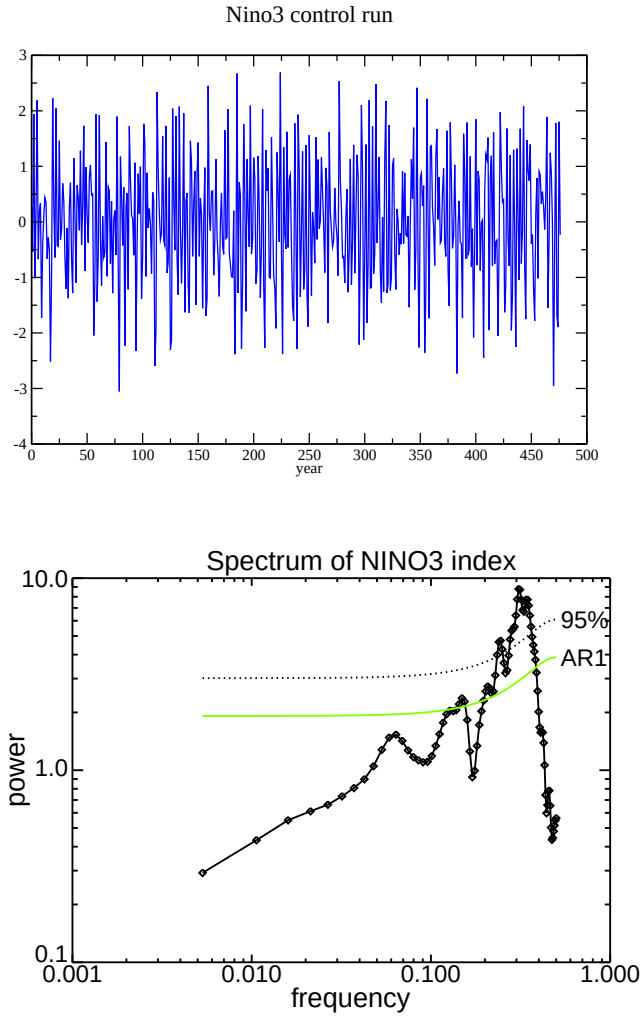

Figure 3.13: *Top: Yearly mean sea surface temperature anomalies in °C between 6° N and 6° S and from 152° W and 90° W in the eastern equatorial Pacific as a function of time in the ECHAM5/MPI-OM model. Bottom: Spectrum of the sea surface temperature anomalies with confidence interval of 95% using a Bartlett window.*

Chapter 4

FORTE Experiments

Seven experiments are undertaken with $\kappa_b = 0.1\ cm^2/s$, $\kappa_b = 0.5\ cm^2/s$, $\kappa_b = 1\ cm^2/s$ (control run), $\kappa_b = 2\ cm^2/s$, $\kappa_b = 3\ cm^2/s$, $\kappa_b = 4\ cm^2/s$ and $\kappa_b = 5\ cm^2/s$ and are named hereafter as KV01, KV05, KV1, KV2, KV3, KV4 and KV5. κ_v is changed instantenously from the control run to new value of κ_v.

4.1 Sensitivity to Diapycnal Diffusivity

4.1.1 Strength of the Meridional Overturning Circulation

All experiments, except that with KV01, show some NADW formation between 40°N and 60°N. This suggests that in the model a minimum amount of diapycnal mixing is required to form NADW. With the increase in κ_v, convection at northern latitudes

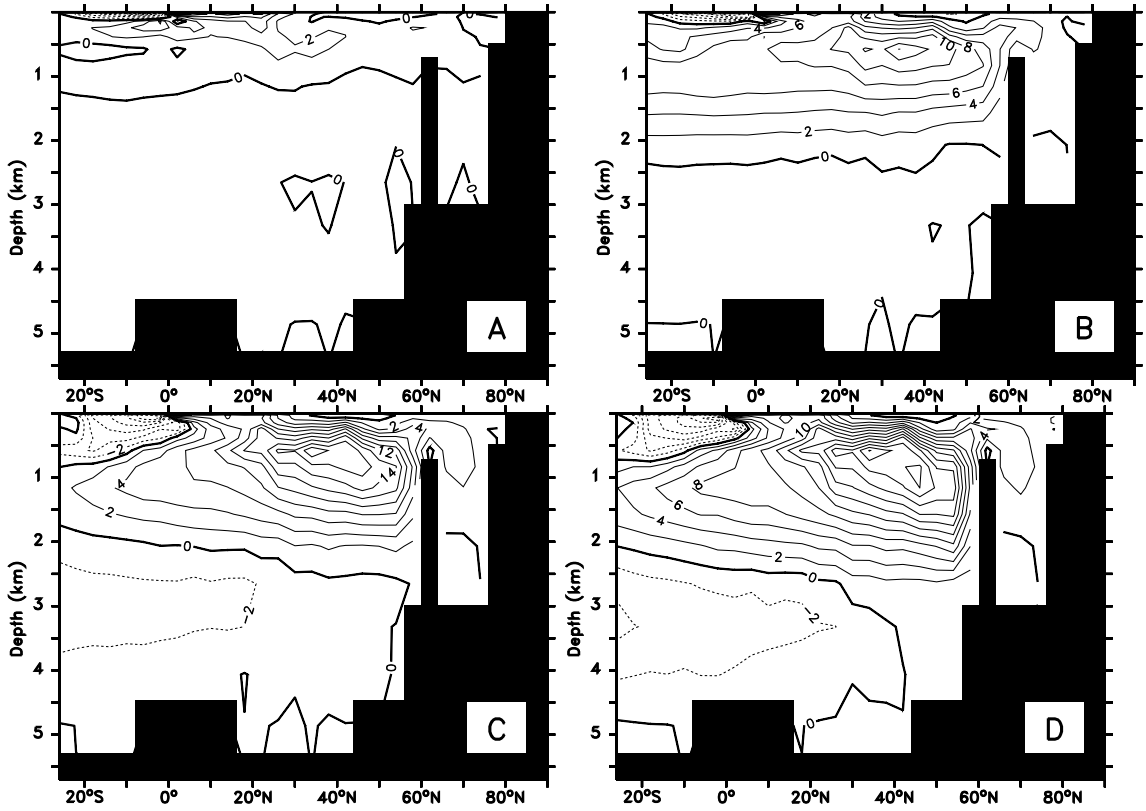

Figure 4.1: *Meridional overturning strength in Sv for the Atlantic ocean for KV01 (A), KV05 (B), KV3 (C) and KV5 (D); positive values correspond to clockwise circulation, negative values correspond to counter-clockwise circulation; contour interval: 2 Sv.*

is intensified. Moving from KV01 to KV5, the Irminger Sea shows an increase in convection strength and an increase in the maximum depth of the convection, up to 2000 m (fig. 4.1). Sinking in the Labrador Sea only occurs for the highest values of κ_v. The frequency of convection in the Norwegian Seas increases by 50% from KV01 to KV5, but the overflow between the Greenland-Scotland ridge remains fairly constant (4 Sv in the control, 4.2 Sv in KV5). The inflow of AABW to the Atlantic ocean increases. The outflow at 30°S decreases from 5 Sv for KV1 to 1.3 Sv for KV2, and increases to 4 Sv for KV5. The ratio of the strength of the AABW at 30°S to the maximum strength of the MOC is 38% in KV1, smaller than the 73% observed in reality. When $\kappa_v \geq 1 cm^2/s$, this ratio decreases and varies between 10 and 17% in the different experiments. All the meridional overturning cells in the Atlantic basin increase in strength with κ_v; the subtropical cell also shows an increase in intensity (table 4.1).

As κ_v increases, the Indo-Pacific Ocean develops northern and southern over-

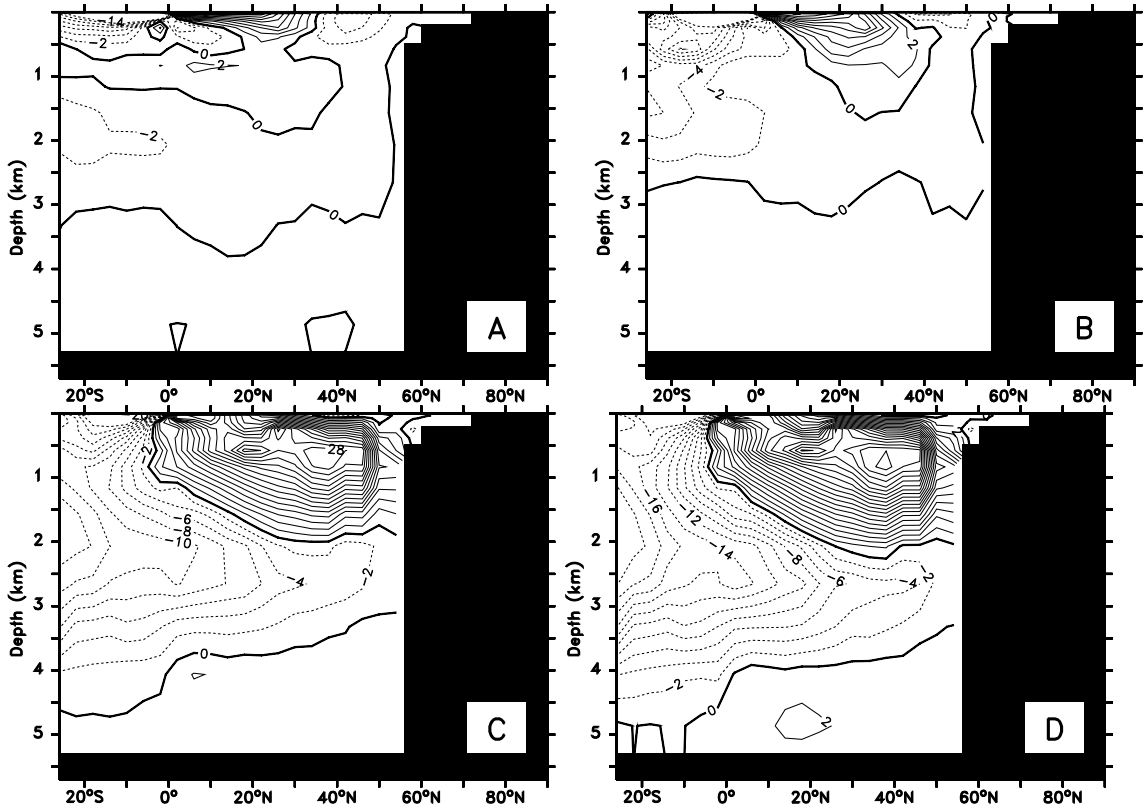

Figure 4.2: *Meridional overturning strength in Sv for the Indo-Pacific ocean for KV01 (A), KV05 (B), KV3 (C) and KV5 (D); positive values correspond to clockwise circulation, negative values correspond to counter-clockwise circulation; contour interval: 2 Sv.*

turning cells, with upwelling at the equator (figure 4.2). The northern cell has a maximum at 40-45°N with 39 Sv for KV5. An overturning cell in the southern basin with stronger strength and deeper depths is found for $\kappa_v \geq 2cm^2/s$. The subtropical overturning cell decreases in the south of the basin and increases in the north (table 4.1). The cross-equatorial transport is very weak for intermediate water but increases with κ_v for the deeper cell. This two cell structure with little cross equatorial transport is reminiscent of the advective-diffusive basins used in the simple scaling theory (Defant, 1961). We might therefore expect a simple ψ, κ_v scaling to apply in the Indo-Pacific.

Combining the results already seen for the Atlantic and the Indo-Pacific, the global overturning shows a strong increase in both hemispheres as κ_v is increased (fig. 4.3). In the Southern Ocean, there is a very strong and deep overturning cell with a strength of 40 Sv for KV5. The Deacon cell in the ACC region decreases in strength and becomes much shallower and confined to the upper layers as κ_v

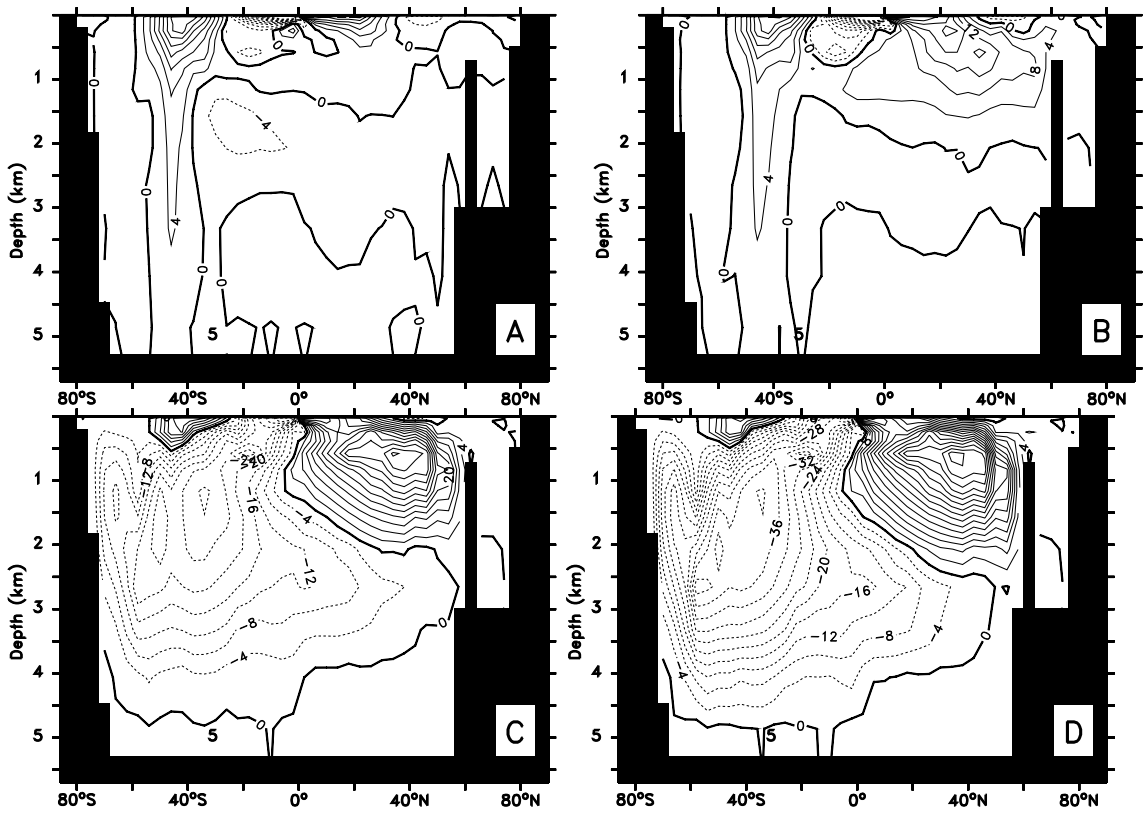

Figure 4.3: *Meridional overturning strength in Sv for the global ocean for KV01 (A), KV05 (D), KV3 (D) and KV5 (D); positive values correspond to clockwise circulation, negative values correspond to counter-clockwise circulation; contour interval: 4 Sv .*

increases. The Southern Ocean has strong convection in the Amundsen Sea. This convection is linked to the strong changes in the fresh water cap and melting of the sea ice in the Southern Ocean and the deepening of the thermocline.

4.1.2 Power Laws

Previous studies have suggested that ψ increases with κ_v according to a power law (eg. Bryan (1987), Marotzke (1997), Weber (1998)). In our experiments, considering each ocean basin separately however does not produce a power law for values of $\kappa_v \leq 1cm^2/s$, but only for $\kappa_v \geq 1cm^2/s$ (figure 4.4) (except for the Southern Indo-Pacific). Calculating values using only results from experiments with $\kappa_v \geq 1cm^2/s$, we find different power laws for each basin (table 4.2). For the highest values of κ_v, the circulation has stronger sinking at high latitudes and more upwelling in the equatorial regions. It also tends to be more symmetric around the equator, which is

κ_v (cm^2/s)	North Atlantic	South Atlantic	North Pacific	South Pacific
0.1	14.2	−10.9	16.3	−44.8
0.5	16.5	−12.2	21.2	−47.4
1	15.9	−12.9	25.6	−37.2
2	14.7	−13.4	27.1	−30.3
3	15.8	−14.4	26.3	−28.3
4	16.6	−15.7	29.7	−30.2
5	17.1	−16.3	32.1	−33.0

Table 4.1: *Sub-tropical overturning strength in Sv for the different values of κ_v; positive values correspond to clockwise circulation, negative values correspond to counter-clockwise circulation, viewed from the east.*

why we have taken the approach of considering the hemispheres separately. In these cases, the contribution by the mixing is much stronger than that by the wind, where the shallow tropical cells stay confine to the upper levels. The overturning cells in the north Atlantic and south Indo-Pacific scale with power of $\psi \propto {\kappa_\nu}^{0.48}$. The overturning cells are more sensitive in the southern Atlantic and northern Indo-Pacific, with a stronger power law of $\psi \propto {\kappa_\nu}^{0.6}$; these basins develop new convection regions as κ_v increases. For the lower values of $\kappa_v \leq 1 cm^2/s$, the strength of the overturning does not fit the power law, except in the south Indo-Pacific; for these values of κ_v, the overturnings have a relatively high cross-equatorial mass transport and shallow overturning cells. We can calculate a power law for the "global overturning" by summing the absolute strength of the overturning in each individual hemispheric basin (fig. 4.4 left). The global overturning strength scales as $\psi \propto \kappa_\nu^{0.54}$ for all values of κ_v. This is surprising considering that the individual ocean basins do not follow a power for weaker values of κ_v; or the sums of absolute magnitude in North plus South Atlantic, or North plus South Indo-Pacific (fig. 4.4 right). Where the total Atlantic and total Pacific MOC strengths do deviate from the scaling law (at $\kappa_v \leq 1 cm^2/s$) it appears that some compensation occurs between the two basins that allows the global sum to still follow the scaling.

This power law does not include the dependence of the $\Delta\rho$ with κ_v included in the theory. The dependence of $\Delta\rho$ is looked at a depth of 700 m while the $\Delta\rho$ at the surface is too influence by the wind and surface fluxes fluctuations. The $\Delta\rho$ is calculated by the zonally averaged difference between 50°N and 5°N for the northern basin and 30°S and 5°S for the southern basin. For the global ocean, we consider the difference between 30°S and 50°N (fig. 4.5). A power law of the $\Delta\rho$ with κ_v

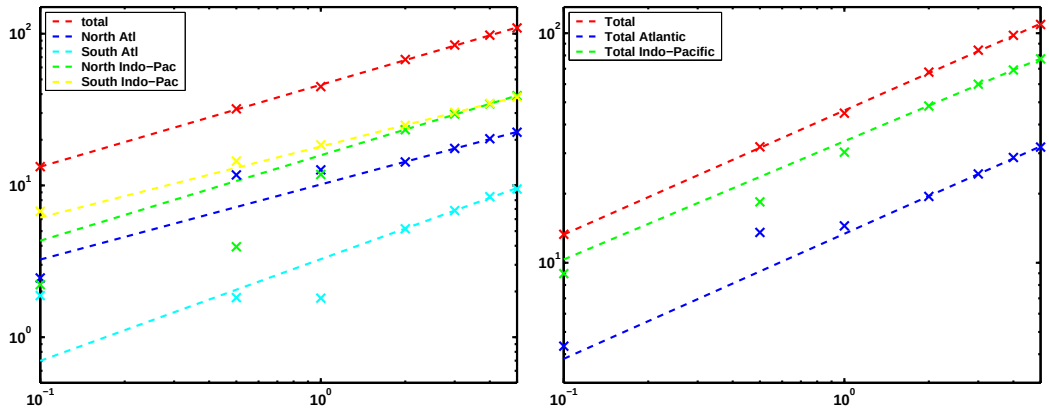

Figure 4.4: *Power law of the maximum strength overturning (Sv) versus κ_v in each ocean basin (left) and the Atlantic/Indo-Pacific sums (right). The dashed lines represent the best fit of ψ with κ_v for κ_v>1cm^2/s .*

is found for each ocean basin; where $\Delta\rho \propto \kappa_v^{0.44}$ for the total ocean, $\Delta\rho \propto \kappa_v^{0.55}$ for the north Atlantic ocean, $\Delta\rho \propto \kappa_v^{0.005}$ for the south Atlantic ocean,$\Delta\rho \propto \kappa_v^{1.15}$ for the north Pacific ocean and $\Delta\rho \propto \kappa_v^{0.17}$ for the south Pacific ocean (table 4.2). Correcting the previous power law with the dependence of $\Delta\rho$ with κ_v, the following power law is found: $\psi \propto \kappa_v^{0.4}$ for the total ocean, $\psi \propto \kappa_v^{0.36}$ for the north Atlantic ocean, $\psi \propto \kappa_v^{0.66}$ for the south Atlantic ocean,$\psi \propto \kappa_v^{0.18}$ for the north Pacific ocean and $\Delta\rho \propto \kappa_v^{0.4}$ for the south Pacific ocean

The power law 2/3 suggested by previous studies is derived from assuming vertical advective-diffusive balance is not found in our study but the scaling for the global ocean is found very robust. Our results suggest that this is not valid for all values of κ_v and that other aspects of the system are involved. No other previous studies found a basin compensation even when the experiments are undertaken with multi ocean basins.

4.1.3 Ocean Heat and Freshwater Transport

We now look at the response of the heat and freshwater transports to the diapycnal diffusivity in the different experiments. The advective transport can be decomposed into an overturning transport part and a gyre transport part (Bryden and Imawaki, 2001). Diffusion in the model is found to be negligible compared to the advective transport.

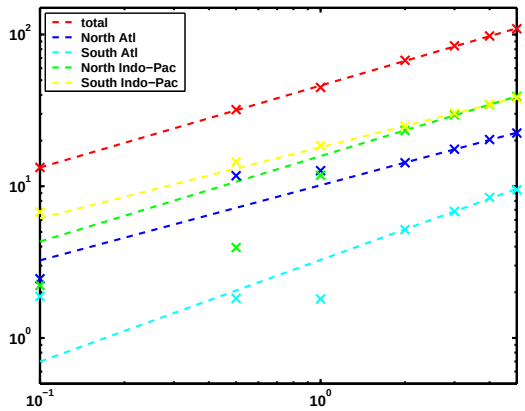

Figure 4.5: *Power law of the equator-pole density difference versus κ_v in each ocean basin (left). The dashed lines represent the best fit of ψ with κ_v for κ_v>1cm^2/s .*

basin	α	β	γ
Total	0.54	0.44	0.39
Total Atlantic	0.55	0.42	0.41
Total Indo-Pacific	0.51	0.58	0.32
North Atlantic	0.49	0.55	0.36
South Atlantic	0.67	0.005	0.66
North Indo-Pacific	0.56	1.15	0.18
South Indo-Pacific	0.47	0.17	0.41

Table 4.2: *α is the power law following $\psi \propto \kappa_v^\alpha$ for each ocean basin, total Atlantic and Indo-Pacific and total ocean basin.*

The advective heat transport in the global ocean (fig. 4.6) shows a very high sensitivity to κ_v in the southern hemisphere, with an increase in the Southern Ocean from 0.3 PW for KV01 to 2 PW for KV1 and 7 PW for KV5, mainly from the overturning component. The northward heat transport in the northern hemisphere shows a much weaker sensitivity and increases by less than 1 PW from 0.8 PW for KV01 to 1 PW for KV1 and to 1.5 PW for KV5. In the Atlantic, the southward advective heat transport increases in the southern tropics by 0.1 PW and the northward heat transport increases by 0.35 PW between 40°N and 60°N and between the experiments KV1 and KV5; in KV01 the overturning component shows a very different patterns due to the lack of overturning circulation for this run. In the Indo-Pacific basin, the heat transport is most sensitive in the southern hemisphere, with an increase of the southward heat transport of 3.5 PW between KV1 and KV5, for KV01 an northward heat transport of 0.8 PW is found. The northward heat transport increases by approximately 1 PW between experiments KV01 or KV1 and KV5 at latitudes between 40°N and 50°N. The very weak transport for KV01 is directly linked to the practically non-existent overturning circulation. The gyre components of the heat transport are an order of magnitude smaller than the overturning parts and a general decrease is observed at the different latitudes as κ_v increases, except for a small increase in the North Indo-Pacific.

The southern hemisphere fresh water transport shows a reduction with increasing κ_v in the mid-latitudes and tropical regions; the northern hemisphere show very little change (fig. 4.6). The reduction in freshwater transport in the Southern Ocean could be the cause of the increase in convection around Antarctica. The Indo-Pacific freshwater transport changes account for most of the changes in the tropical regions. These changes can be related to the disappearance of the ENSO-like phenomena in this region, discussed in detail in the next section. The Atlantic ocean shows only minor changes.

4.2 Climate Response

4.2.1 Atmospheric response

The atmospheric circulation is expected to respond to the changes in the SST induced by the enhanced oceanic mixing. The surface air temperature (SAT) becomes

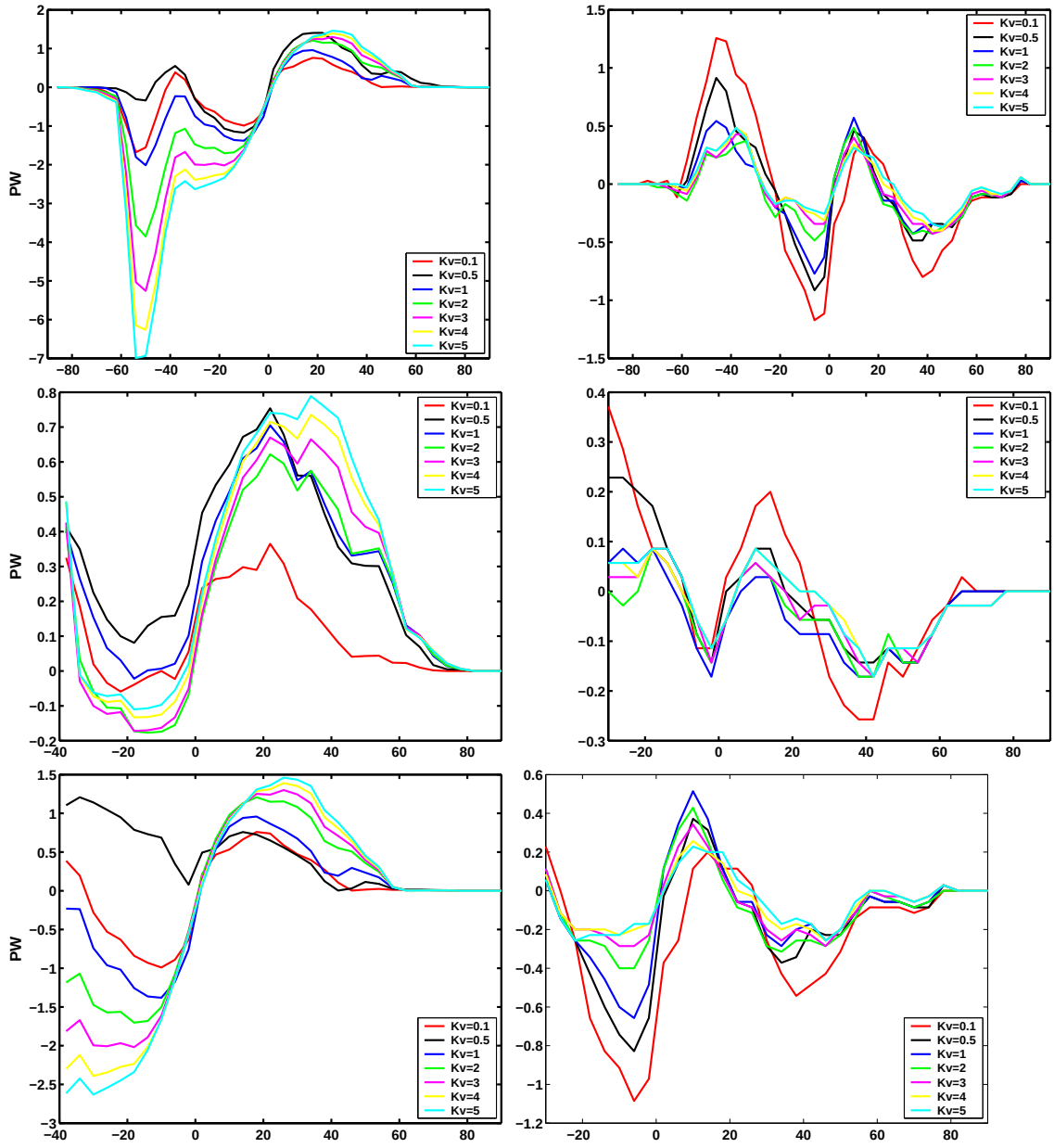

Figure 4.6: *Heat transport in PW for the global ocean (top left), Atlantic ocean (middle left) and Indo-Pacific ocean (bottom left) and freshwater transport in Sv for the global ocean (top right), Atlantic ocean (middle right) and Indo-Pacific ocean (bottom right).*

κ_v (cm^2/s)	0.1	0.5	1	2	3	4	5
Surface temperature (^0C)	14.38	15.22	15.82	16.94	17.24	17.42	17.5
Surface albedo	0.155	0.151	0.147	0.143	0.143	0.142	0.142
SAT by changes in surface albedo (^0C)	15.16	15.55	–	16.13	16.18	16.22	16.51
Planetary albedo	0.322	0.318	0.317	0.316	0.315	0.315	0.314
Longwave transmissivity	0.592	0.586	0.581	0.571	0.567	0.565	0.563

Table 4.3: *Effect of changing κ_v on global mean properties. Shown are changes of surface temperature, surface albedo, surface air temperature changes by the changes in albedo compared with the control run, planetary albedo and longwave transmissivity for the different values of κ_v.*

generally warmer than that of the control run (KV1) as κ_v increases and colder as κ_v decreases. Compared to KV1, in KV5 the SAT at the poles is 10°C higher, and at the equator is 2°C lower. The global average SAT also increases from 14.4°C for KV01 to 17.5°C for KV5 (table 4.3).

As a consequence of the net surface temperature increase with κ_v, the sea ice disappears in the Southern Ocean and is also reduced in the Arctic Ocean for higher κ_v. There is a noticeable change of surface albedo caused by the change in the ice and snow cover at high latitudes in northern Europe, Asia and North America. The global average surface albedo decreases by ˜3% from 0.147 for KV1 to 0.142 for KV5. The decrease in the planetary albedo (˜1%) is smaller compared to the change in the surface albedo. This can be associated with the increase in the atmospheric temperature, associated with an increase in water vapour and clouds. The model can simulate low, mid, high altitude and convective clouds. All of them show an increase in the average coverage fraction, which are responsible for the weaker increase in the planetary albedo compared to the increase in surface albedo. There is also an increase in the amount of longwave radiation absorbed by the atmosphere. The longwave transmissivity ε_L is given by: $\varepsilon_L = \frac{LW_{up}^{TOA}}{LW_{up^{BOA}}}$, where LW_{up}^{BOA} is the globally averaged amount of longwave radiation emitted by the Earth's surface and LW_{up}^{TOA} is the amount emitted from the top of the atmosphere. The longwave radiation transmissivity decreases as κ_v increases. This is due to the increased water vapour content of the atmosphere as κ_v increases, which strengthens the greenhouse effect.

The global average rainfall does not change, but the spatial distribution of the rainfall shows strong differences between KV01 and KV5. The Indo - Pacific ocean

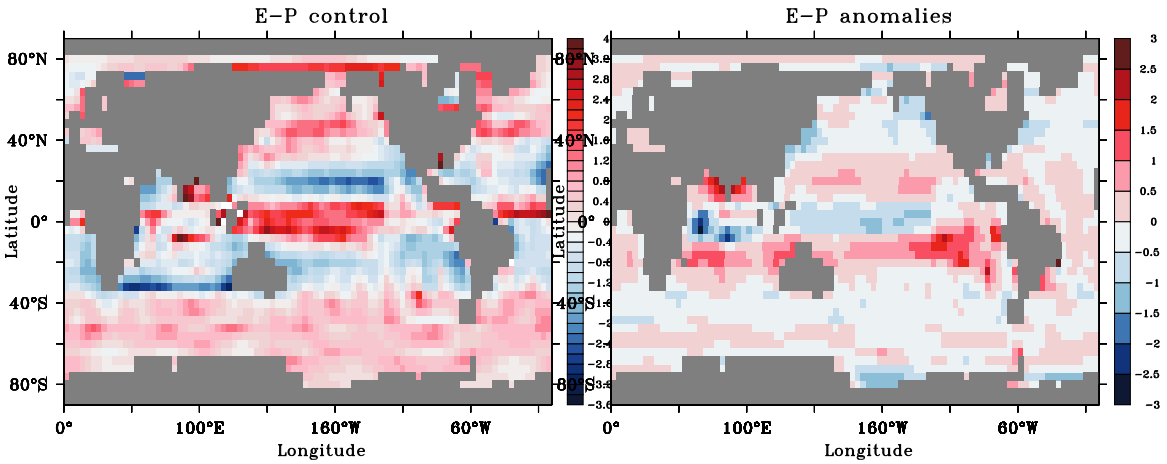

Figure 4.7: *Precipitation minus Evaporation (P-E) in the control run (KV1) (left); difference of P-E between KV5 and KV1 in m/year..*

shows the biggest changes, with a strong decrease in the rainfall in the Equatorial Western Pacific and Equatorial Indian ocean by 2 m/year between KV1 and KV5 and an increase of the same amount in the Eastern Pacific. The highest latitudes receive more rainfall, around 1 m/year for KV5, except the North Atlantic.

The behavior of the climate system in the Pacific is dominated by the ENSO-like phenomenon. As κ_ν increases, the depth of the thermocline in the equatorial region increases. In the control run, oscillations between El Niño and La Niña conditions are observed, but as κ_ν increases, these oscillations disappear (fig. 4.8). The relaxation of the eastward winds during El Niño allows the warm water in the equatorial region to flow back eastward. As κ_ν increases, the thermocline deepens and less cold water can be upwelled in the east; the SST gradient along the equator therefore decreases. As the zonal temperature gradient decreases it directly affects and weakens the trade winds and the Walker and Hadley circulations. Changes in κ_ν strongly control the existence of the ENSO-like phenomenon in the model.

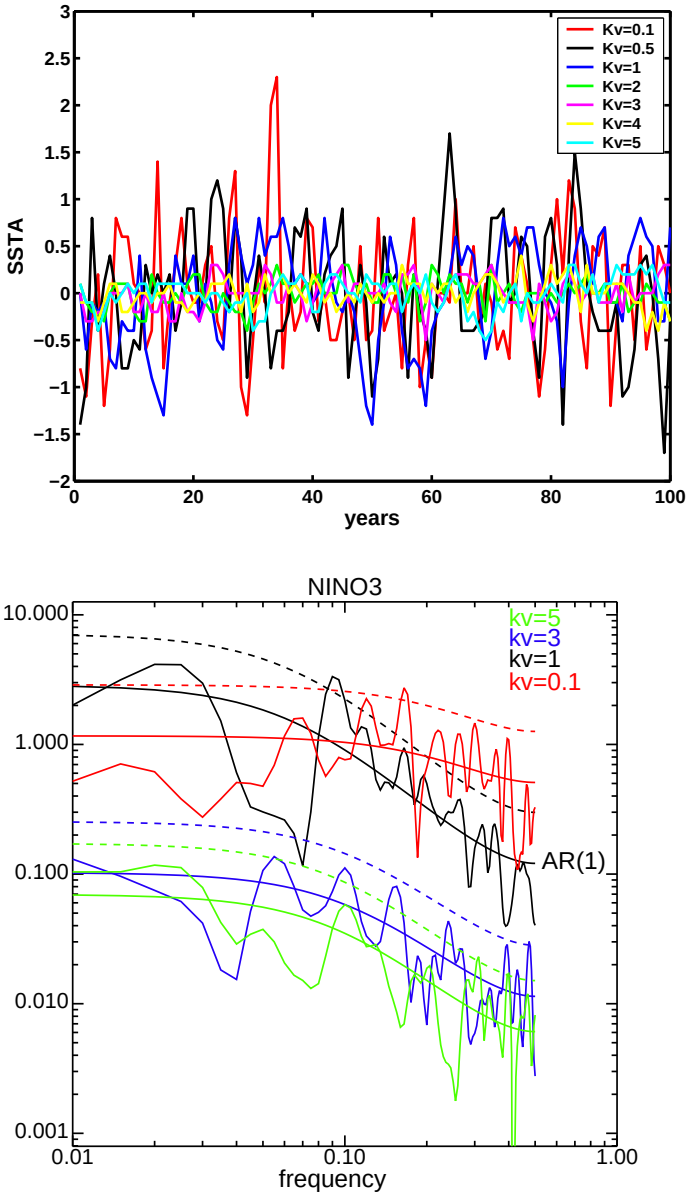

Figure 4.8: *Average SST anomalies between 6° N and 6° S and from 152° W and 90° W in the Eastern Equatorial Pacific as a function of time (° C). Associated spectra for KV01, KV1, KV3 and KV5 and their associate confidence interval of 90% .*

4.2.2 Atmospheric Meridional Transport

An important component of the atmospheric circulation is the meridional energy transport. Bjerknes (1964) suggested that the total energy transport in the climate system should remain constant and an intensification in the oceanic meridional heat transport would be compensated by a corresponding decrease in the atmospheric energy transport. Other studies supported for this theory (Manabe et al., 1975; Stone, 1978; Clement and Seager, 1999; Smith et al., 2006). In our model, the SAT gradient between the equator and the poles is reduced with increasing κ_ν (figure 4.9), which in turn weakens the mean meridional atmospheric circulation (figure 4.10). There is a reduction of the mean meridional atmospheric circulation from 8×10^{10} kg/s to 4×10^{10} kg/s in the southern hemisphere and from $8\times10^{10}kg/s$ to 6×10^{10} kg/s in the northern hemisphere between KV01 and KV5 (fig. 4.11 left). As a result, the atmospheric energy transport also decreases with κ_ν. We have seen however that the ocean heat transport increases with κ_ν; the total energy transport of the system also increases, implying that the atmosphere is unable to compensate completely for the increase in ocean heat transport (fig. 4.11 right). The decrease of 1 % of the planetary albedo should lead to a similar decrease of the total energy flux (Stone, 1978), but it is associated by a decrease of 1 PW in the atmospheric energgy transport from KV1 to KV5 and an increase from 4.2 PW for KV1 to 4.9 PW for KV5 for the total system energy transport. The compensation between the ocean and atmosphere does not follow previous finding from Shaffrey and Sutton (2004) and Shaffrey and Sutton (2006). They found a Bjerknes compensation for decadal time-scale at high latitudes but on interannual time-scale. In the experiments conducted with FORTE suggest that the Bjerknes compensation does not hold for very different state of the ocean configuration. Stone (1978) suggested that the total system transport will stay constant as long as a number of factors, including the hemispheric mean albedo, are constant. Whilst the other factors cited by Stone (orbital parameters) remain constant in our model, the melting of snow and sea ice as κ_ν increases does change the albedo. Our hemispheric mean albedo thus is not constant and this explains why perfect compensation is not found.

The winds in the model are free to respond to the change of the ocean state as κ_ν changes. The global zonal average windstress is reduced in the tropical regions in both hemispheres, as well as in the high latitudes and mid latitudes of the southern hemisphere (fig. 4.12) which is link to the reduction of the atmospheric circulation

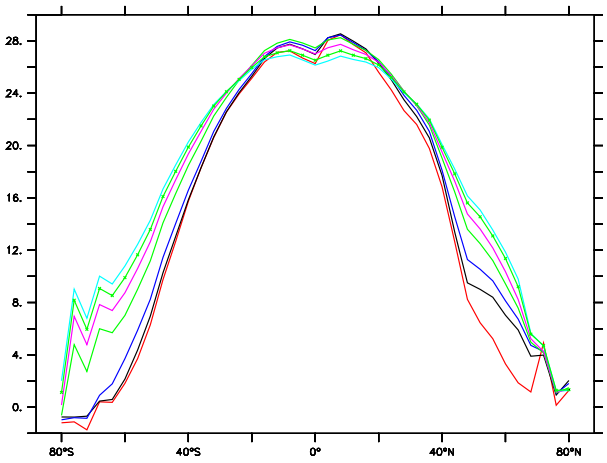

Figure 4.9: *Zonal SST for the different experiments .*

as κ_ν increases. The changes in the global average windstress are mainly due to the changes over the Pacific ocean as has been looked at in the discussion of the ENSO-like phenomenon. The global zonal Ekman transport decreases in the tropical regions by 3 Sv in the southern hemisphere between KV01 or KV1 and KV5. The weakening in the Ekman transport in turn causes a reduction in the surface layers of the oceanic meridional overturning streamfunction. The Ekman transport in the ACC is also reduced by 2 Sv from KV1 to K5.

4.3 Discussion

This study looks at the sensitivity of the climate system to κ_ν in a global atmosphere-ocean general circulation model. Previous sensitivity studies to κ_ν have been done with various models, including sophisticated ocean models, but not with an AOGCM. We show that the coupled model, including its atmospheric component, is strongly sensitive to κ_ν.

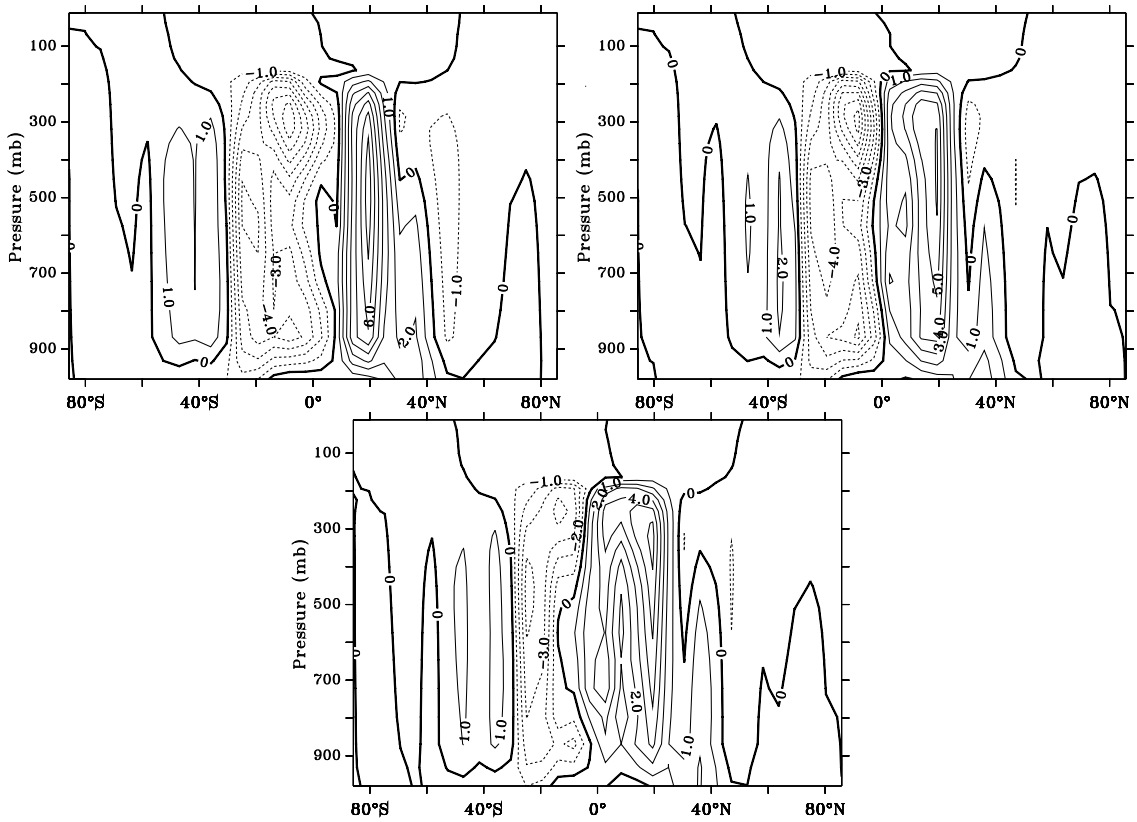

Figure 4.10: *Atmospheric meridional circulation for KV01 (top left), KV1 (top right) and KV5 (bottom), units in 10^{10} kg/s. The vertical coordinate of the IGCM data are sigma levels, which give an indication of pressure (mb) .*

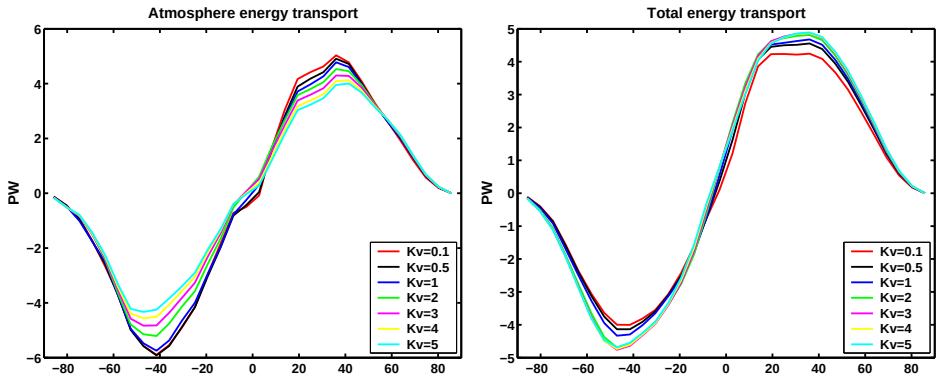

Figure 4.11: *Atmospheric (left) and total (right) energy transport in PW for the different values of κ_ν (cm^2/s) .*

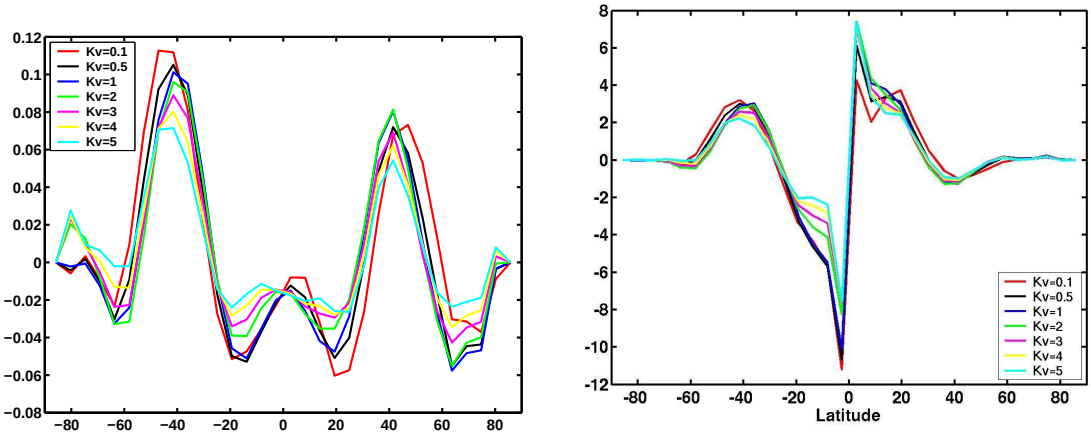

Figure 4.12: *Global zonal mean windstress (N/m^2) (left) and associated meridional Ekman volume transport (Sv) (right) for the different sensitivity experiments with changing κ_ν (cm^2/s).*

Previous studies have shown that κ_v is important and a crucial parameter of the ocean circulation (Bryan (1987) and Scott and Marotzke (2002)) abd found from theoritical argument that $\psi \propto \kappa_\nu^{2/3}\rho^{1/3}$ (Marotzke, 1997). All previous sensitivities studies have been undertaken with simple basin OGCM ((Marotzke, 1997) and (Park and Bryan, 2000)) or with multi-ocean basin ((Weber, 1998) and (Wright and Stocker, 1992)). Only recently, more studies with realistic topography and simplified AGCM have been caried out ((Prange et al., 2003), (Dalan et al., 2005) and (Mignot et al., 2006)). In our study, each single basin does not, however, follow a power law for $\kappa_v \leq 1cm^2/s$, only for $\kappa_v > 1cm^2/s$ for those higher value κ_v controls the circulation and other effects such as the wind or surface fluxes are minimised. None of the individual basins follow the expected $\psi \propto \kappa_\nu^{2/3}$ law predicted by simple advective-diffusive theory. The power scaling for the global overturning is found very robust which suggests that the advecttion-diffusion relation is valid for the global overturning and not just for the north Atlantic. Multiple basins should be considered in the scaling analysis, with upwelling and downwelling occurring in regions other than the North Atlantic. This behaviour can explain the compensation between the Atlantic and the Pacific. The power scaling as to consider the dependence of $\Delta\rho$ with κ_v which gives a power scaling of $\psi \propto \kappa_\nu^{0.4}$ for the global overturning.

Toggweiler and Samuels (1995) and Klinger et al. (2003) among other, found an increase in the NADW when the windstress is increased in the ACC region. Gnanadesikan (1999) proposed a cubic scaling relationship between the depth of

the overturning and the wind stress over the ACC. This scaling does not consider changes in the wind in other parts of the ocean. Tsujino and Suginohara (2001) applied changes in windstress in the northern hemisphere over an idealized single ocean basin. In their study, they also found that an increase in the wind forcing is responsible for enhancing the thermohaline circulation. In our experiments, the Indo-Pacific windstress is sensitive to increasing κ_ν, but the Atlantic windstress is not. This suggests that transport by the gyres and in the ACC region needs to be considered in the scaling analysis and that the fully coupled ocean-atmosphere system should be considered. This can be due to major changes on coupled phenomena, where a cessation of the ENSO-like phenomenon is observed as κ_v increases. The southward freshwater transport in the south Indo-Pacific is strongly reduced as κ_v increases as well as the precipitation which induce deep convection and a strong overturning in the south Indo-Pacific. Nevertheless, the coarse resolution of the model could however be amplifying this response as the equatorial Pacific is represented by only 3 grids boxes in the meridional direction.

Climate models which aim to represent the present day climate and predict future climate have to properly represent diapycnal mixing processes. We have seen a number of feedbacks from the coupled system, but the sophistication of the model imposes some limits. At the resolution used by FORTE, small scale processes are parameterised with a coarse resolution and we use a constant value of the mixing. The uniform mixing used in the model is unrealistic and does not admit the feedbacks from the atmospheric winds, ocean static stability, or current shear on the values of the mixing itself. Similar experiments to those described here will be carried out in a more sophisticated model, to confirm the results obtained with FORTE.

4.4 Conclusions

1. The MOC-κ_ν scaling found analytically does not hold for the individual basins. Scaling is found for κ_v>$1cm^2/s$, but not with the predicted exponent, except in the South Atlantic. The Souh Atlantic and North Indo-Pacific overturning cells are more sensitive to κ_ν than the ones in the north Atlantic and South Indo-Pacific.

2. The global MOC scales with $\psi \propto \kappa_\nu^{0.4}$ for all values of κ_ν, which can explain the compensation between the Atlantic and Pacific basins.

3. A strong overturning in the south Indo-Pacific appears as κ_v increases caused by a cessesion of the ENSO-like phenomena.

4. Ocean energy transport increases with κ_ν; some reduction in atmospheric energy transport occurs, but there is no full compensation because of changes in surface albedo.

Chapter 5

ECHAM5/MPI-OM Experiments

The previous chapter shows that changes in κ_v have an impact on the climate system. However, FORTE uses a rather simple parameterisation of κ_v which does not allow feedbacks of the mixing parameterisation itself and has to use flux adjustments. Similar sensitivity experiments to the FORTE ones are conducted using a state-of-the-art AOGCM: ECHAM5/MPI-OM. The ECHAM5/MPI-OM model has a widely used control run and does not use flux adjustments (Marsland et al., 2003). The mixing parameterisation in the ocean is more complex, as described in chapter 2. To stay as close as possible to the experiments undertaken with FORTE, only the background diffusivity, κ_b, is varied in MPI-OM model, which is also constant over the whole ocean basin. Due to computational cost only 3 coupled experiments are integrated, compared to 7 with FORTE.

The overturning circulation is found to reduce as the κ_b increases in the experiments using the coupled model but not in the ocean only experiments. This counter-intuitive result will be described and discussed in the following chapter. Six experiments are undertaken with $\kappa_b = 0.1\ cm^2/s$ (control run), $\kappa_b = 0.25\ cm^2/s$ and κ_b

$= 1\ cm^2/s$ and are named hereafter as EXP0.1coup, EXP0.25coup and EXP1coup for the coupled experiments and EXP0.1oce, EXP0.25oce and EXP1oce for the ocean-only experiments respectively.

5.1 Strength of the Meridional Overturning Circulation

5.1.1 MOC - Ocean-only Experiments

The ocean-only experiments are forced with the OMIP forcing (Röske, 2001) and κ_b is changed instantenously after 200 years of control run. From this model year, the experiments are integrated for another 460 years.

As expected from previous experiments, the overturning circulation in the Atlantic increases as κ_b increases (figure 5.1). The timeseries of the maximum MOC strength show a rapid increase as κ_b increases. Within 250 years, the maximum MOC strength stabilises for EXP1oce, and very weak changes are observed in EXP0.25oce compared to EXP0.1oce. The strength of the maximum MOC stabilises at 21 Sv for EXP1oce, 16 Sv for EXP0.25oce and 15 Sv for EXP0.1oce.

The MOC is looked at for the different ocean basins, averaged over the last 10 years of integration. The global MOC in the ocean-only experiments shows a significant increase from EXP0.1oce to EXP1oce (figure 5.3). In the northern hemisphere, the maximum MOC increases from 15 Sv for EXP0.1oce to 21 Sv for EXP1oce. The latitudes of convection and the depth of the return flow stay the same in all experiments, with convection at 40-45°N at 1000 m depth. EXP0.1oce and EXP0.25oce have similar strengths and locations of the MOC and convection regions. The Antarctic Bottom Water (AABW) cell at 45°S increases from 8 Sv for EXP0.1oce to 12 Sv for EXP1oce. The Deacon cell shows a reduction in its depth from 3500 m in EXP0.1oce to 2000 m in EXP1oce. The shallow equatorial overturning cells deepen and increase in strength as κ_b increases. A reduction of the cross equatorial flow is found as κ_b increases, as also found in the FORTE experiments. At 30°S, 9 Sv in EXP0.1oce reaches the southern ocean compared to none in EXP1oce.

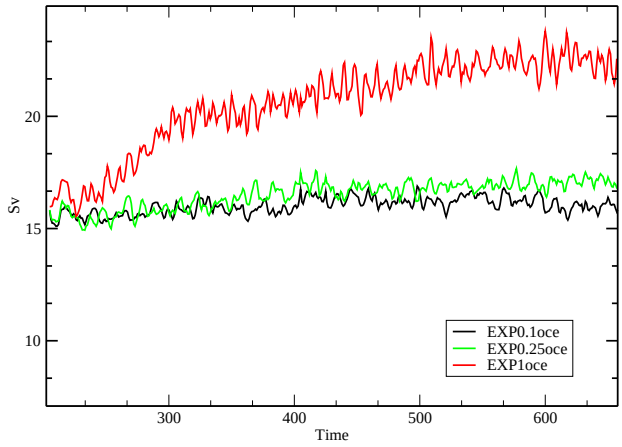

Figure 5.1: *In the ocean-only model, timeseries in years of the strength of the MOC in Sv at 30-35 °N. black: EXP0.1oce, green: EXP0.25oce and red: EXP1oce.*

In the Atlantic Ocean, the overturning circulation increases in strength as expected as κ_b, with its maximum staying at a constant depth of 1000 m increases (figure 5.4). The maximum MOC equals 15 Sv at 40°N in EXP0.1oce and 21 Sv for EXP1oce. The cross-equatorial flow shows a small increase in EXP1oce by 2 Sv compared to EXP0.1oce. The strength of the AABW overturning cell remains constant with a strength of 2 Sv.

In the Indo-Pacific Ocean, no deep overturning cell is observed in any of the experiments (figure 5.4). As κ_b increases, the shallow equatorial overturning cells increase in depth from 700 m in EXP0.1oce to 1000 m in EXP1oce in the northern hemisphere and from 1200 m (in EXP0.1oce) to 2500 m (in EXP1oce) in the southern hemisphere.

5.1.2 MOC - Coupled Experiments

These afore mentioned results from the ocean-only experiments are similar to those found in previous studies, such as those undertaken with FORTE. The same experiments are then conducted using coupled ECHAM5/MPI-OM. The maximum Atlantic maximum MOC for EXP1coup increases in the first 20 years, up to 20 Sv, and then decreases and stabilises to 8 Sv after 460 years of integration. For

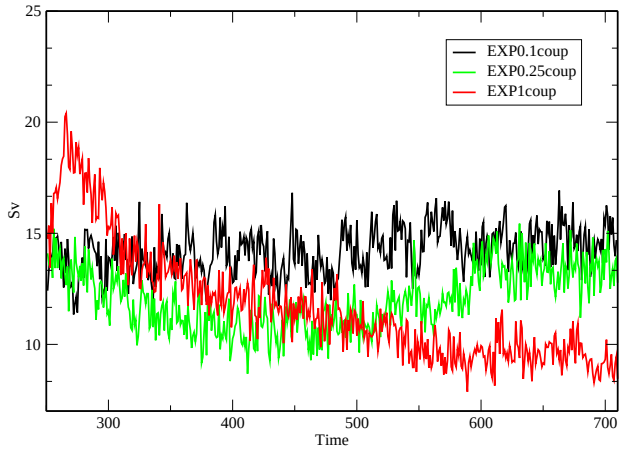

Figure 5.2: *In the coupled experiments, timeseries in years of the maximum strength of the MOC at 30-35 ^0N using the ECHAM5/MPI-OM model. Black: κ_b=0.1 cm^2/s, green: κ_b=0.25 cm^2/s and red: κ_b=1 cm^2/s.*

EXP0.25coup, the strength of the maximum MOC decreases and after 350 years recovers its initial value (figure 5.2). EXP0.1coup has a mean value of 13.5 Sv. The variability of the MOC strength is the coupled experiments is much higher than in the ocean-only experiments. This is explained by the OMIP forcing in the ocean-only experiments, which does not have periods longer than a year. The OMIP forcing has a annual cycle but omits any variabilities such as NAO which is reflected on the MOC variability.

In the global ocean, the overturning cells become more symmetrical around the equator as κ_b increases, which is also observed in the FORTE experiments (figure 5.5). The convection in northern latitudes migrates further northwards from 40°N in EXP0.1coup to 45°N in EXP1coup. The shallow equatorial cells increase in strength and deepen from 500m in EXP0.1coup to 1500 m in EXP1coup. The Deacon cell reduces in depth and strength as κ_b increases from 2500 m in EXP0.1coup to 2000 m in EXP1coup.

In the Atlantic Ocean, the overturning circulation decreases as κ_b increases which is counter-intuitive, in view of our previous experiments (figure 5.6). The strength of the overturning decreases from 15 Sv for EXP0.1coup to 8 Sv for EXP1coup. The

cross equatorial flow significantly reduces as κ_b increases. The intrusion of AABW into the north Atlantic increases by 2 Sv from EXP0.1coup to EXP1coup.

In the Indo-Pacific Ocean, a deep northern meridional overturning cell appears in EXP1coup with an overturning strength of 10 Sv at a depth of 1500 m at 45°N compared to none in EXP0.1coup (figure 5.6). The equatorial cells deepen from 500 m in EXP0.1coup to 1500 m in EXP1coup.

5.1.3 Mixed Layer Depth

The mixed layer depth is calculated by the changes in the potential density profile. The depth calculated corresponds to a change in density of 0.125 kg/m^3 throughout the water column compared to the density at the surface. This choice gives a good representation of the mixed layer depth in the North Atlantic but can give a biased depth where the stratification of the water column is weak such as in the Southern Ocean. In the Southern Ocean, this calculation can give very deep mixed layer depth and large errors due to the large vertical size of the model grid at depth.

In EXP0.1oce, the convection regions in the north Atlantic Ocean, in the Southern Ocean and the eastern Pacific can be clearly seen, with depths around 1000m, between 500 m to 4000 m and to 300 m respectively (figure 5.7 right). As κ_b increases, no new convection regions are observed but an overall increase in the mixed layer depth is seen.

The mixed layer depth shows differences in the convection regions in the north-west Pacific between EXP0.1coup and EXP1coup (figure 5.7 left). A reduction in the mixed layer in the convection regions is observed in the north Atlantic as κ_b increases. In the north west Pacific, a new convection region appears in EXP1coup which explains the presence of the overturning cell in the Indo-Pacific. The mixed layer depth increases in the Southern Ocean as κ_b increases.

5.2 Changes in the Ocean Diffusivity

To understand the change in the overturning strength and mixed layer depth, we examine how the different components of the ocean diffusivity adjust to the increase

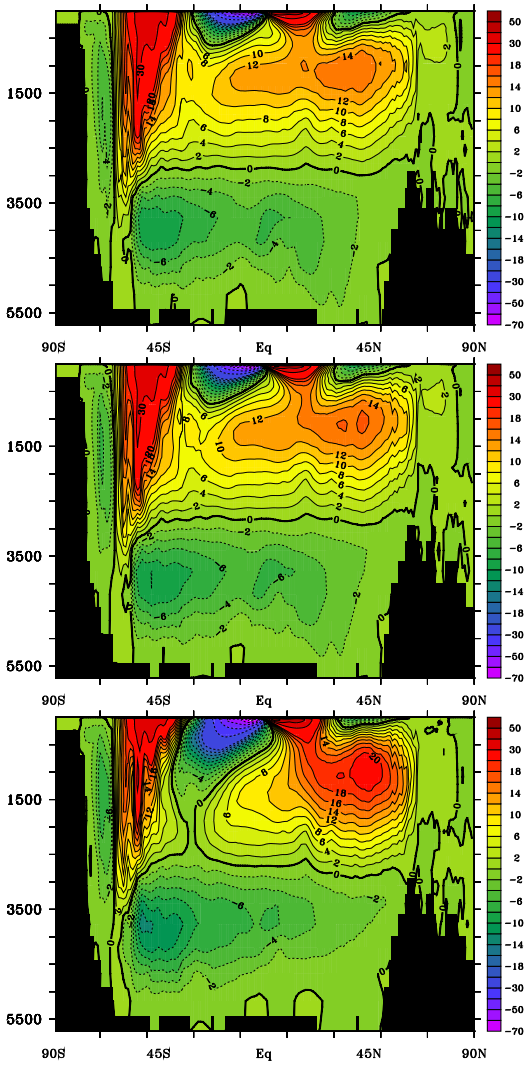

Figure 5.3: *In the ocean-only experiments, meridional overturning strength in Sv for the global ocean for (top) EXP0.1oce, (middle) EXP0.25oce,(bottom) EXP1oce; contour interval 2 Sv.*

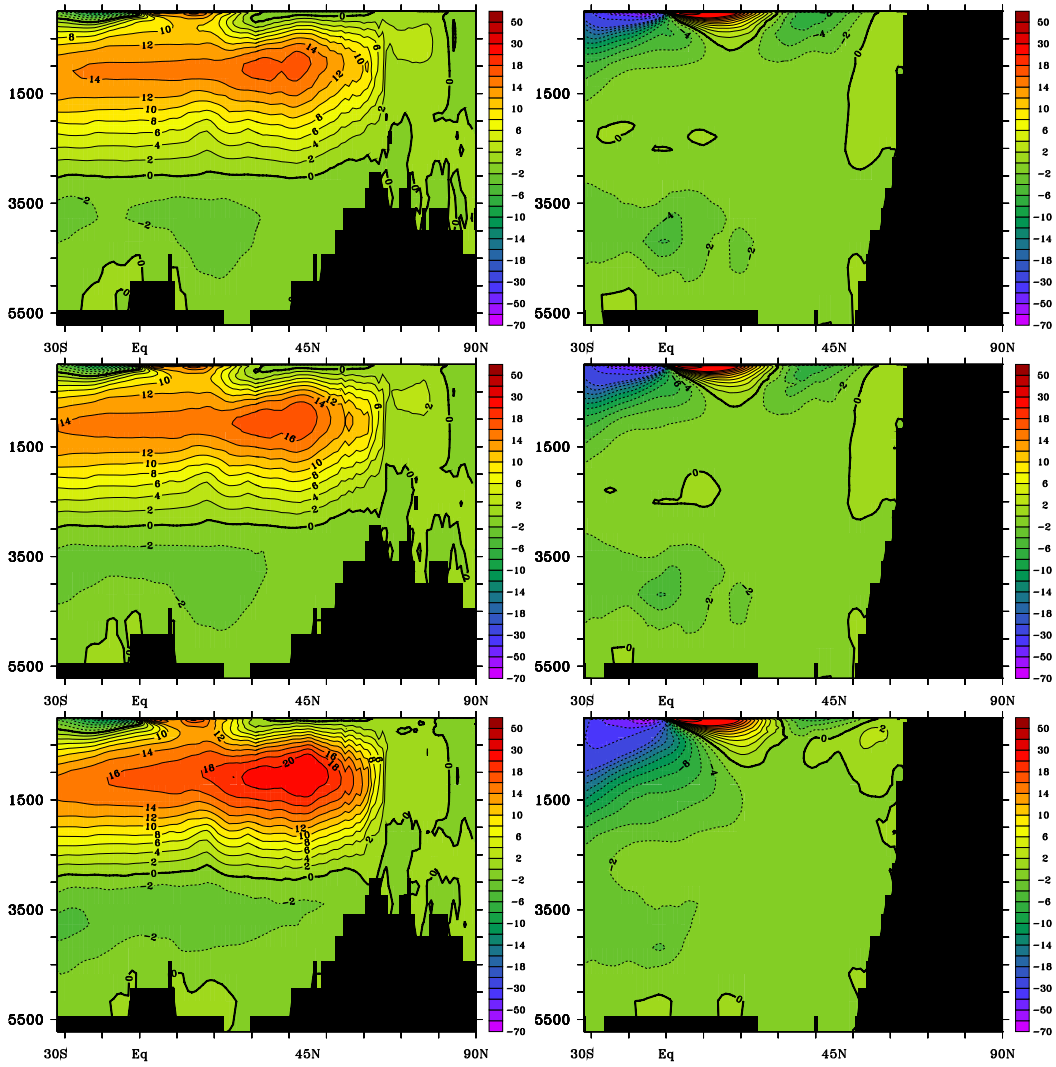

Figure 5.4: *In the ocean-only experiments, meridional overturning strength in Sv for the Atlantic (left) and Indo-Pacific (right) Ocean for (top) EXP0.1oce, (middle) EXP0.25oce, (bottom) EXP1oce; contour interval 2 Sv.*

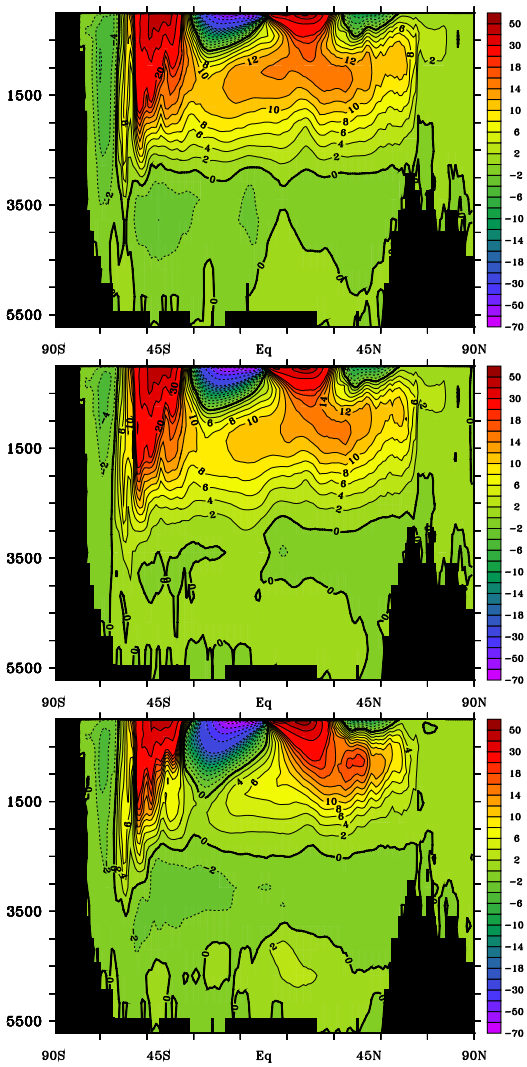

Figure 5.5: *In the coupled experiments, meridional overturning strength in Sv for the global ocean (top) EXP0.1coup, (middle) EXP0.25coup, (bottom) EXP1coup; contour interval 2 Sv.*

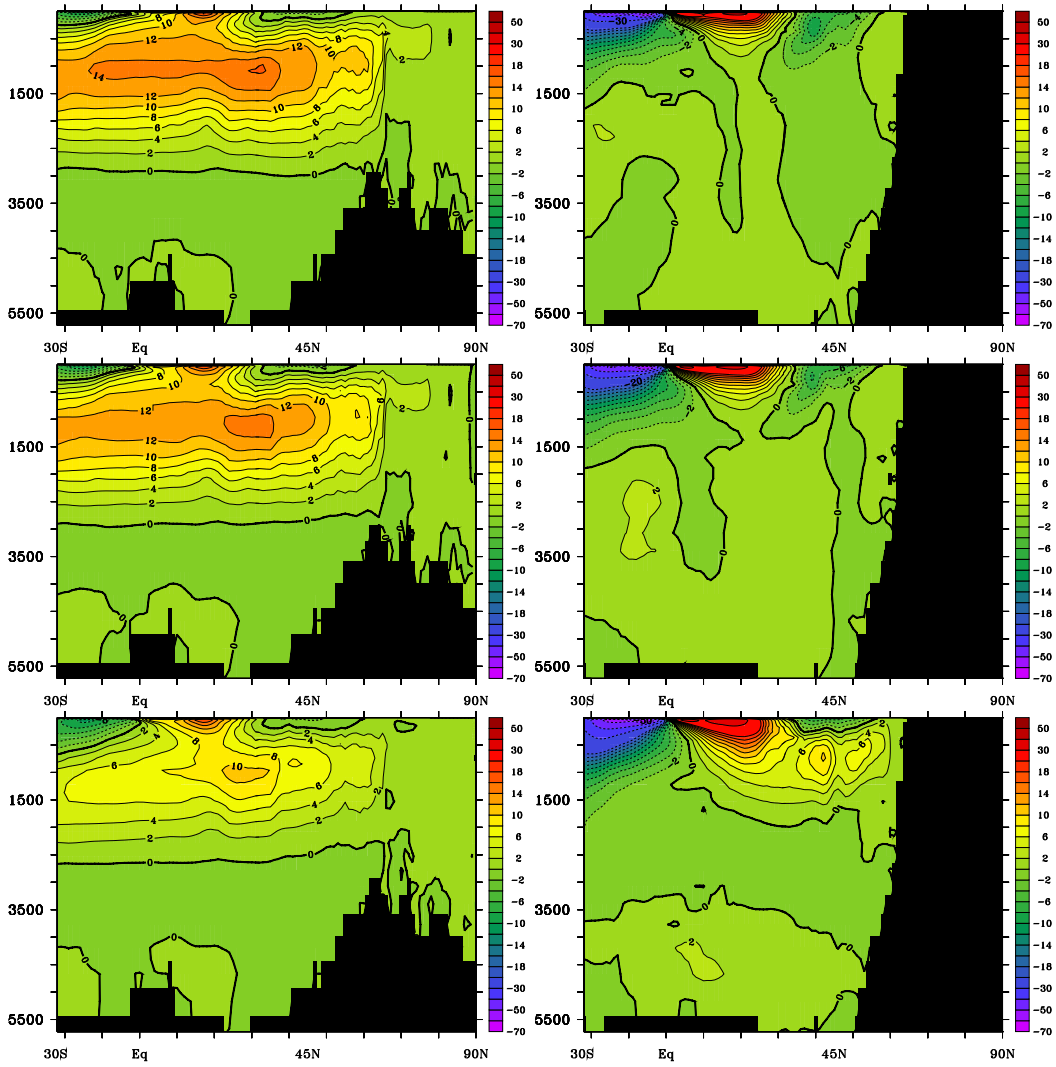

Figure 5.6: *In the coupled experiments, meridional overturning strength in Sv for the Atlantic (left) and Indo-Pacific (right) Ocean for (top) EXP0.1coup, (middle) EXP0.25coup, (bottom) EXP1coup; contour interval: 2 Sv.*

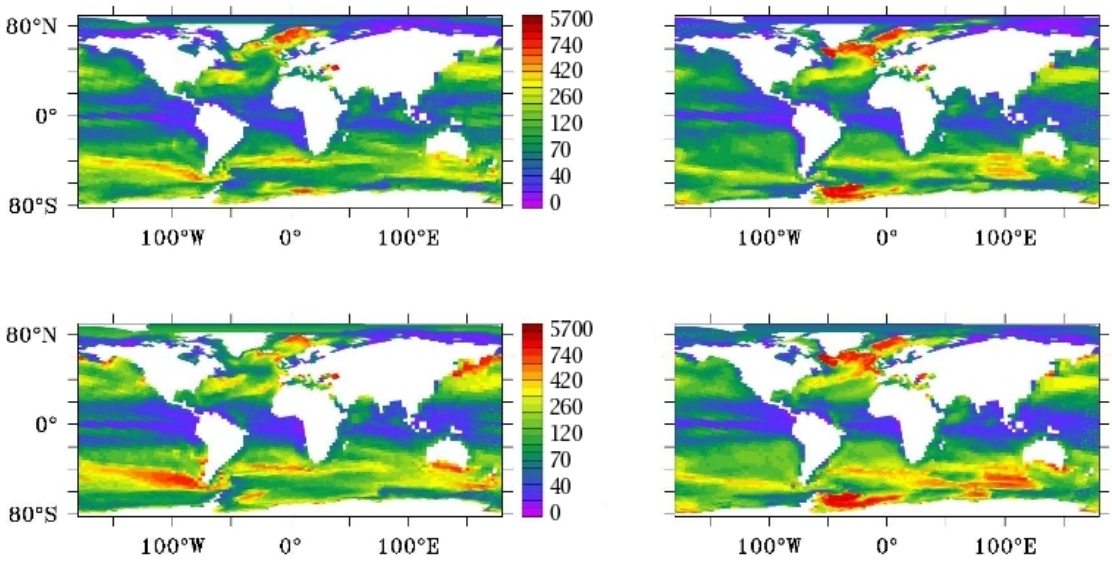

Figure 5.7: *Mixed layer depth in metres, left: coupled experiments, top left: EXP0.1coup, bottom left: EXP1coup; right: ocean-only experiments, top right: EXP0.1oce, bottom right: EXP1oce.*

in κ_b. In all the experiments only the background diffusivity κ_b is changed, but the other terms are free to adjust to the new ocean state and atmospheric forcing. To understand the opposite behavior of the strength of the MOC between the ocean only experiments and the coupled experiments, the difference in the total mixing and the different terms that compose it are looked at in the different ocean basins for an average of the last 10 years of the integration. From the overturning plots, we know that the major differences are seen between EXP1oce and EXP1coup, thus we compare the mixing fields with EXP1oce and EXP1coup, as EXP0.25oce and EXP0.25coup show very similar patterns to EXP0.1oce and EXP0.1coup. As explained in chapter 2, the total mixing $\kappa_v(total)$ is the sum of the mixing by convection $\kappa_v(convection)$ and the mixing from the PP-scheme $\kappa_v(PP - scheme)$.

5.2.1 Diffusivity - Ocean-only experiments

The zonal average total diffusivity $\kappa_v(total)$ of the model is shown for the global ocean (figure 5.8). The spatial distribution of the total diffusivity hardly changes between the experiments. High values of $\kappa_v(total)$ up to 150 cm^2/s are found at the

convection regions between 40-50°N to a depth of 2500 m, in the Southern Ocean throughout the water column, at the ocean surface and near bottom topography. In the ocean interior, $\kappa_v(total)$ equals the background diffusivity (0.1 cm^2/s for EXP0.1oce and 1 cm^2/s for EXP1oce). The difference between EXP0.1oce and EXP1oce in the open ocean is equal to the increase of the background diffusivity but also in the convection regions and at the surface of the ACC region. A decrease is observed in small regions at high northern latitudes and near bottom topography.

In the Atlantic ocean, high values of the $\kappa_v(total)$ more than 150 cm^2/s are found in regions of convection at high northern latitudes as well as at the surface, bottom topography and few locations at mid depths which correspond to high mixing near the mid Atlantic ridge (figure 5.9). Comparing EXP0.1oce and EXP1oce shows a strong increase by 35-55 cm^2/s in convection throughout the water column at 40-45°N, and north of the ACC region at the surface. A decrease by about 35 cm^2/s is observed in the Arctic region between 100 m and 1200 m.

In the Pacific ocean, high values of $\kappa_v(total)$ are found at the surface and bottom, around 80 cm^2/s (figure 5.10). As κ_b increases, $\kappa_v(total)$ increases at the surface north of the ACC and northern latitudes of the Pacific ocean by 35 cm^2/s and in the northern hemisphere by 55 cm^2/s and more. A decrease is observed deep near bottom topography.

The zonal mean diffusivity from the $\kappa_v(PP - scheme)$ accounts only for a small portion of the $\kappa_v(total)$ compared to $\kappa_v(convection)$ (figure 5.11 and 5.12). The spatial pattern of the $\kappa_v(PP - scheme)$ and $\kappa_v(convection)$ are very similar, with high values in the convection regions. The maximum values for the $\kappa_v(convection)$ is 125 cm^2/s whereas the maximum value for the $\kappa_v(PP - scheme)$ is 35 cm^2/s. As κ_b increases, both $\kappa_v(convection)$ and $\kappa_v(PP - scheme)$ show an increase in the convection region and at the surface north of the ACC and a reduction is observed in the high latitudes in the north. The changes in the $\kappa_v(PP - scheme)$ come from the combined effects of the shear and stability. The mixing induced by the wind does not change between the experiments as the windstress is prescribed at the surface.

5.2.2 Diffusivity - Coupled Experiments

The zonal mean total diffusivity $\kappa_v(total)$ in EXP0.1coup for the global ocean shows similar patterns to the ocean-only experiments, with high values in the convection

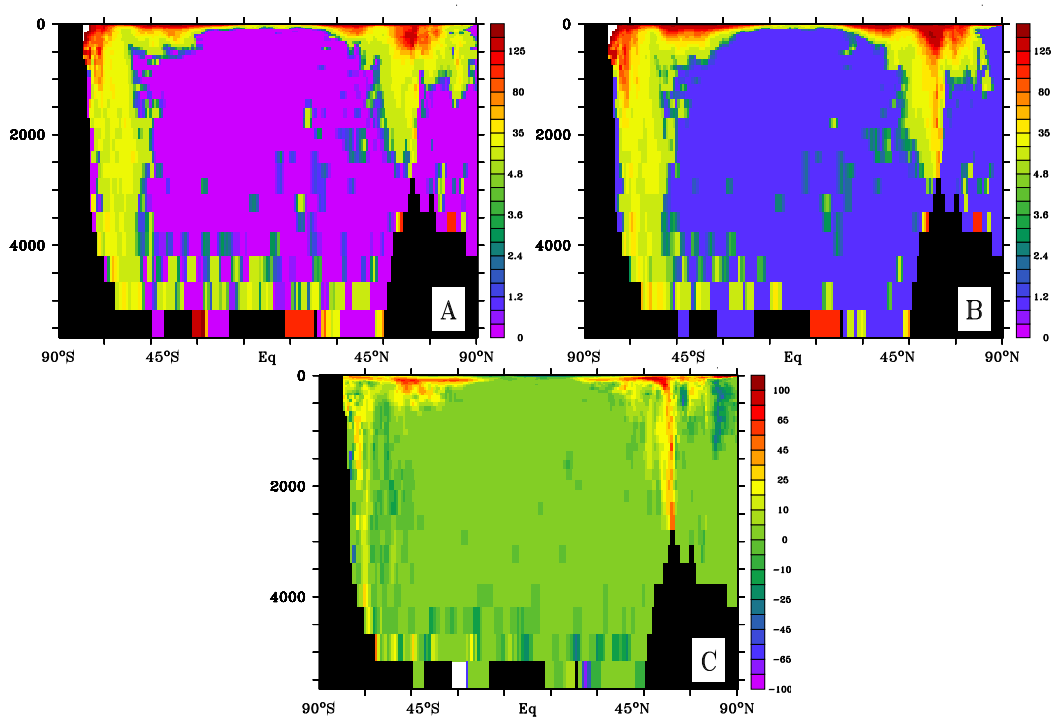

Figure 5.8: *In the ocean-only experiments, zonal mean total diffusivity (in cm^2/s) in the global ocean for EXP0.1oce (A) and EXP1oce (B), difference EXP1oce - EXP0.1oce (C).*

regions, at the surface and near bottom topography (figure 5.13). $\kappa_v(total)$ in the interior ocean is equal to κ_b. As κ_b increases, EXP1coup shows a very different pattern to EXP0.1coup in the convection regions in the northern and southern hemisphere, with little mixing below 1500 m. The difference plot between EXP0.1coup and EXP1coup highlights the strong reduction in $\kappa_v(total)$ in the convection region in the northern hemisphere and throughout the water column in the southern ocean, this behaviour is only found in the coupled experiments. An increase is observed in the north between 30-40°N between the surface and 1000 m and at the surface north of the ACC.

The strong reduction in $\kappa_v(total)$ in the northern hemisphere comes from the Atlantic ocean, where a reduction of the overturning and shallowing of the mixed layer depth is observed (figure 5.14). An increase in the $\kappa_v(total)$ is observed at the surface north of the ACC and at 30-40°N.

Most of the increase in $\kappa_v(total)$ in the northern hemisphere around 30-40°N comes from the Pacific where an overturning cell is observed in EXP1coup (figure 5.15).

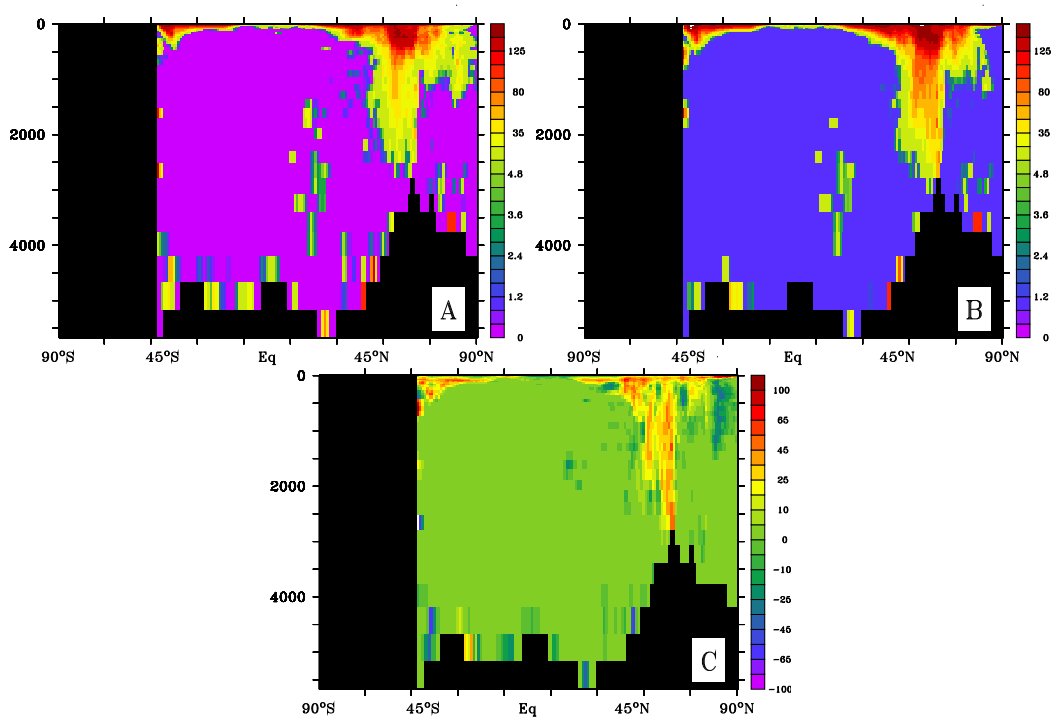

Figure 5.9: *In the ocean-only experiments, zonal mean total diffusivity (in cm^2/s) in the Atlantic ocean for EXP0.1oce (A) and EXP1oce (B), difference EXP1oce - EXP0.1oce (C).*

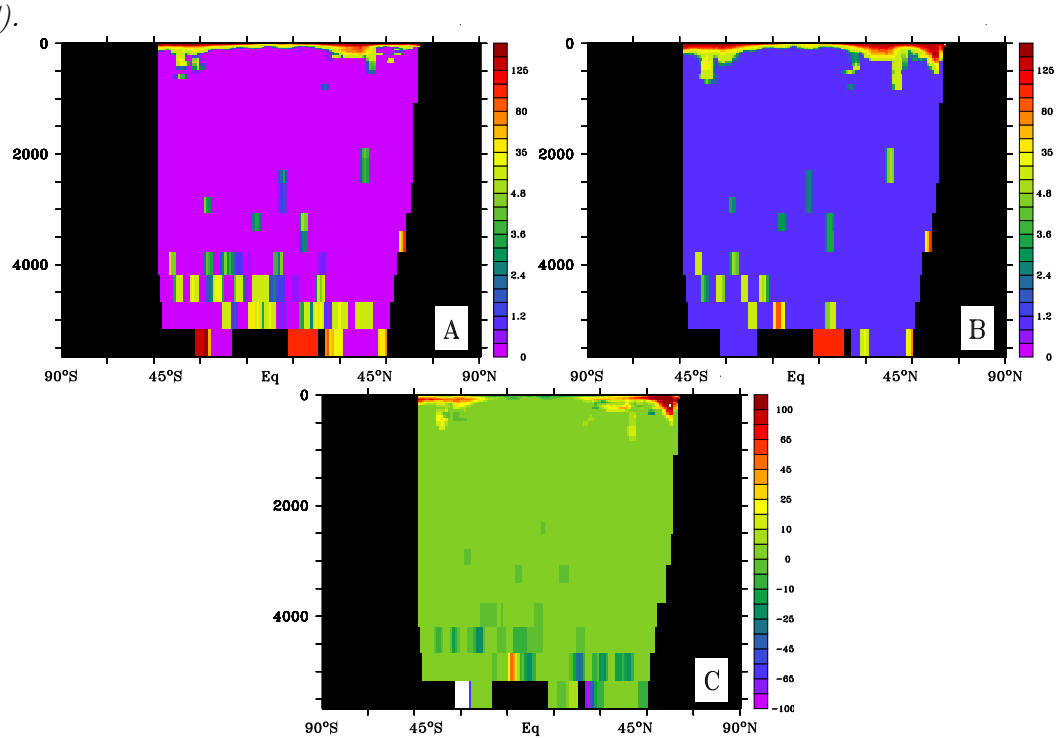

Figure 5.10: *In the ocean-only experiments, zonal mean total diffusivity (in cm^2/s) in the Pacific ocean for EXP0.1oce (A) and EXP1oce (B), difference EXP1oce - EXP0.1oce (C).*

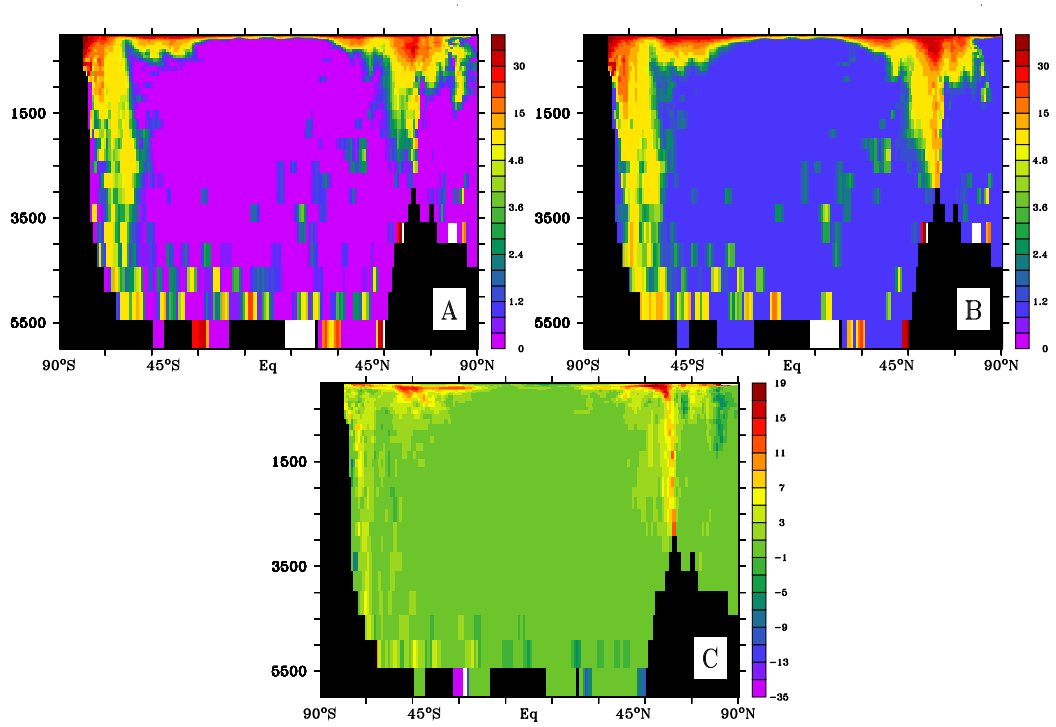

Figure 5.11: *In the ocean-only experiments, zonal mean diffusivity from the PP-scheme (in cm^2/s) in the global ocean for EXP0.1oce (A) and EXP1oce (B), difference EXP1oce - EXP0.1oce (C).*

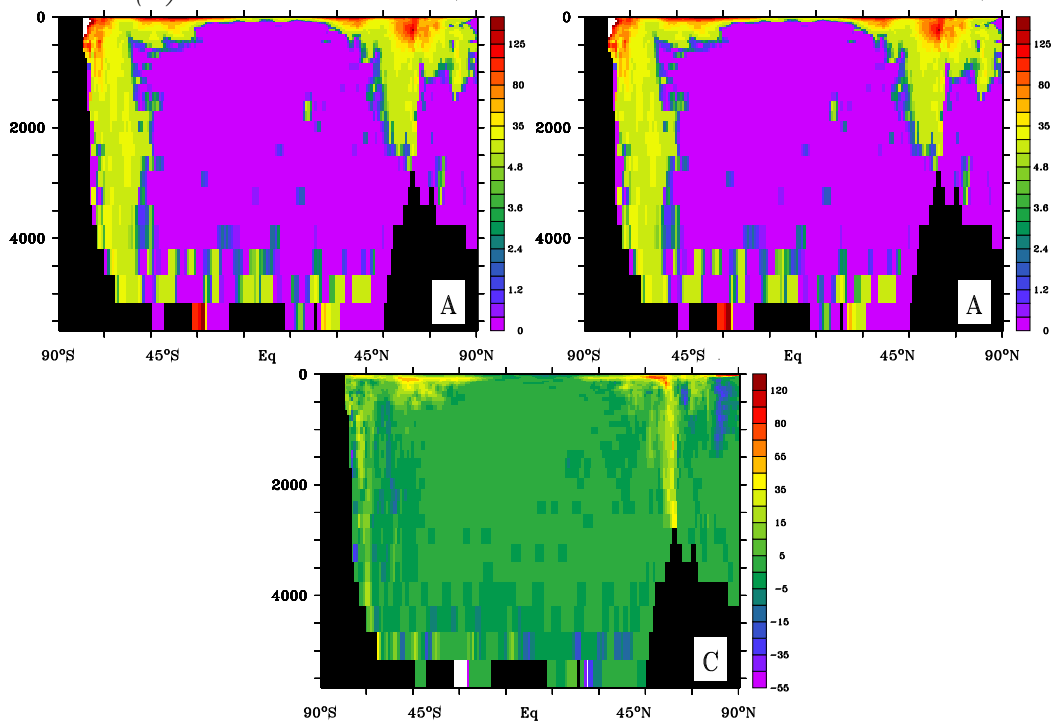

Figure 5.12: *In the ocean-only experiments, zonal mean diffusivity from convective mixing (in cm^2/s) in the global ocean for EXP0.1oce (A) and EXP1oce (B), difference EXP1oce - EXP0.1oce (C).*

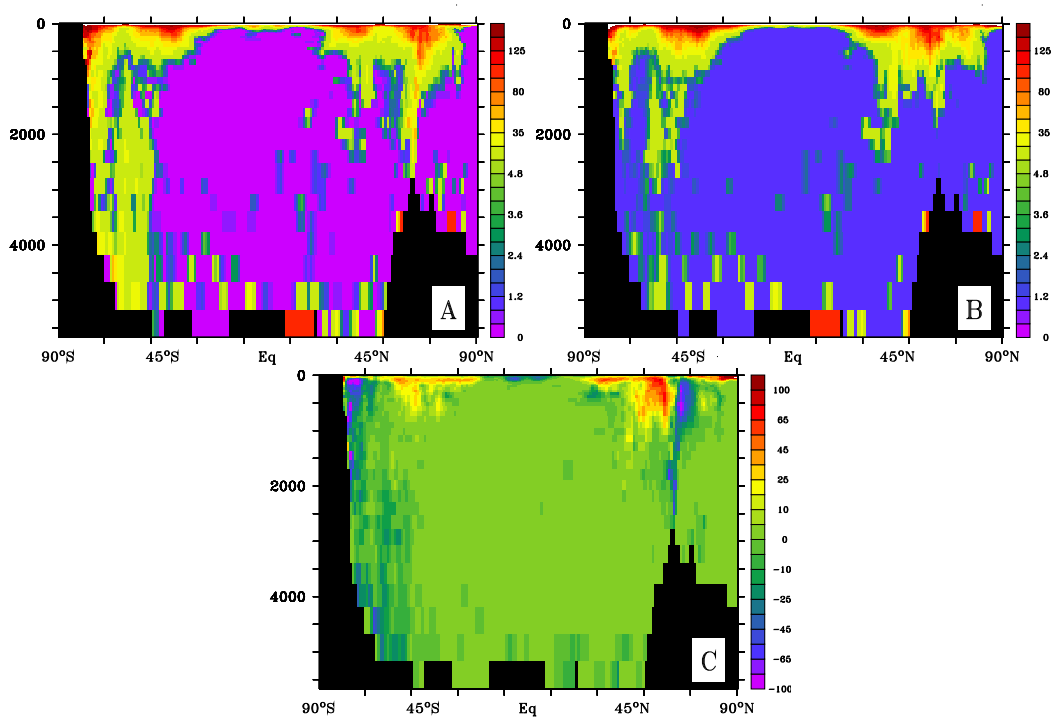

Figure 5.13: *In the coupled experiments, zonal mean total diffusivity (in cm^2/s) in the global ocean for EXP0.1coup (A) and EXP1coup (B), difference EXP1coup - EXP0.1coup (C).*

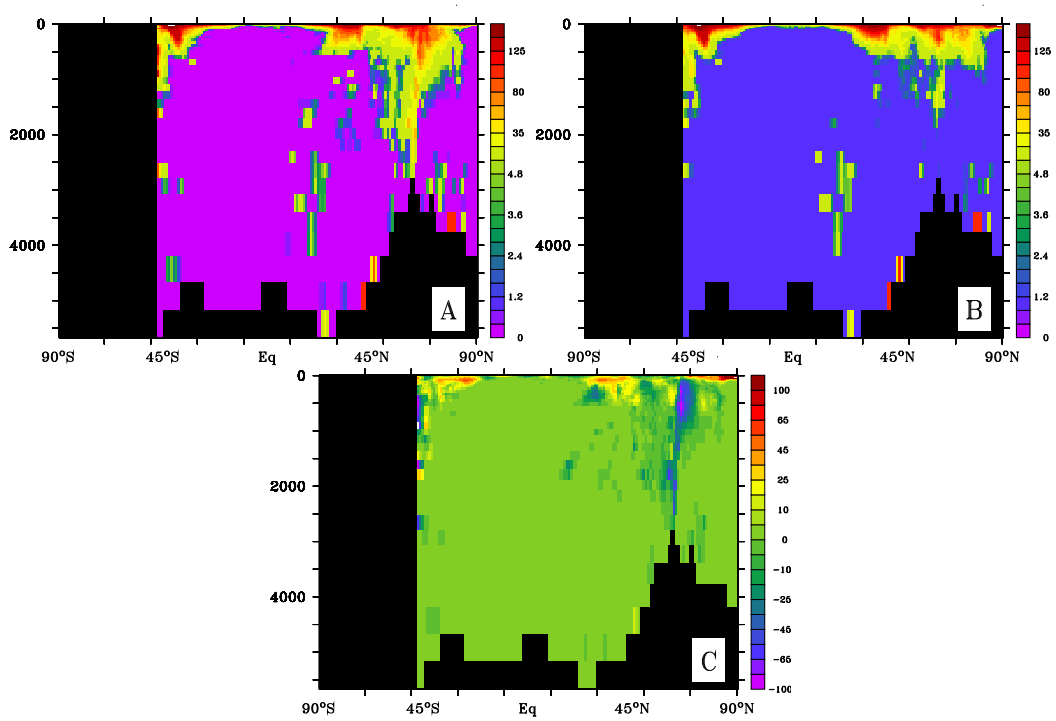

Figure 5.14: *In the coupled experiments, zonal mean total diffusivity (in cm^2/s) in the Atlantic ocean for EXP0.1coup (A) and EXP1coup (B), difference EXP1coup - EXP0.1coup (C).*

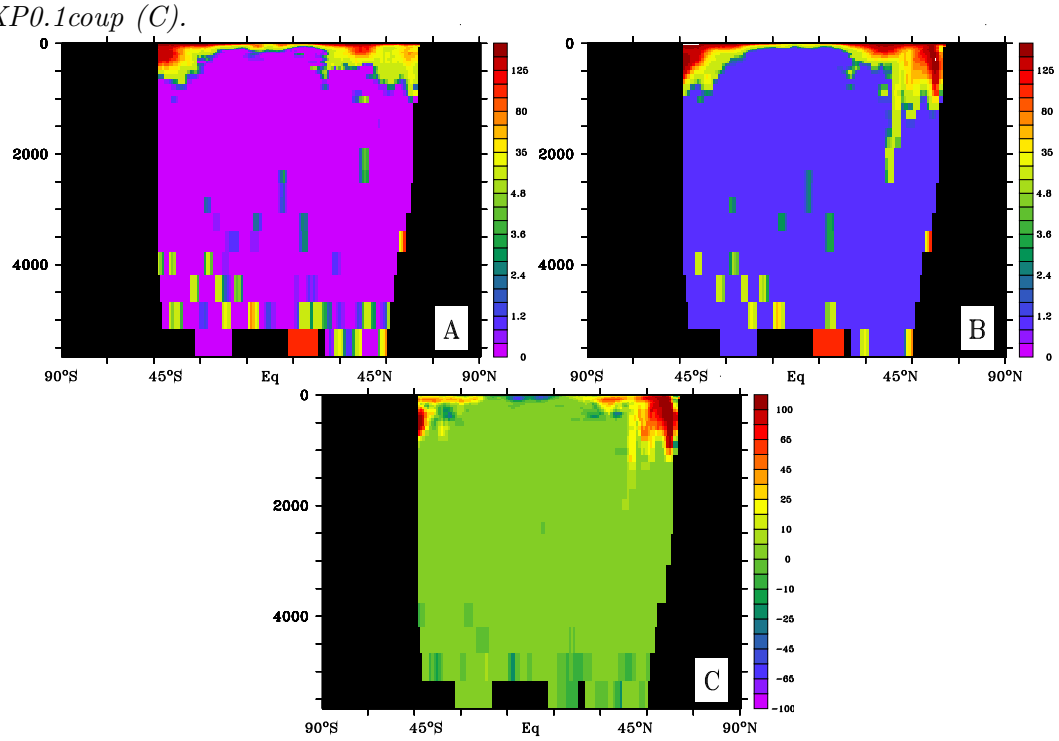

Figure 5.15: *In the coupled experiments, zonal mean total diffusivity (in cm^2/s) in the Pacific ocean for EXP0.1coup (A) and EXP1coup (B), difference EXP1coup - EXP0.1coup (C).*

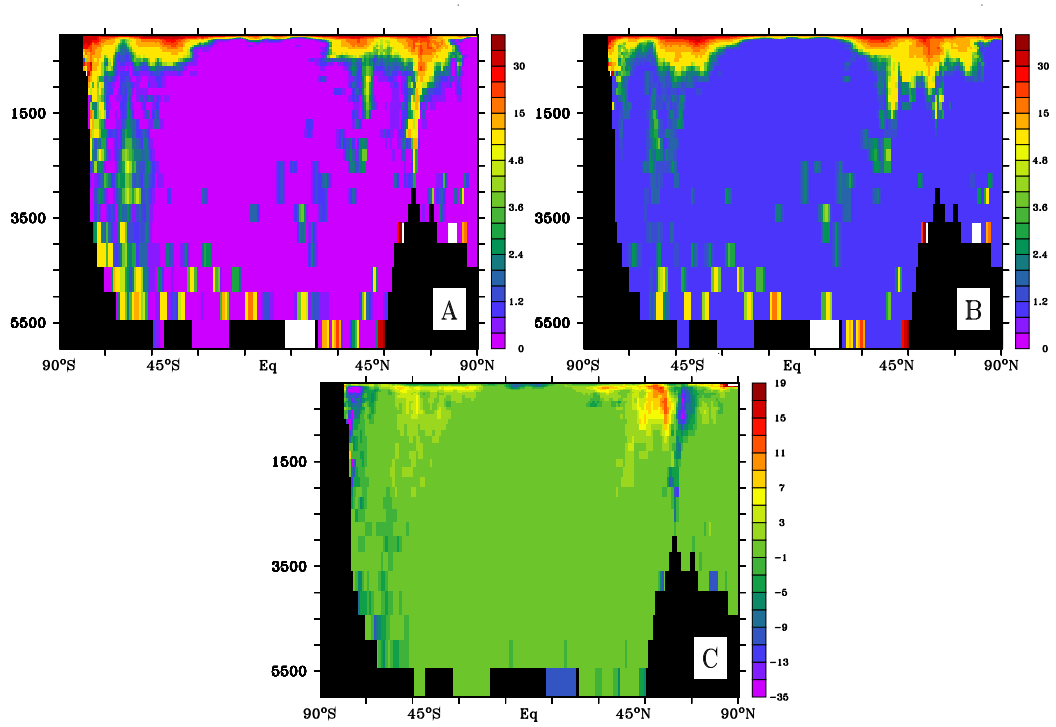

Figure 5.16: *In the coupled experiments, zonal mean diffusivity from the PP-scheme (in cm^2/s) in the global ocean for EXP0.1coup (A) and EXP1coup (B), difference EXP1coup - EXP0.1coup (C).*

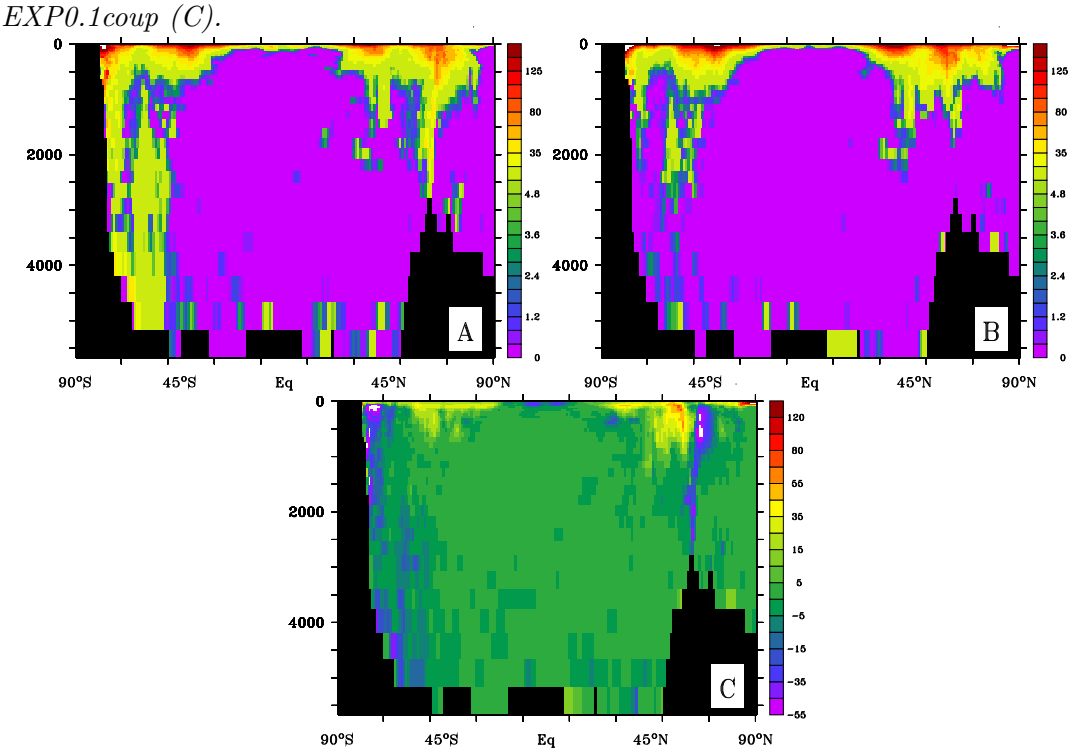

Figure 5.17: *In the coupled experiemts, zonal mean diffusivity from convective mixing (in cm^2/s) in the global ocean for EXP0.1coup (A) and EXP1coup (B), difference EXP1coup - EXP0.1coup (C).*

The spatial distribution of the mixing due to the PP-scheme and the convective mixing are also very similar when κ_b is increased, and most the mixing comes from the convective mixing. We find when we further decompose each component from the PP-scheme that the Richardson number contribution decreases in the Arctic region and in the South Pacific and increases in the ACC and south Atlantic. These changes in the Richardson number can be related to a decrease in the stability components in the Arctic region and a decrease in the shear in the upwelling region in the Pacific, Indian Ocean and North Atlantic. The mixing induced by the windstress at the surface decreases in the ACC and in the north Atlantic.

We find that the $\kappa_v(convective)$ dominates over the $\kappa_v(PP - scheme)$. This suggests that the cause of the difference in behavior of the MOC between the coupled and ocean experiments is induce by the changes in the convection patterns due to changes in the water masses. Both terms ($\kappa_v(convective)$ and $\kappa_v(PP-scheme)$) are both dependent on the stability of the water column, which explains the similarity in the location of the changes in $\kappa_v(convection)$ and $\kappa_v(PP - scheme)$.

5.3 Changes in the Water Masses

In the section 5.2, $\kappa_v(total)$ shows opposite response between the coupled and ocean only experiments in the North Atlantic, Southern Ocean and Pacific as κ_b increases. We analyse the water masses properties profiles in different ocean regions by looking at the density, temperature, salinity and stability frequency for all experiments undertaken (figure 5.18). The larger the stability frequency, the more stable is the water column. Instability leads to an increase in the mixing by convection.

5.3.1 Nordic Seas and Arctic Region

In the Nordic Seas (named GIN on the map, figure 5.18) and Arctic regions, the profiles show very similar changes in the water properties as κ_b increases (figures 5.19 and 5.20). The changes in the coupled experiments are much larger than in the ocean only experiments. In the Nordic Seas, the density is reduced throughout the water column, from 27.9 kg/m^3 at 1000 m in EXP0.1coup to 27.2 kg/m^3 in EXP1coup. The stability and salinity profiles do not change in the ocean-only experiments. In

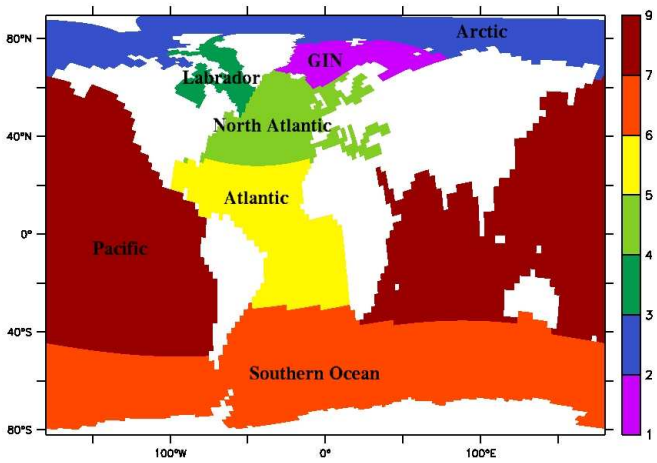

Figure 5.18: *Different regions of the ocean where the water properties profiles are looked at.*

the coupled experiments, the stability profiles decreases at the surface and increases between 500 m and 2000 m as κ_b increases, which explains the reduction in the mixed layer depth in these regions. The salinity profiles decrease as κ_b increases in the coupled experiments, up to 0.9 PSU at 1000 m deep. The temperature increases by 0.5°C between 500 m to the bottom in the ocean only experiments. In the coupled experiments, the temperature decreases by 0.5°C between the surface and 2500 m.

5.3.2 Labrador Region

In the Labrador region (figure 5.21), the density profiles show a stronger reduction in the coupled experiments than in the ocean only experiments. The density reduces from 27.6 kg/m^3 in EXP0.1coup to 26.9 kg/m^3 in EXP1coup between 1000 and 2500 m depth. The stability reduces as κ_b increases in the first 300 m in both sets of experiments. In the coupled experiments, the stability frequency increases between 1500 m and 3000 m as κ_b increases. The temperature shows an increase of 1.5°C between 500 m and 2500 m in the ocean-only experiments. In the coupled experiments the temperature is found to decrease by 0.5°C between 100 m and 700 m and to increase by 0.5°C between 700 m and 2000 m and then again to decrease

between 2000 m to 3000 m as κ_b increases. The salinity profiles in the North Atlantic show a large reduction as κ_b increases in the coupled experiments, by 0.7 PSU at 1000 m depth, compared to a weak reduction in the ocean-only experiments.

5.3.3 North Atlantic Region

In the north Atlantic region, the density profiles decrease throughout the whole water column as the Arctic and Nordic Seas as κ_b increases (figure 5.22). The stability frequency profiles increases between 1000 m and 2000 m and decreases at the surface as κ_b increases. This increase is more pronounced in the coupled experiments. The temperature profiles show a warming by 1°C in the ocean only experiments through the whole water column, and in the coupled experiments a warming of 1.5°C is observed below 3000 m. The salinity profiles show large changes of up to 0.6 PSU between 500 m and 3500 m in the coupled experiments. The ocean only experiments show a small increase of 0.1 PSU between 1000 m and 3500 m as κ_b increases.

5.3.4 Atlantic Region

The density profiles show a decrease in the ocean only and coupled experiments, the density decreases as κ_b increases; the changes are more pronounced in the coupled experiments (figure 5.23). The stability profiles show a small increase between 1500 m and 3000 m in the coupled and ocean-only experiments. At the surface, the stability reduces, which explains the deeper and stronger shallow equatorial cells, as κ_b increases. The temperature, increases as κ_b increases, by about 1°C in the ocean only experiments and 2°C in the coupled experiments. The salinity profiles do not change so much in the ocean only experiments, but the coupled experiments show an increase in the first 1000 m and a decrease down to 3500 m. The salinity shows the most differences between the experiments. Many of the changes at depth are observed in the convection regions such as the Arctic and Nordic Seas.

5.3.5 Southern Ocean Region

In the Southern Ocean region, the density profiles show a much weaker stratification than the other regions (figure 5.24). The density shows a decrease of 0.35 between

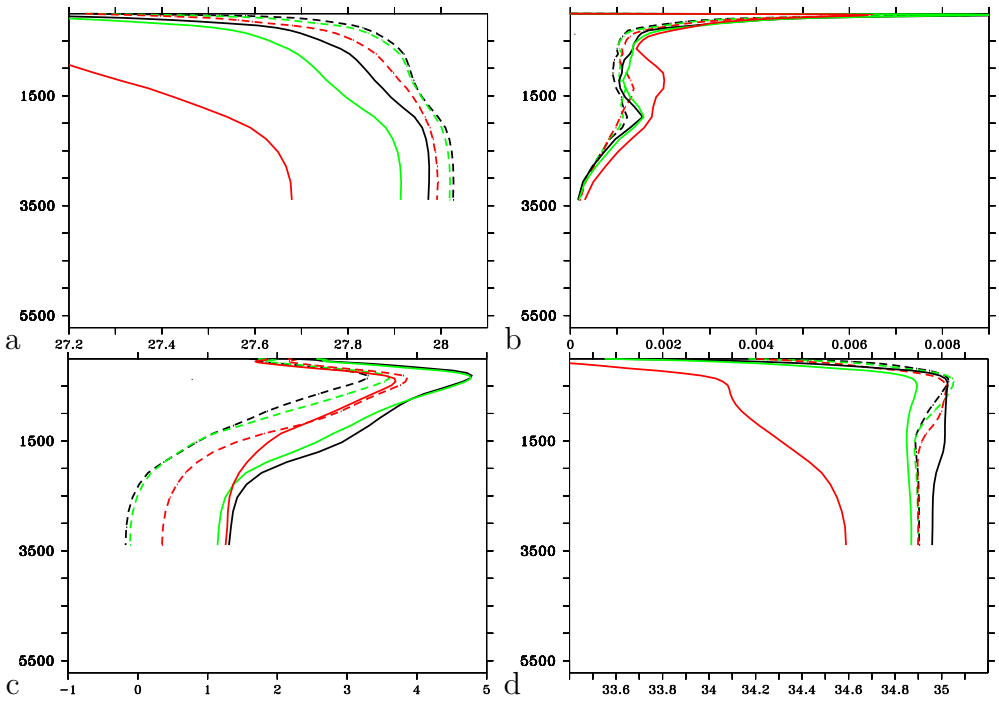

Figure 5.19: *Vertical profile in the GIN region of the density in kg/m^3 (a), stability frequency in rad.s^{-1} (b), temperature in °C (c) and salinity in PSU (d) for EXP0.1 (black), EXP0.25 (green) and EXP1 (red), the coupled experiments are represented by the solid lines and the ocean only experiments by the dashed line.*

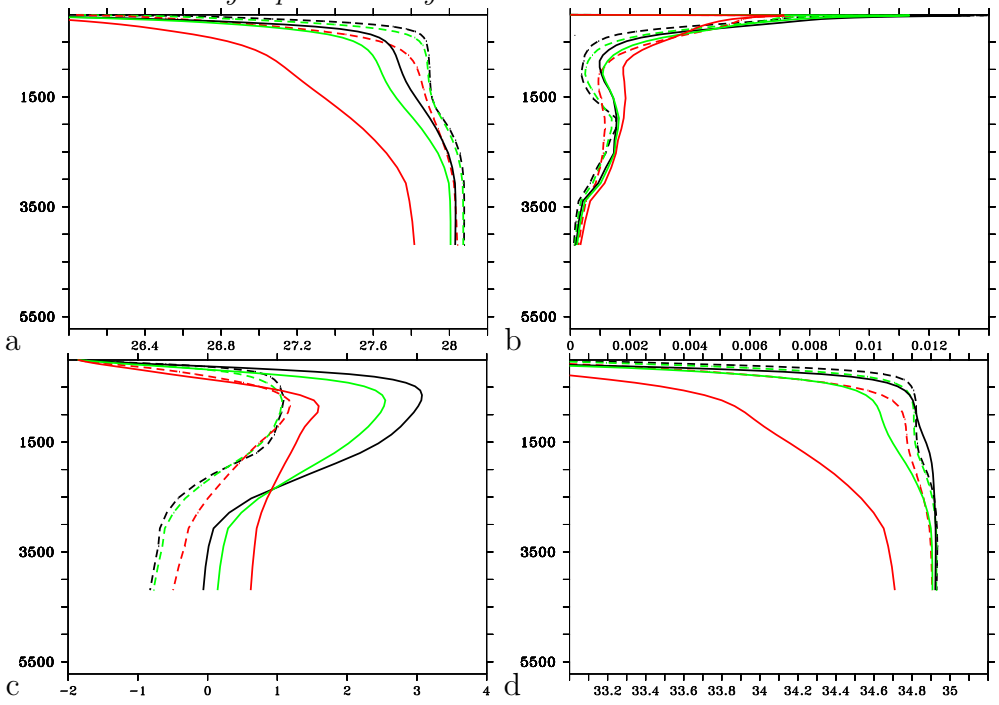

Figure 5.20: *Vertical profile in the Arctic region of the density in kg/m^3 (a), stability frequency in rad.s^{-1} (b), temperature in °C (c) and salinity in PSU (d) for EXP0.1 (black), EXP0.25 (green) and EXP1 (red), the coupled experiments are represented by the solid lines and the ocean only experiments by the dashed line.*

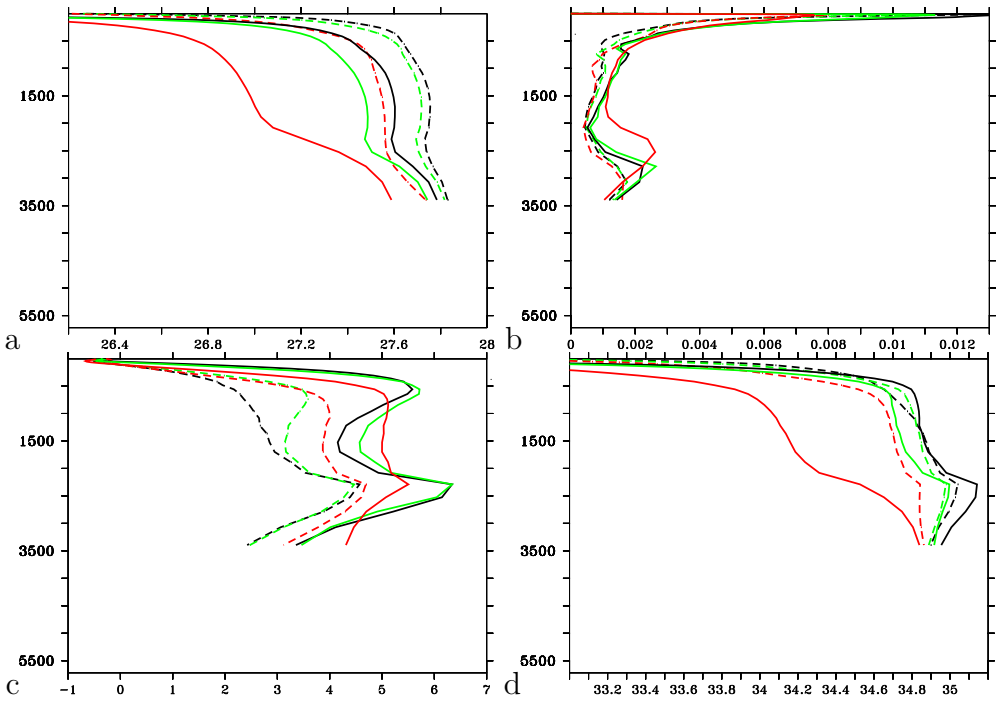

Figure 5.21: *Vertical profile in the Labrador region of the density in kg/m^3 (a), stability frequency in $rad.s^{-1}$ (b), temperature in $^\circ C$ (c) and salinity in PSU (d) for EXP0.1 (black), EXP0.25 (green) and EXP1 (red), the coupled experiments are represented by the solid lines and the ocean only experiments by the dashed line.*

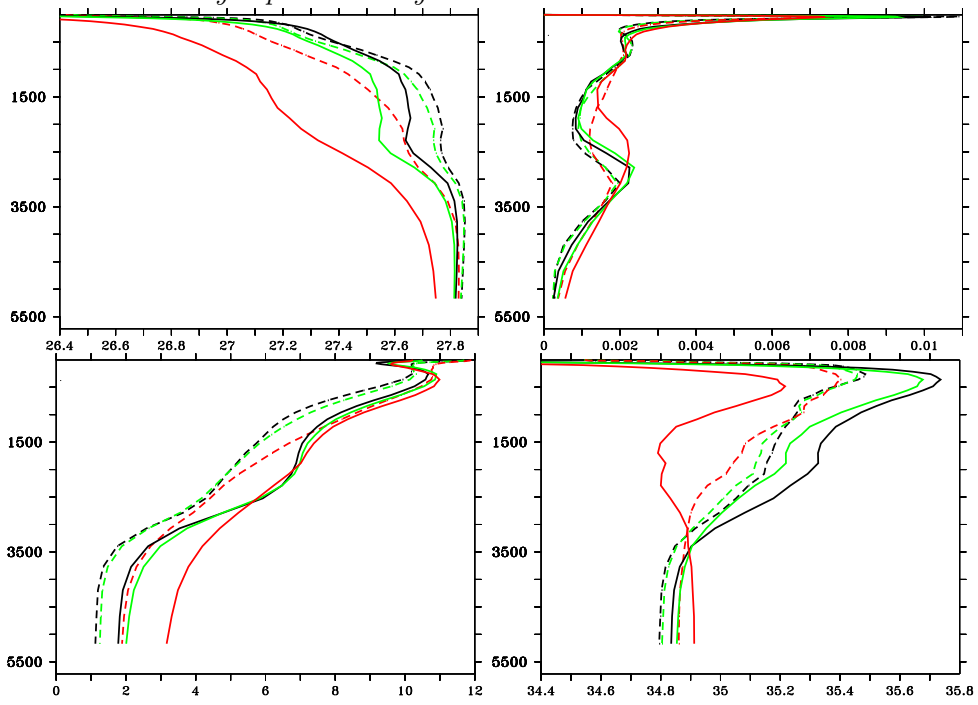

Figure 5.22: *Vertical profile in the North Atlantic region of the density in kg/m^3 (a), stability frequency in $rad.s^{-1}$ (b), temperature in $^\circ C$ (c) and salinity in PSU (d) for EXP0.1 (black), EXP0.25 (green) and EXP1 (red), the coupled experiments are represented by the solid lines and the ocean only experiments by the dashed line.*

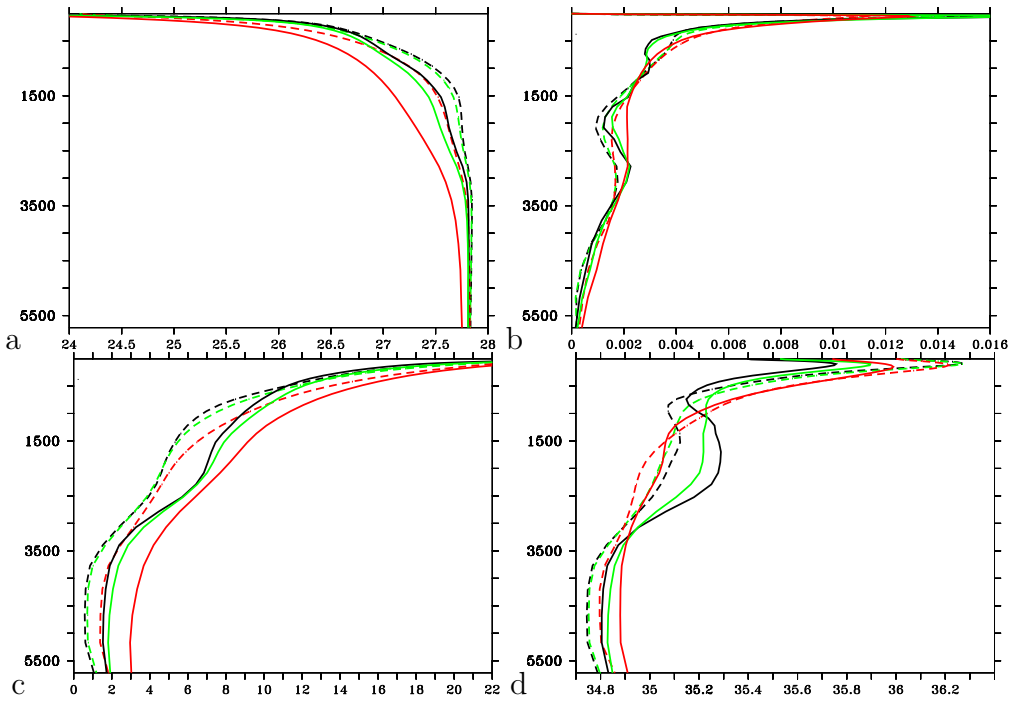

Figure 5.23: *Vertical profile in the Atlantic region of the density in kg/m^3 (a), stability frequency in rad.s^{-1} (b), temperature in °C (c) and salinity in PSU (d) for EXP0.1 (black), EXP0.25 (green) and EXP1 (red), the coupled experiments are represented by the solid lines and the ocean only experiments by the dashed line.*

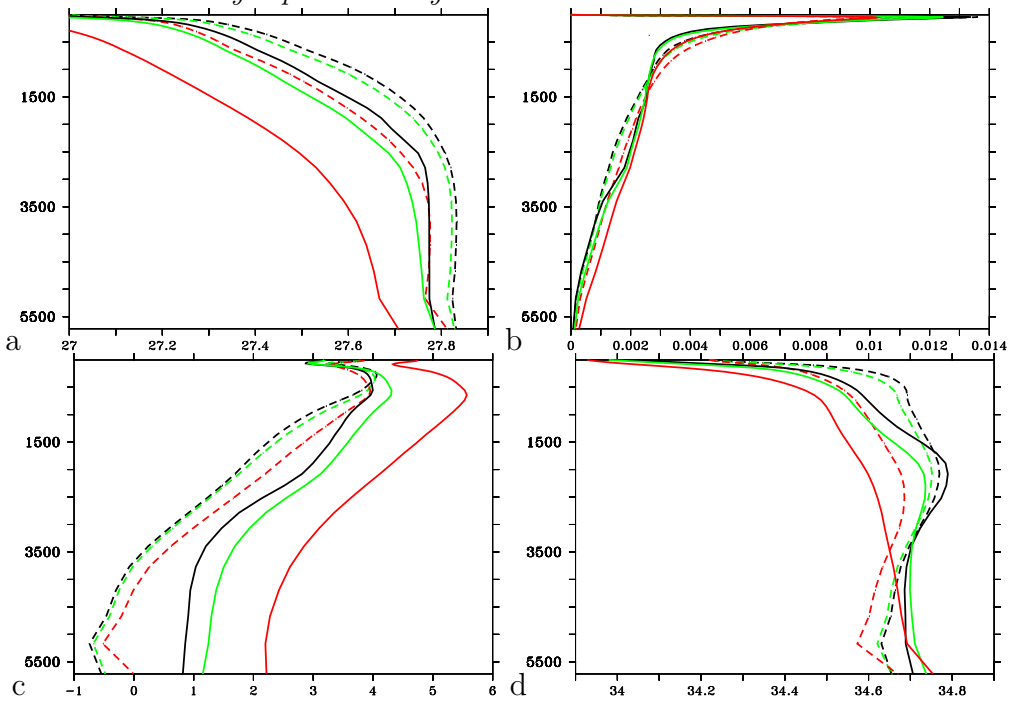

Figure 5.24: *Vertical profile in the southern ocean region of the density in kg/m^3 (a), stability frequency in rad.s^{-1} (b), temperature in °C (c) and salinity in PSU (d) for EXP0.1 (black), EXP0.25 (green) and EXP1 (red), the coupled experiments are represented by the solid lines and the ocean only experiments by the dashed line.*

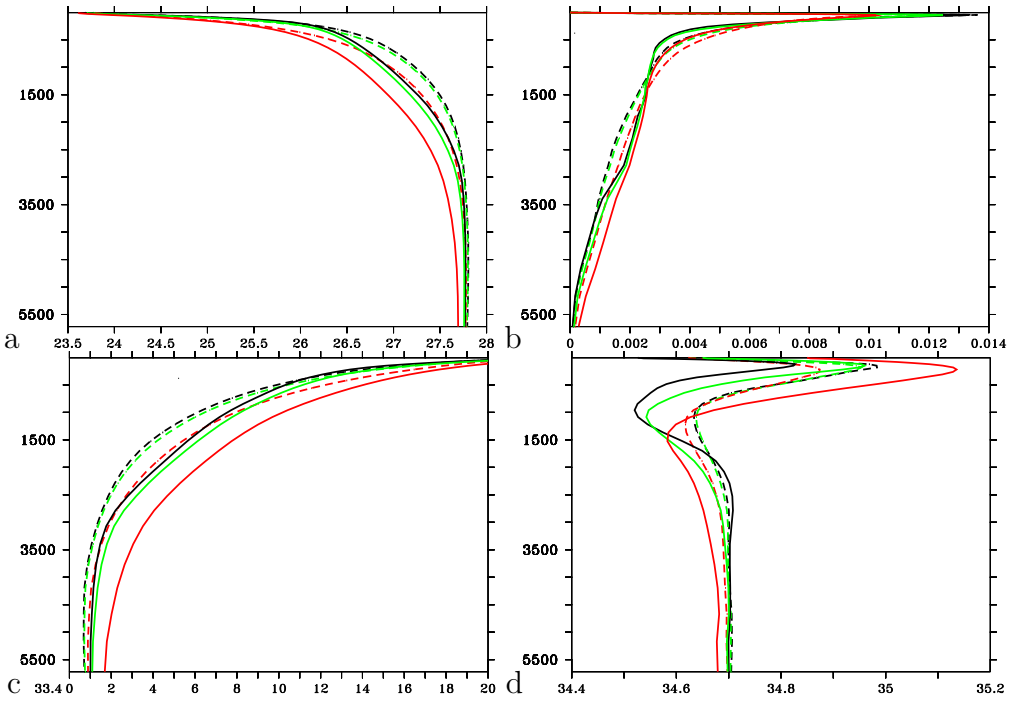

Figure 5.25: *Vertical profile in the Pacific region of the density in kg/m^3 (a), stability frequency in rad.s^{-1} (b), temperature in °C (c) and salinity in PSU (d) for EXP0.1 (black), EXP0.25 (green) and EXP1 (red), the coupled experiments are represented by the solid lines and the ocean only experiments by the dashed line.*

EXP0.1coup and EXP1coup, and of 0.1 in the ocean-only experiments. The stability shows very little changes throughout the water column. The temperature increases by 1.5°C throughout the water column between EXP0.1coup and EXP1coup, and by 0.5°C between 500 m to the bottom in the ocean-only experiments. The salinity decreases by 0.1 PSU between EXP0.1 and EXP1 in both coupled and ocean only experiments.

5.3.6 Pacific Region

In the Pacific region, the strongest changes are observed in the salinity profiles, with a strong reduction by nearly 0.4 PSU in the northern latitudes in the Atlantic in the coupled experiments (figure 5.25). The temperature is also found to reduce in the Atlantic region in the coupled experiments. These changes explain the increase in the stability around 1000 m in these regions, leading to reduction of the convection depth and therefore the MOC.

The strongest changes are observed in the coupled experiments. The Southern Ocean is found to warm significantly over the entire water column, this warming is found in the deepest water in the different regions.

5.4 Heat and Freshwater Transport

The coupled experiments highlights strong difference in the water masses between the experiments. These changes can be caused by changes in the ocean properties or atmospheric one for the coupled experiments. We first looked at the tracer transports in the ocean in order to explain the changes in water masses then the climate response in the coupled experiments.

5.4.1 Heat Transport

We look at the heat transport to explain the changes in the temperature profiles. The heat transport at 30°N in the Atlantic shows a strong correlation with the maximum MOC strength in the North Atlantic in both ocean only and coupled experiments

(figure 5.26). The timeseries of the heat transport at 30°N in the Atlantic in the ocean only experiments increase as κ_b increases. In EXP0.1oce, the time mean heat transport at 30°N in the Atlantic is 0.67 PW northwards, in EXP0.25oce 0.73 PW and in EXP1oce 1 PW at the end of the 460 years. In the coupled experiments, the heat transport shows a similar behaviour to the maximum MOC at 30°N. In the coupled experiments, in EXP0.1coup, the heat transport is 0.6 PW northwards. In EXP0.25coup, the heat transport first decreases then it recovers to its original value and stabilises at 0.55 PW at the end of the 460 years. In EXP1coup, the heat transport shows a sharp increase in the first 20 years before decreasing and stabilising around 0.45 PW at the end of the 460 years.

The heat transport in the global, Atlantic and Pacific ocean correlates with the changes in the overturning circulation. The global heat transport increases its transport northward in the northern hemisphere and southward in the southern hemisphere by about 0.2 PW as κ_b increases. No changes is observed between 10°S and 10°N. The Atlantic heat transport shows a decrease of the northward heat transport in the northern hemisphere. The southern hemisphere shows a small southward heat transport in EXP1coup. The Pacific Ocean shows as an increase by about 0.2 PW of its northward heat transport in the northern hemisphere and the same amount southward in the southern hemisphere.

The increase in the heat transport in the ocean only experiments influences the temperature profiles at high latitudes. In fact, in the Nordic, labrador seas and North Atlantic ocean are found to increase as κ_v increases. In the coupled experiments, the opposite behavior is found, where the reduction in the temperatures in found in the high latitudes between 1000-1500 m deep. The colder temperatures in the convection regions in the coupled experiments cannot explain the reduction in the MOC.

5.4.2 Freshwater Transport

The salinity profiles in the coupled experiments show the strongest changes whereas only minor changes are obserserved in the ocean only experiments. We are looking at the freshwater transport to explain the changes in the freshening at high latitudes. In the global ocean, the freshwater transport increases by 0.01 Sv between

a

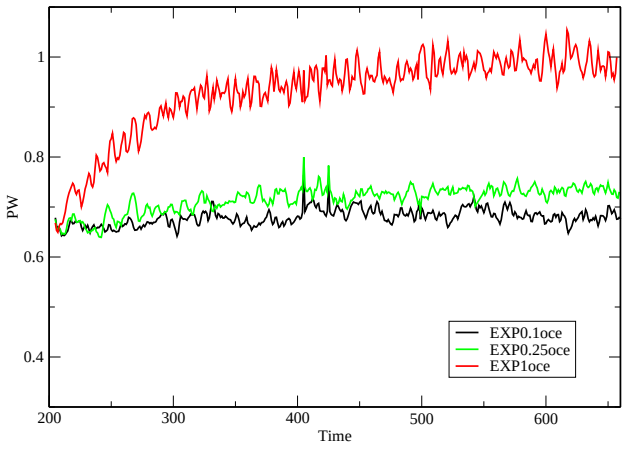

b

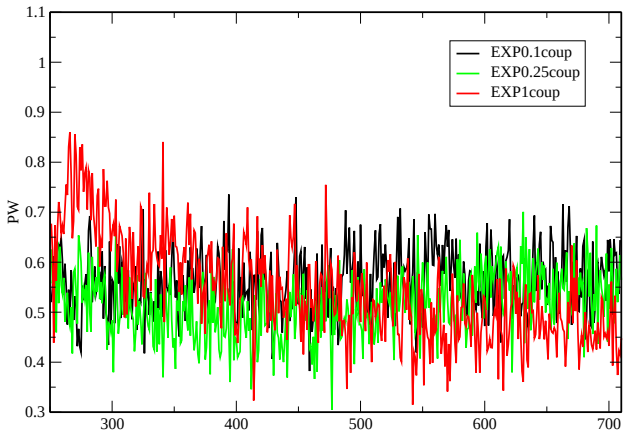

Figure 5.26: *Timeseries of the heat transport in the north Atlantic in PW (a) ocean-only experiments (b) coupled experiments for EXP0.1 (black), EXP0.25 (green) and EXP1 (red).*

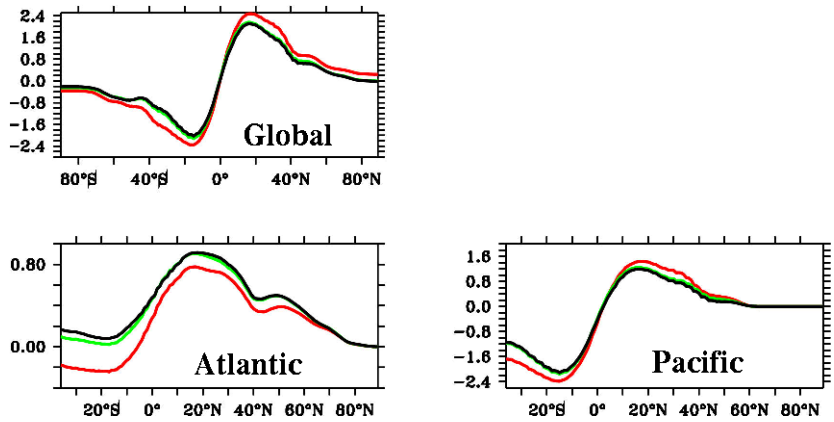

Figure 5.27: *Heat transport in PW in coupled experiments (top) in the global ocean, (bottom left) in the Atlantic, (bottom right) in the Pacific for EXP0.1coup (black), EXP0.25coup (green) and EXP1coup (red) .*

20°S and 20°N between EXP0.1 and EXP1 (figure 5.28). In the Atlantic, the northward freshwater transport increases by 0.0035 Sv between the equator and 20°S as κ_b increases, and decreases between the equator and 10°N. The freshwater transport increases southwards by 0.01 Sv between 10°N and 20°N as κ_b increases. In the Pacific, the northward freshwater transport increases by 0.01 Sv between the equator and 20°S and decreases between the equator and 10°N as κ_b increases. The southward freshwater transport increases by 0.01 Sv between 10°N and 20°N. No changes in the freshwater transport are observed at latitudes higher than 20°S and 20°N. The changes in the freshwater profiles cannot be explained by the changes in the freshwater transport in the coupled experiments.

5.5 Climate Response

The experiments undertaken highlight the importance of the coupling, by the opposite response of the NADW in the Atlantic between the ocean-only and the coupled experiments to increasing κ_b. The changes in the ocean heat transport can explain the changes in the temperature in the ocean only and coupled experiments. But in the coupled experiments, the strong changes in the salinities at high latitudes cannot be explain by the changes in the ocean freshwater transport in the Atlantic. To explain these changes, we look at atmospheric fluxes in the different regions.

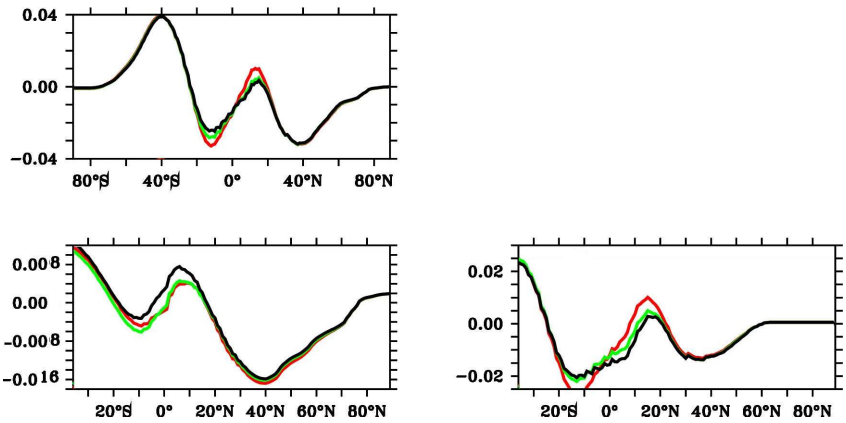

Figure 5.28: *Freshwater transport in Sv in coupled experiments (top) in the global ocean, (bottom left) in the Atlantic, (bottom right) in the Pacific for EXP0.1coup (black), EXP0.25coup (green) and EXP1coup (red).*

5.5.1 Atmospheric Fluxes

The heat and water fluxes from the atmosphere to the ocean can ajust to the new ocean state and have a feedback to the ocean in the coupled experiments (figure 5.29). In the ocean only experiments, the fluxes are calculated from the ocean state and a prescribed atmosphere using the bulk formulas.

In EXP0.1coup of the coupled experiments, the ocean takes up between 100 to 150 W/m^2 in the equatorial and upwelling regions and in the northern Atlantic regions. The regions of strong heat loss are in the Gulf Stream and Kuriosho regions with heat lost of 200-300 W/m^2. The north Atlantic, Arctic, Nordic Seas and Labrador regions lose between 60 and 180 W/m^2. As κ_b increases, the ocean takes up more heat in the equatorial regions, but less in the upwelling and southern regions. Also, more heat is lost in the northern latitudes in the Atlantic and Pacific in the coupled experiments. The strongest changes are observed in the Labrador and Nordic Seas (table 5.1). In the ocean only experiments, the changes as κ_b increases are much weaker and the Arctic, Nordic Seas and North Atlantic lose less heat, in contrast to the coupled experiments. These differences at all northern latitudes can explain the difference in the temperature profiles, which are found to have a colder surface water in the coupled experiments as κ_b increases. In the Pacific and Atlantic regions, the ocean gains more heat and loses more in the Southern Ocean as κ_b increases in all experiments. At high latitudes, the ocean heat lost increases as κ_v increases which suggests that the ocean is melting the sea-icea from below.

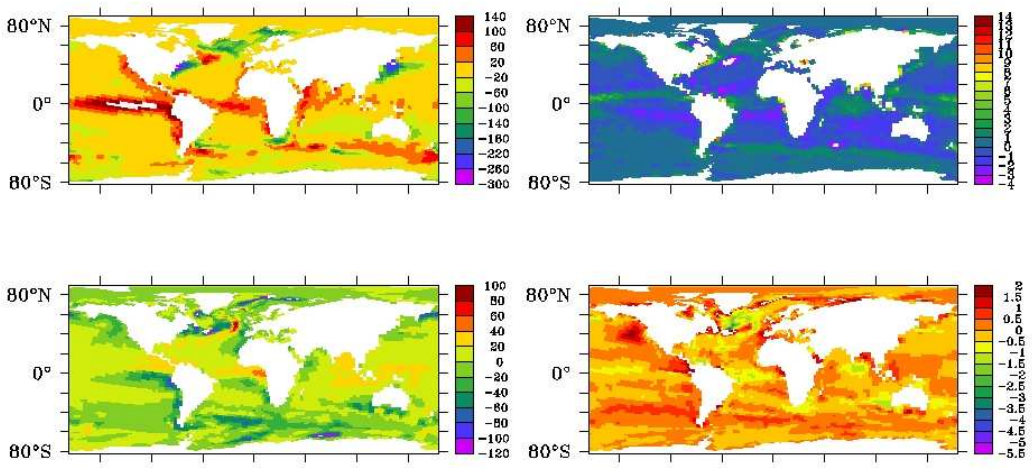

Figure 5.29: *Heat flux in W/m^2 (top left) and freshwater flux in m/year (top right) for EXP0.1coup and the difference between EXP1coup and EXP0.1coup for the heat flux (bottom left) and freshwater flux (bottom right) in the coupled experiments.*

In EXP0.1coup, the waterflux has net precipitation in the equatorial and high northern latitudes in the Pacific and Atlantic Oceans and Southern Ocean and a net evaporation is observed in the tropical regions, in the Atlantic and Pacific regions (figure 5.29). As κ_b increases, the evaporation is reduced in the middle of the Nordic Seas and more precipitation is observed in the North Atlantic and east equatorial Pacific. The waterflux in the Arctic, labrador and North Atlantic is found to decrease in the first 30-40 years then increases and exceeds the water flux in the control run. Table 5.2 shows the net precipitation and evaporation in the different regions for the last 10 years of the experiments. In the coupled experiments, the average water flux in the Arctic, Nordic Seas and Labrador shows an increase in the precipitation. The strongest changes are in the GIN and Labrador regions in the coupled experiments. The increase in precipitation is between 50 and 100% at high latitudes. This increases has the same temporal variations that the MOC. At the beginning of the sensitivity experiments, the precipitation reduces at high latitudes when the MOC is found in EXP1 to increase. Then the precipitation increases in EXP1 which is followed by a decrease of the MOC. The significant freshwater input in the high latitudes can sustain in reduction in the MOC in the north Atlantic. The Pacific shows an increases in evaporation in the coupled experiments but an increase in precipitation in the ocean-only experiments. This could explain the overturning cell in the northern Pacific in the coupled experiments due to the transport of saltier

	Ocean			*Coupled*		
	EXP0.1	EXP0.25	EXP1	EXP0.1	EXP0.25	EXP1
Total	-8.4	-8.2	-6.6	-9.1	-9.6	-12.5
Arctic	-7.0	-6.5	-6.3	-6.6	-6.9	-7.4
GIN	-58.9	-56.8	-46.2	-43.4	-49	-63.2
Labrador	-8	-9.6	-9.4	-16.2	-16.7	-25.6
North Atl	-30.4	-29	-22.9	-42.9	-43.8	-50.4
Atlantic	13.9	14.2	18.1	11.9	13	19.5
Pacific	2.9	2.4	3.5	4.4	4.7	6.8
South Ocean	-7.8	-7.7	-11.2	-5.9	-6.6	-15.8

Table 5.1: *Heat flux for the different values of κ_b for the ocean only and coupled experiments in W/m^2.*

	Ocean			*Coupled*		
	EXP0.1	EXP0.25	EXP1	EXP0.1	EXP0.25	EXP1
Total	0.15	0.16	0.17	0.12	0.12	0.16
Arctic	0.52	0.53	0.54	0.49	0.54	0.65
GIN	0.38	0.45	0.47	0.28	0.38	0.57
Labrador	0.78	0.78	0.82	0.44	0.47	0.74
North Atl	0.36	0.37	0.42	0.31	0.26	0.19
Atlantic	-0.56	-0.53	-0.56	-0.36	-0.39	-0.49
Pacific	-0.09	-0.1	-0.1	-0.09	-0.08	-0.06
South Ocean	0.39	0.4	0.42	0.28	0.29	0.37

Table 5.2: *Water flux for the different values of κ_b for the ocean only and coupled experiments in m/year.*

water and more evaporation at high latitudes.

5.5.2 Surface air temperature

The surface air temperature is found to have increased at high latitudes with the strongest changes in the southern Ocean by 8 °C and in the Arctic region by 2°C. This has effect on the heat flux as shown in the previous section but also on the sea-ice extend and snow cover. The sea ice cover is found to reduce as κ_v increases. In the coupled experiments, the sea ice in EXP0.1coup has a thickness of about 4 metres in the Arctic region (figure 5.31). The Labrador and Nordic Seas show ice cover between 0.4 m and 1.5 m. As κ_b increases, the sea ice thickness reduces in all regions with sea-ice cover. The sea ice around the Antarctic Peninsula has

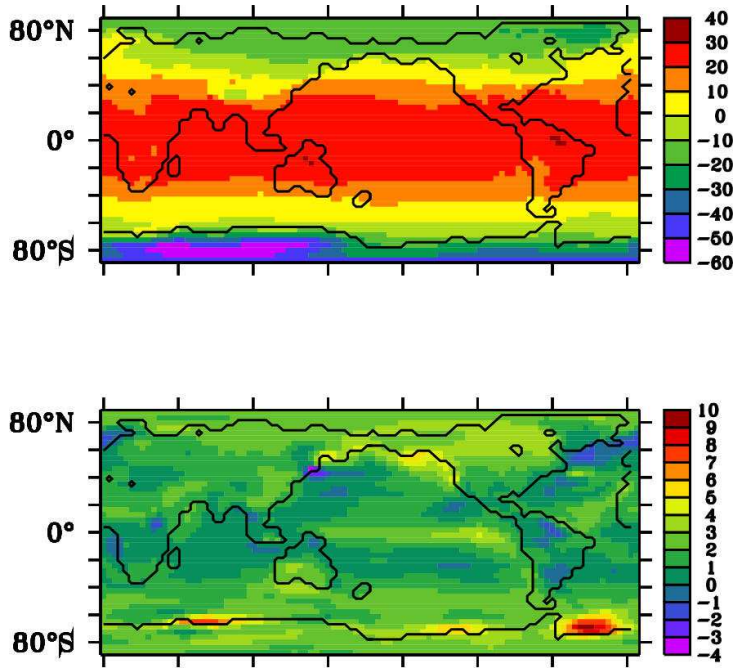

Figure 5.30: *Air surface temperature in °C in the coupled experiments for EXP0.1coup (top), difference EXP1coup - EXP0.1coup.*

a thickness of up to 2 m. In EXP1coup, the sea ice shows strong changes in the Arctic region and west of the Antarctic peninsula, with a reduction of between 1.5 m and 2.2 m. The increase in air temperature has a weaker impact in the reduction of the sea-ice cover, as the temperature stay well below freezing temperature. This reduction in sea-ice cover increase the input of freshwater in the high latitudes in the Atlantic ocean.

In the ocean only-experiments, the sea ice volume shows a decrease in all regions. The change occurs instantanously after the change in κ_b and stabilises straight afterwards. The freshwater input from the ice melting is only valid in a transient period but only the freshwatwer imput from precipitation at high latitudes follows the changes in the MOC as κ_v increases.

5.5.3 Atmospheric Transport

The heat and water fluxes show differences between the experiments; this can be in largly linked to the changes in the atmospheric energy transport and wind patterns, which can only change in the coupled experiments. The atmospheric energy

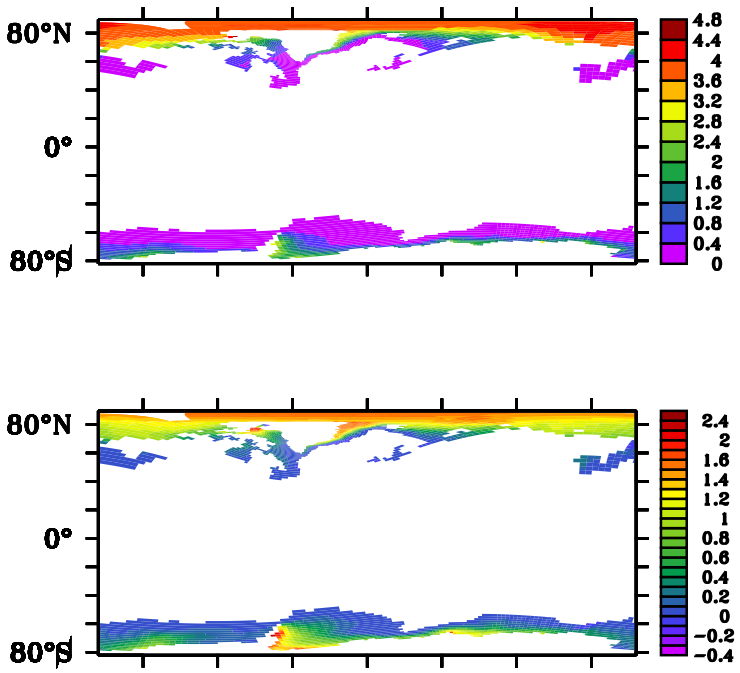

Figure 5.31: *Sea-ice thickness changes in metres in coupled experiments for EXP0.1coup (top), difference EXP1coup - EXP0.1coup.*

transport reduces in the Southern hemisphere and does not change in the Northern Hemisphere (figure 5.32). A change in atmospheric energy transport that compensates the change in ocean heat transport is only found in the Southern Hemisphere. In the Norhern Hemisphere, the energy transport in the atmosphere does not changes between EXP0.1coup and EXP1coup, but regional differences are observed in the surface air temperature. The Nordic Seas and north Atlantic region show a reduction of 2-3°C, the Pacific an increase of 5-6°C and the Arctic region an increase of 3-4°C. The decrease in temperature in the Nordic Seas and north Atlantic can be related to the decrease in ocean heat transport. Where the surface air temperature (SAT), reduces no changes in the sea ice is found but over the Arctic where the SAT is found to increase a continuous decrease of the sea ice is found.

The windstress in EXP0.1coup shows strong eastward windstress in the ACC regions. The trade winds in tropical regions are well reproduce. As κ_b increases, the windstress is found to reduce in the ACC region, in the Indian Ocean and high latitudes in the Atlantic and to increase in the tropical and high latitudes in the Pacific. The increase in windstress northward in the Pacific is responsible for the increase in the sea air temperature over the Arctic regions. The increases over the

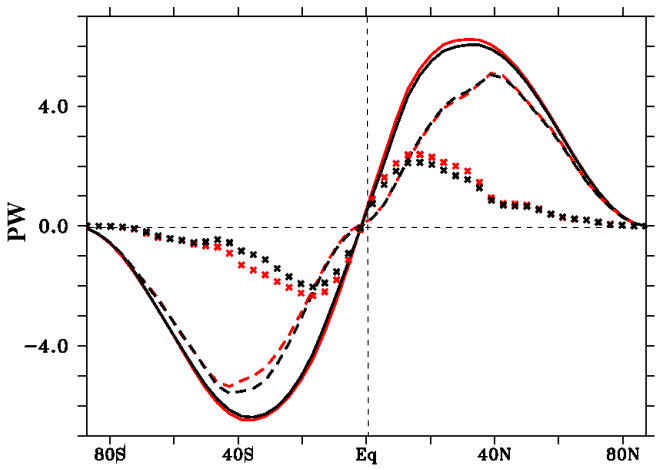

Figure 5.32: *In the coupled experiments, energy transport in PW for EXP0.1coup (black) and EXP1coup (red), total energy transport (solid line), atmospheric energy transport (dashed line) and ocean heat transport (crosses).*

eastern Pacific are correlated with the increased ocean heat transport and changes in the wind stress.

5.6 Discussion

The experiments look at the response to changes in κ_b in the state-of-the-art model: ECHAM5/MPI-OM. The ocean only experiments found similar behavior to previous studies, such as the FORTE experiments in Chapter 4. However, the fully coupled experiments show a reduction in the MOC in the Atlantic and an overturning cell appears in the Pacific as κ_b increases. The equatorial overturning cells are also increasing as κ_b increases. In the ocean-only experiments, this cannot be related to increase in the wind stress as the ocean model is forced by climatological wind stress forcing, but hence to a more diffuse thermocline which is also the case in the coupled experiments in regions with no deep convection.

A clear difference in the vertical mixing shows clear differences between the ocean and coupled experiments in the north Atlantic and Pacific is obseerved. We show

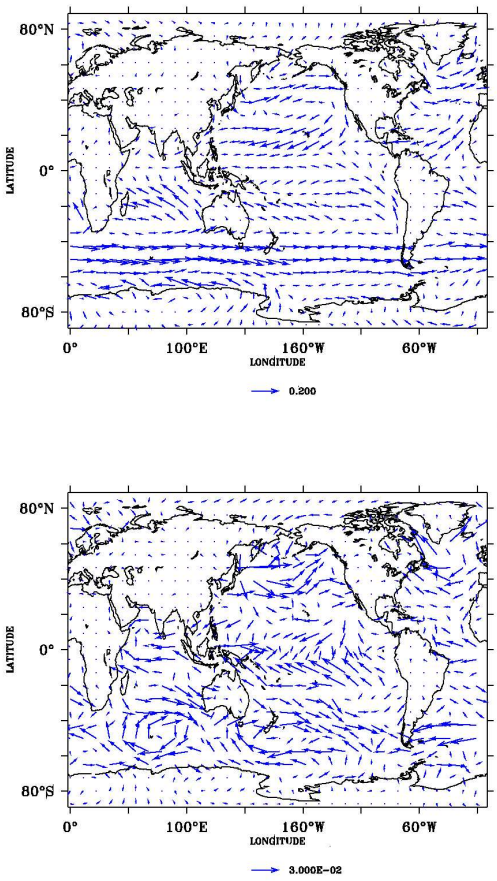

Figure 5.33: *Top: Windstress in EXP0.1coup in $N.m^{-2}$; Bottom: difference in windstress between EXP1coup and EXP0.1coup in $N.m^{-2}$.*

that most of the mixing comes from the convective component and patterns of mixing due to the $\kappa_v(PP - scheme)$ and $\kappa_v(convection)$ are very similar. As κ_b increases a reduction of the $\kappa_v(total)$ is found at the convection regions and no mixing coefficient is observed below 1000 m deep in the coupled experiments. The $\kappa_v(total)$ increases as κ_b increases in the ocean only experiments. The changes in the water properties and the stability of the water column affect both the $\kappa_v(convection)$ and $\kappa_v(PP-scheme)$ term and can explain the changes in the overturning in convection regions and their spatial similarities.

The strongest difference in water properties between the ocean-only and coupled experiments is the reduction in salinity and temperature at high latitudes in the Atlantic as κ_b increases. The changes in temperature are directly correlated to the changes in the heat transport. The strongest change is the freshening in the Arctic in the coupled experiments as κ_b increases; this is not related to the freshwater transport changes but to the atmospheric response to an increase in precipitation by 50-100%. The Pacific shows an increase in salinity in higher latitudes which is related to a reduction in the northward freshwater transport in the northern hemisphere and an increase of evaporation. In the ocean-only experiments, these feedbacks can not be observed as the SAT is prescribed. The strong freshening in the Arctic water as κ_b increases comes from an increase in the precipitations at high latitudes by 50 to 100% and sea ice melting. The changes in the precipitation at high latitudes are followed by similar changes in the MOC. Whereas the freshening by the se-ice is constant throughout the sensitivity experiments once κ_b has been changed.

The increase in precipitation over the Arctic should be enough to reduce the overturning in the North Atlantic once all the ice cover is gone. But this could only be verified by another 1000 years of integration. The sea ice model is a 0-layer model and passes the melting sea ice at the surface directly into the ocean. It is far from the complex dynamics and thermodynamics of the observed sea-ice. Observations show that the melting sea ice creates water ponds at the surface which creates a positive feedback by enhanced albedo effect. All of these processes are missing in the MPI-OM model; if they were included, they would produce a more rapid melting, but the impact on the ocean should be the same.

The experiments show the importance of the coupling and the feedbacks of the atmosphere on the ocean vertical mixing. This behavior should be further investigated with other coupled models.

5.7 Conclusions

1. The MOC in the Atlantic shows opposite behavior between the coupled and ocean only experiments. This behavior highlights the importance of the use of coupled ocean-atmosphere models.

2. The mixing shows opposite changes in strength as κ_b in the convection regions. The changes in the mixing is deminated by the convective mixing. Its changes, to increasing κ_b, is due to changes in the water masses at high latitudes.

3. The sea ice model is very sensitive to the changes in the surface air temperature and ocean heat lost. But it ssimplicity omits many feedbacks.

4. In the coupled experiments, the precipitation increases between 50 and 100% at high latitudes providing a constant freshwater input and reduction of the MOC.

Chapter 6

Conclusions and Future Work

The sensitivity experiments undertaken in this thesis are novel and many of the results found are unexpected and counter-intuitive. This work raises questions which will need further investigation.

6.1 Summary

In the first part, 8 experiments with different values of κ_v are conducted using the atmosphere-ocean coupled model FORTE. In common with previous studies (Bryan (1987), Wright and Stocker (1992) and Weber (1998)), the MOC in the Atlantic is found to increase with increasing κ_v as well as two recent studies with simple atmosphere coupled to OGCM ((Prange et al., 2003) and (Mignot et al., 2006)). Summing the contribution to the global MOC from each individual basin, global MOC strength is found to scale with κ_v with a power 0.4. The power law is not

found for each individual ocean basin but a compensation between the Atlantic and Pacific ocean is found. The increase in MOC in the Atlantic and Pacific oceans is associated with an increase in the ocean heat transport. The atmosphere responds to the change in the ocean state by a decrease of its energy transport and surface winds. Only a partial compensation is found between the changes in ocean and atmosphere heat transport (Bjerknes, 1964). Greater κ_v leads to a strong oceanic heat transport and energy transport. The strength of κ_v is found to have a strong impact on coupled phenomena, such as the cessation of El Niño at high values of κ_v.

In the second part, 6 experiments are undertaken, using the ocean only model MPI-OM or the coupled model ECHAM5/MPI-OM. The ocean model has a better representation of κ_v than that in FORTE model. The MPI-OM includes a PP-scheme, wind mixing, mixing by convection and a constant background mixing (κ_b). Only κ_b is changed, leaving the other components of the mixing to adjust freely. In the coupled model, the maximum strength of the MOC in the Atlantic shows a reduction by 16% as κ_b increases from 0.1 cm^2/s to 1 cm^2/s. This counter-intuitive behavior is not found when the experiment is reproduced with the ocean-only model. The reduction in MOC in the coupled model is found to be linked to a strong reduction in the convective mixing at high latitudes. The convective mixing is reduced by a strong freshening in the Arctic region due to an increase in surface air temperature and an increase in precipitation.

Two major difference are found between the FORTE and the ECHAM5/MPI-OM experiments as κ_v increases. Firstly, the overturning in the Atlantic is found to increase as κ_v increases in the FORTE experiments but not in the ECHAM5/MPI-OM. The main reason found for this difference is because of an freshwater input in the Arctic region and influence the convection occuring in the ECHAM5/MPI-OM. This freshwater input is due to changes in the atmospheric water transport and to the melting of the sea-ice cover. Secondly, the strong overturning circulation appears in the south Indo-Pacific ocean as κ_v increases in the FORTE model. This behaviour can be explain by the cessasion of the ENSO-phenomena and a reduction of the southward freshwater transport in the south Indo-Pacific ocean, which cause an increase in SSS and convection of water in the Admunsen Sea.

6.2 Discussion

6.2.1 Parameterisation of the vertical mixing

The choice of parameterisation of κ_v can varies from model to model, as with the two models used in this study. In FORTE, the vertical diffusivity has a constant value spatially and temporally over the entire ocean and cannot adjust to the changing atmospheric conditions; it is therefore rather crude. Information from the atmosphere is still seen by convection. When a water mass is unstable, it mixes with the water mass below in the next grid box. The constant κ_v in FORTE does not represent the spatial distribution of the values of the κ_v from observations and induces a bias in the value in some regions. For example, in the control run, $\kappa_v = 1$ cm^2/s, which is too high for the thermocline and ocean interior: observations suggest values of $\kappa_v = 0.1$ cm^2/s for these regions, and higher values than 1 cm$^2/s$ are observed near rough topography and at the surface Scott and Marotzke (2002). Also, in the FORTE experiment with $\kappa_v = 0.1$cm^2/s, this very small value does not allow the ocean to transmit surface signals the deeper levels, which cannot transfert heat to the deep and upwell dense water. This can explain the lack of overturning in this experiment.

Similar experiments are reproduced using the MPI-OM model. The MPI-OM model parameterised the mixing from the forcing due to the surface and to the breaking of internal waves. The MPI-OM model has a better representation of the mixing,which using the PP-scheme, mixing from the winds, mixing by convection and a small constant background mixing, κ_b. In the control run, mixing in the ocean interior is equal to 0.1cm^2/s (which is equal to κ_b), higher values are found in the model at the surface, in regions of convection and near rough topography. This formulation of the mixing agrees better with observations. However, it still omits many processes, such as capillary waves, tidal mixing, Langmuir circulations and boundary mixing which are other non-negligible sources of mixing. Today, only a few ocean-only models have tried to include tidal mixing. Simmons et al. (2004) tested the effect of the tidal energy budget on the MOC in a global ocean. Their energy flux estimates agreed well with independent estimated observations for generation sites for tidal energy. Such improvements are not yet available in global ocean GCMs, and are too numerically expensive.

Both models show difference in the mixing representation but that cannot explain by it self the opposite response of the overturning circulation in the Atlantic. The

strongest changes in the total mixing in the ECHAM5/MPI-OM experiments as κ_b increases come from the convective mixing. The FORTE model also has a convective adjustment but it atmosphere has responed differently to increasing κ_b.

6.2.2 Coupled Models

The coupled and ocean-only experiments using ECHAM5/MPI-OM highlight the importance of the coupling in these sensitivity experiments. In fact, the same experiments with or without the atmosphere give opposite response of the Atlantic MOC to increasing κ_b. In the coupled experiments, the surface air temperature changes as κ_b increases, which affects the cryosphere,the atmospheric circulation and ocean water masses and thus ocean circulation. This indirect effect of the mixing on the ocean circulation is not possible with the ocean model experiments forced by climatology.

FORTE and ECHAM5/MPI-OM are both coupled models and the MOC strengths in the two models show many similarities as κ_b increases. In both models, a reduction of the sea-ice and snow and freshening of the Arctic water are found, as well as an increase in surface air temperatures above the Arctic region. Both models also show convection in the Pacific for high values of κ_b, but the main difference is the response in the Atlantic and south Indo-Pacific. An opposite response of the MOC strength in the Atlantic ocean is observed. In ECHAM5/MPI-OM, the changes occur in the water masses in the Arctic region, where very strong changes in the convection are found. In FORTE, a freshening is also found by melting of the sea-ice and snow at high latitudes but the convection regions are located in the North Atlantic. The input of freshwater and the reduction of the overturning in the Atlantic should not be only a transient behaviour but also in the steady state. In both models, the atmospheric circulation changes which affects the water cycles. In the FORTE experiments, as κ_v increases, the freshwater fluxes change mainly in the equatorial and tropical regions. In the ECHAM5/MPI-OM experiments, the freshwater fluxes changes mainly at high latitudes contributing to a continous input of freshwater in the convection regions. The freshwater input from increasing precipitation as κ_v increases and sea-ice input by melting cannot be seperated from one to the other but the increased precipitation at high latitudes is only found in the ECHAM5/MPI-OM experiments and could be responsible for the difference in

response in the overturning circulation in the Atlantic to increasing κ_v. As well as the difference in the location of deep convection and their relative changes, similar to processes seen in Mignot et al. (2006) and Lucas et al. (2006). Another difference in the response in the MOC to increasing κ_v is found on the south Indo-Pacific. In FORTE, a strong overturning appears as κ_v increases. This response is linked to the changes in the ENSO-phenomena, which decrease southward freshwater transport and a decrease in the precipitation above the Admunsen Sea. This coupled changes are not observed with the ECHAM5/MPI-OM model.

6.2.3 Model Resolution

Both models used have a coarse resolution (for the atmosphere T21 in FORTE and T31 in ECHAM5 and for the ocean $4°\times4°$ in FORTE and $3.25°\times3.25°$ for MPI-OM), and FORTE uses flux adjustments to obtain a realistic reference climate. Neither model can explicitly represent mesoscale eddies and have to use a parameterisation such as the Gent-McWilliams one (Redi, 1982; Gent and McWilliams, 1990; Gent et al., 1995). Many regions of upwelling, convection, overflows or straits are only represented by few grid cells, which can bias the results observed in the studies. For example, the equatorial Pacific where the El Niño phenomenon takes place is only represented by 3-4 grids cells in the meridional direction, which creates a cold bias on the eastern side and exaggerates the extent of the cold tongue. Atmospheric properties such as the meridional transport and jet stream are better represented at resolutions higher than T21 (Boyles, 1993). ECHAM5 has a T31 resolution, which is able to reproduce well many of the atmospheric processes (Roeckner et al., 2006).

The Arctic region show a strong response to the changes in the diapycnal mixing. Both models used a very simple parameterisation of the sea ice, which does not contain some internal dynamics. In FORTE, the freshwater fluxes are directly passed onto the ocean and cannot be stored as sea-ice above the ocean. In the MPI-OM model, the freshwater can built up some ice but still remains very simple. The sea-ice model is omitting many of the complex dynamics and thermodynamics of observed sea-ice such as multi layer model, water melting at the surface. The vertical ocean resolution does not allow the formation of a freshwater cap over the Arctic region when sea-ice is melting. The freshwater will be distribute in the first ocean grid box and then mixed downward.

6.3 Conclusions

1. The MOC-κ_ν scaling found analytically does not hold for the individual basins. A scaling is found for κ_v>$1cm^2/s$, but not with the predicted exponent, except in the South Atlantic. The South Atlantic and North Indo-Pacific overturning cells are more sensitive to κ_ν than the ones in the north Atlantic and South Indo-Pacific. The global overturning shows a very robust scaling power suggesting that the advection-diffusion holds for the global overturning and not for the Atlantic ocean only. This could explain why compensation between basins is found.

2. The power law scaling between κ_v and the MOC is not found using the state-of-the-art coupled model ECHAM5/MPI-OM. Nevertheless, it is found in FORTE for the global MOC, which scales with $\psi \propto \kappa_\nu^{0.4}$.

3. The existence of ENSO-like phenomena depends of the strength of κ_ν: it disappears for high values of κ_ν with the FORTE model. It suggests that it is linked to the apparition of a strong overturning in the south Indo-Pacific ocean.

4. The MOC in the Atlantic shows opposite response to increasing mixing between the coupled ECHAM5/MPI-OM and ocean-only MPI-OM experiments. This behavior highlights the importance of the use of coupled ocean-atmosphere models in sensitivity studies.

5. Both coupled models show a high sensitivity of the sea ice model, due to the changes in the surface air temperature. The freshwater input from the ice melting has a strong impact on the water masses below it and the ocean circulation. The ECHAM5/MPI-OM model shows in addition an increase in the precipitation over the Nordic, Labrador Seas and Arctic Ocean. The impact of the freshening is found to be different according to the location of the deep convection, which plays an important role in the changes in the strength of the MOC.

6. The Bjerknes compensation is only partially found in the FORTE model.

7. The diapycnal mixing and the ocean-atmosphere interactions both control the strength of the MOC, and their influences cannot be considered separately.

6.4 Future Work

This study looks at the response of the climate system to parameterisations of the ocean mixing. So far all previous studies showed an increase in the overturning circulation as the vertical diffusivity is increased. The findings with the coupled ECHAM5/MPI-OM are the first to find a decrease of the MOC in the Atlantic for increasing κ_v; the difference between FORTE and MPI-OM suggest that the coupled system is very sensitive to the mixing parameterisation and its ocean response. This study is a step towards the use of more complex models in sensitivity studies to ocean parameters.

Fisrtly, the use of the Gent-McWilliams parameterisations for mesoscales eddies (Redi, 1982; Gent and McWilliams, 1990; Gent et al., 1995) allows a reduction of the vertical exchanges compare to the horizontal/vertical parameterisation. As computer power will increase higher resolution models can be used and avoid the use of this parameterisation and resolve the mesoscales eddies.

Secondly, the parameterisations do not represent the mixing explicitly and omits some potentially important processes, such as double diffusion, tidal mixing, Langmuir circulation and boundary mixing, which are not represented in the models used. Few ocean only models formulate mixing by tides (Simmons et al., 2004).

In the past, parameterisation for all these small scales processes can be included in coupled models, the diapycnal mixing can be prescribed in the model as a 3-D field. In our experiments, the background diffusivity is constant spatially and temporally but exponential profiles of the vertical mixing are more realistic and can be used as well as using a global distribution map such as proposed by Hibiya et al. (2006).

Another important behaviour highlighted by the timeserie of the MOC in the Altantic in the ECHAM5/MPI-OM experiments is the adjustment time. If one only consider the first 10 years of the timeseries, we can conclude that the MOC in the Atlantic increases as κ_v increases, which is not the case afterwards. If futher experiments will have to be carried out or if a model have to be tested or tuned in relation to its κ_v value, it has to be run for few decades until it adjusts.

Nowadays, models are getting more complex, aiming to create an Earth system model which will incorporate all elements of the climate system for the purpose of

predicting future climate change. Mixing parameterisations in future Earth system models should be more realistic as the computer power will increase and the sensitivity of Earth system model tested to gain faith in the outputs of the climate models and their prediction for future climate changes.

Bibliography

R.B. Alley, J. Marotzke, W.D. Nordhaus, J.T. Overpeck, D.M. Peteet, R.A. Pielke Jr., R.T. Pierrehumbert, P.B. Rhines, T.F. Stocker, L.D. Talley, and J.W. Wallace. Abrupt climate change. *Science*, 299(5615):2005–2010, 2003.

A. Arakawa. Computational design for long-term numerical integration of the equation of fluid motion: two-dimensional incompressible flow. Part I. *J. of Comp.Fluid Dyn.*, 1:119–143, 1966.

A. Arakawa and V.R. Lamb. Computational design of the basic dynamical processes of the UCLA general circulation model. *Methods Comput. Phys.*, 17:173–265, 1977.

L. Armi. Some evidence for boundary mixing in the deep ocean. *J. Geophys. Res*, 83(C4):1971–1979, 1978.

E.D. Barton and A.E Hill. Abyssal flow through the Amirante Trench (Western Indian Ocean). *Deep Sea Res. A*, 36:1121–1126, 1989.

A. Betts. A new convective adjustment scheme 1. Observational and theoretical basis. *Quaterly Journal of the Royal Meteorological Society*, 112:667–691, 1986.

J. Bjerknes. *Atlantic air-sea interaction*, volume 10, pages 1–82. Advances in Geophysics, 1964.

J.S. Boyles. Sensitivity of dynamical quantities to horizontal resolution for a climate simulation using the ECMWF (cycle 33) model. *J. Climate*, 6:796–815, 1993.

W.S. Broecker. The great ocean conveyor. *Oceanography*, 4:79–89, 1991.

W.S. Broecker. Thermohaline circulation, the achilles heel of our climate system: Will man-made CO_2 upset the balance? *Science*, 278:1582–1588, 1997.

W.S. Broecker, D.M. Peteet, and D. Rind. Does the ocean-atmosphere system have more than one stable mode of operation? *Nature*, 315:218–220, 1985.

F. Bryan. Parameter Sensitivity of Primitive Equation Ocean General Circulation Models. *J. Phys. Oceanogr.*, 17:970–985, 1987.

K Bryan. A numerical method for the study of the circulation of the world ocean. *Journal Computational Physics*, 4(3):347–376, 1969.

H.L. Bryden and S. Imawaki. *Ocean circulation and climate*, volume 10, chapter Ocean heat transport, pages 474–495. eds. Siedler, G. and Church, J. and Gould, J., Advances in Geophysics edition, 2001.

J.M. Campin and H. Goosse. Parameterization of density-driven downsloping flow for a coarse-resolution ocean model in z-coordinate. *Tellus*, 51A:412 – 430, 1999.

A. Clement and R. Seager. Climate and the tropical oceans. *J. Climate*, 12:3383–3401, 1999.

A. Colin de Verdiere. *Modelling Oceanic Climate Interactions*, chapter On the oceanic thermohaline circulation, pages 151–183. Willebrand, J. and Anderson, D.L.T., 1993.

M. Conkright, S. Levitus, T. O'Brien, C. Stephens, D. Johnson, O. Baranova, J. Antonov, R. Gelfeld, J. Rochester, and C. Fory. *World Ocean Atlas 1998*. National Oceanographic Data Center, 1998.

Coupled Model Intercomparison Project, CMIP.
http://www-pcmdi.llnl.gov/modeldoc/cmip/table3.html.

M. Cox. A primitive equation, 3-dimensional model of the ocean. Tech. Rep. 1, Geophysical Fluid Dynamics Laboratory/NOAA, Princeton University, 1984.

U. Cubasch, G.A. Meehl, G.J. Boer, R.J. Stouffer, M. Dix, A. Noda, S. Senior, C.A. Raper, and K.S. Yap. *Climate Change 2001: The Scientific Basis*, chapter Projections of future climate change, pages 525–582. eds. J.T. Houghton and Ding, Y. and Griggs, D.J. and Noguer, M. and van der Linden, P. and Maskell, K. and Johnson, C.I., 2001.

A. Czaja and J. Marshall. The Partitioning of Poleward Heat Transport between the Atmosphere and Ocean. *Journal of the Atmospheric Sciences*, 63:1498–1511, 2006.

F. Dalan, P.H. Stone, I. Kamenkovich, and J. Scott. Sensitivity of the Ocean's Climate to Diapycnal Diffusivity in an EMIC. Part I: Equilibrium State. *J. Climate*, 18:2460–2481, 2005.

G. Danabasoglu and J.C. McWilliams. Sensitivity of the global ocean circulation to parameterizations of mesoscale tracer transports. *J. Climate*, 8:2967–2987, 1995.

A. Defant. *Physical Oceanography*, volume 1. New York: Pergamon, 1961.

T.L. Delworth and R.J. Greatbatch. Multidecadal thermohaline circulation variability driven by atmospheric surface flux forcing. *J. Climate*, 13:1481–1495, 2000.

T.L. Delworth, S. Manabe, and R.J. Stouffer. Interdecadal variations of the thermohaline circulation in a coupled ocean-atmosphere model. *J. Climate*, 6:1993–2011, 1993.

X. Durrieu de Madron and G. Weatherly. Circulation, transport and bottom boundary layers of the deep currents in the Brazil Basin. *J. Mar. Res.*, 52:583–638, 1994.

G.D. Egbert and R.D. Ray. Significant dissipation of tidal energy in the deep ocean inferred from satellite altimeter data. *Nature*, 405:775–778, 2000.

K. Emanuel. Contribution of tropical cyclones to meridional heat transport by the oceans. *Geophys. Res. Lett.*, 106:14771–14781, 2001.

B. Ferron, H. Mercier, K.G. Speer, A.E. Gargett, and K.L. Polzin. Mixing in the Romanche Facture Zone. *J. Phys. Oceanogr.*, 28:1929–1945, 1998.

P.M. Forster, M. Blackburn, R. Glover, and K.P. Shine. An examination of climate sensitivity for idealised climate change experiments in an intermediate general circulation model. *Climate Dynamics*, 16:833–849, 2000.

T. Furevik, M. Bentsen, H. Drange, I. Kindem, N. Kvamstø, and A. Sorteberg. Description and evaluation of the Bergen climate model: ARPEGE coupled with MICOM. *Climate Dynamics*, 21:27–51, 2003.

A. Ganachaud and C. Wunsch. Improved estimated of global ocean circulation, heat transport and mixing from hydrographic data. *Nature*, 408:453–456, 2000.

P. Gent and J. McWilliams. Isopycnal mixing in ocean circulation models. *J. Phys. Oceanogr.*, 20:150–155, 1990.

P. Gent, J. Willebrand, T. McDougall, and J. McWilliams. Parameterizing eddy-induced transports in ocean circulation models. *J. Phys. Oceanogr.*, 25:463–474, 1995.

J.K. Gibson, P. Kållberg, S. Uppala, A. Hernandez, A. Nomura, and E. Serrano. ERA description. ECMWF Re-analysis Proj. Rep. Ser. 1, European Centre for Medium-Range Weather Forecast, Reading, England, 1997.

A.E. Gill. *Atmosphere-Ocean Dynamics*. Academic Press, 1982.

A. Gnanadesikan. A simple predictive model for the structure of the oceanic pycnocline. *Science*, 283:2077–2079, 1999.

A.L. Gordon. Interocean exchange of thermocline water. *J. Geophys. Res.*, 91: 5037–5046, 1986.

W.M. Gray. Atlantic seasonal hurricane frequency, part I. El Niño and 30 mb quasi-biennal oscillation influences. *Mon. Weather Rev.*, 112:1649–1668, 1984a.

S.M. Griffies, C. Boening, F.O. Bryan, E.P. Chassignet, R. Gerdes, H. Hasumi, A. Hirst, A-M. Treguier, and D. Webb. Developments in ocean climate modelling. *Ocean Modelling*, 2:123–192, 2000.

S.M. Griffies, R.C. Pacanowski, M. Schmidt, and V. Balaji. Tracer Conservation with an Explicit Free Surface Method for z-Coordinate Ocean Models . *Monthly Weather Review*, 129(5):1081–1098, 2001.

S. Hellerman and M. Rosenstein. Normal monthly wind stress over the world ocean with error estimates. *J. Phys. Oceanogr.*, 13:1093–1104, 1983.

K.J. Heywood, A.C. Naveira Garabato, and D.P. Stevens. High mixing rates in the abyssal Southern Ocean . *Nature*, 415:1011–1014, 2002.

T. Hibiya, M. Nagasawa, and Y. Niwa. Global mapping of diapycnal diffusivity in the deep based on the results of expendable profiler (XCP) surveys. *Geophys. Res. Lett.*, 33:L03611, 2006.

W.D. Hibler III. A dynamic thermodynamic sea ice model. *J. Phys. Oceanogr.*, 9: 815–846, 1979.

N.G. Hogg, P. Biscaye, W. Gardner, and W.J. Schmitz. On the transport and modification of the Antarctic Bottom water in the Vema Channel. *J. Mar. Res.*, 40(Suppl.):231–263, 1982.

B.J. Hoskins. A multi-layer spectral model and the semi-implicit method. *Quart. J. R. Met. Soc.*, 101:637–655, 1975.

J.T. Houghton, L.G. Meira Filho, B.A. Callander, N. Harris, A. Kattenberg, and K. Maskell. *Climate Change 1995: The scinece of Climate Change. Contribution of the Working Group I to the Second Assessment Report of the Intergovernmental Panel on Climate Change*. IPCC, Cambridge University Press edition, 1996.

R.X. Huang. Mixing and Energetics of the Oceanic Thermohaline Circulation. *J. Phys. Oceanogr.*, 29:727–746, 1999.

J.W. Hurrell, Y. Kushnir, G. Ottersen, and M. Visbeck. *The North Atlantic Oscillation*, volume 134. Geophysical Monograph Series, 2003a.

J.W. Hurrell, Y. Kushnir, G. Ottersen, and M. Visbeck. *The North Atlantic Oscillation Climate Significance and Environmental Impacts*. Geophysical Monograph Series, 2003b.

D. Jacob, H. Goettel, J. Jungclaus, M. Muskulus, Podzun, and J. Marotzke. Slowdown of the thermohaline circulation causes enhanced maritime climate influence and snow cover over europe. *Geophys. Res. Lett.*, 32:L21711, 2005.

H.W. Jeffreys. On fluid motions produced by differences of temperature and humidity. *Q. J. R. Meteorol. Soc.*, 51:347–356, 1925.

J.H. Jungclaus, H. Haak, M. Latif, and U. Mikolajewicz. Artic-North Atlantic Interactions and Multidecadal Variability of the Meridional Overturning Circulation. *J. Climate*, 18(19):4013–4031, 2005.

I.V. Kamenkovich and E.S. Sarachik. Mechanisms Controlling the Sensitivity of the Atlantic Thermohaline Circulation to the Parameterization of Eddy Transports in Ocean GCMs. *J. Phys. Oceanogr.*, 34:1628–1647, 2004.

B.A. Klinger, S. Drijfhout, J. Marotzke, and J.R. Scott. Sensitivity of Basin-wide Meridional Overturning to Diapycnal Diffusion and Remote Wind Forcing in an Idealized Atlantic-Southern Ocean Geometry. *J. Phys. Oceanogr.*, 33:249–266, 2003.

J.R. Ledwell, E.T. Montgomery, K.L. Polzin, L.C. St. Laurent, R.W. Schmitt, and J.M. Toole. Evidence for enhanced mixing over rough topography in the abyssal ocean. *Nature*, 403:179–182, 2000.

J.R. Ledwell, A.J. Watson, and C.J. Law. Evidence for slow mixing across the pycnocline from an open-ocean tracer release experiment. *Nature*, 364:701–703, 1993.

S. Levitus. *World Ocean Atlas*. National Oceanography Data Center, 1998.

M.A. Lucas, J.J. Hirschi, and J. Marotzke. The scaling of the meridional overturning with the meridional temperature gradient in idealised general circulation models. *Ocean Modelling*, 13:306–318, 2006.

S. Manabe, K. Bryan, and M.J. Spelman. A global ocean-atmosphere climate model. Part I. The atmospheric circulation. *J. Phys. Oceanogr.*, 5:3–29, 1975.

S. Manabe and R.J. Stouffer. Two stable equilibria of a coupled ocean-atmosphere model. *J. Climate*, 1:841–866, 1988.

S. Manabe and R.J. Stouffer. Multiple-century response of a coupled ocean-atmosphere model to increase of atmospheric carbon dioxide. *J. Climate*, 7(1): 5–23, 1994.

J. Marotzke. Influence of convective adjustment on the stability of the thermohaline circulation. *J. Phys. Oceanogr.*, 21:903–907, 1991.

J. Marotzke. Boundary mixing and the dynamics of three-dimensional thermohaline circulations. *J. Phys. Oceanogr.*, 27:1713–1728, 1997.

J. Marotzke and P. Stone. Atmospheric transport, the thermohaline circulation, and flux adjustments in a simple coupled model. *J. Phys. Oceanogr.*, 25:1350–1364, 1995.

J. Marshall and F. Schott. Open-ocean convection: Observations, theory, and models. *Rev. of Geophys.*, 1999.

S.J. Marsland, H. Haak, J.H. Jungclaus, M. Latif, and F. Roeske. The Max-Planck-Institute global ocean/sea ice model with orthogonal curvilinear coordinates. *Ocean Modelling*, 5:91 – 127, 2003.

M.C. McCarthy, L.D. Talley, and M.O. Baringer. Deep upwelling and diffusivity in the southern central Indian basin. *Geophys. Res. Lett.*, 24:2801–2804, 1997.

J.F. McManus, R. Francois, J.-M. Gherardi, L.D. Keigwin, and S. Brown-Leger. Collapse and rapid resumption of Atlantic meridional circulation linked to deglacial climate changes. *Nature*, 428:834–837, 2004.

F. Mesinger and A Arakawa. Numerical methods used in atmospheric models, Vol.I. JOC. Technical Report 17, World Meteorological Organisation, 1976.

J. Mignot, A. Levermann, and A. Griesel. A decomposition of the Atlantic Meridional Overturning Circulation into physical components using its sensitivity to vertical diffusivity. *J. Phys. Oceanogr.*, 36:636–650, 2006.

M.Y. Morris, M.M. Hall, L.C. St Laurent, and N.G. Hogg. Abyssal mixing in the Brazil Basin. *J. Phys. Oceanogr.*, 31:3331–3348, 2001.

W.H. Munk. Abyssal recipes. *Deep-Sea Research*, 13:707–730, 1966.

W.H. Munk and C. Wunsch. Abyssal recipes II: energetics or tidal and wind mixing. *Deep-Sea Research*, 45:1977–2010, 1998.

A.C. Naveira Garabato, K.L. Polzin, B.A. King, K.J. Heywood, and M. Visbeck. Widespread Intense Turbulent Mixing in the Southern Ocean. *Science*, 303:210–213, 2004.

J. Nilsson. Mixing in the ocean produced by tropical cyclones. *Tellus*, 48A:342–355, 1996.

R.C. Pacanowski and S.M. Griffies. *MOM 3.0 Manual*. NOAA/Geophysical Fluid Dynamics Laboratory, Princeton USA, 1998.

R.C. Pacanowski and S.G.H. Philander. Parameterization of vertical mixing in numerical-models of tropical oceans. *J. Phys. Oceanogr.*, 11:1443–1451, 1981.

W. Park and M. Latif. Ocean Dynamics and the Nature of Air-Sea Interactions over the North Atlantic at Decadal Times Scales. *J. Climate*, 18:982–995, 2005.

Y.G. Park and K. Bryan. Comparison of Thermally Driven Circulations from a Depth-Coordinate Model and an Isopycnal-Layer Model. Part I: Scaling-Law Sensitivity to Vertical Diffusivity. *J. Phys. Oceanogr.*, 30(3):590–605, 2000.

S.G.H. Philander. *El Niño, La Niña and the Southern Oscillation*. Academic Press, 1990.

H. Pohlmann, F. Sienz, and M. Latif. Influence of the multidecadal Atlantic meridional overturning circulation variability on European climate. *J. Climate*, accepted, 2006.

K.L. Polzin, J.M. Toole, J.R. Ledwell, and R.W. Schmitt. Spatial variability of turbulent mixing in the abyssal ocean. *Science*, 276:93–96, 1997.

M. Prange, G. Lohmann, and A. Paul. Influence of Vertical Mixing on the Thermohaline Hysteresis: Analyses of an OGCM. *J. Phys. Oceanogr.*, 33:1707–1721, 2003.

J.F. Price and M. Baringer. Outflows and deep water productions by marginal seas. *Prog. Oceanogr.*, 25:162–200, 1994.

M.H. Redi. Oceanic isopycnal mixing by coordinate rotation. *J. Phys. Oceanogr.*, 12:1154–1158, 1982.

A. Robinson and H. Stommel. The oceanic thermocline and the associated thermohaline circulation. *Tellus*, 3:295–308, 1959.

E. Roeckner, K. Arpe, L. Bengtsson, M. Christoph, M. Claussen, L. Duemenil, M Esch, M. Giorgetta, U. Schlese, and U. Schulzweida. The atmospheric general circulation model ECHAM-4: Model description and simulation of present climate. Report 218, Max-Planck-Institute fuer Meteorlogie, 1996.

E. Roeckner, G. Baeuml, L. Bonaventura, R. Brokopf, M. Esch, M. Giorgetta, S. Hagemann, I. Kirchner, L. Kornblueh, E. Manzini, A. Rhodin, U. Schlese, U. Schulzweida, and A. Tompkins. The atmospheric general circulation model ECHAM5: Model description. Report 349, Max-Planck-Institute fuer Meteorlogie, 2003.

E. Roeckner, R. Brokopf, M. Esch, M. Giorgetta, S. Hagemann, L. Kornblueh, E. Manzini, U. Schlese, and U. schulzweida. Sensitivity of simulated Climate to Horizontal and Vertical Resolution in the ECHAM5 Atmosphere Model. *J. Climate*, 19:3771–37191, 2006.

D. Roemmich, S. Huatala, and D. Rudnick. Northward abyssal transport through the Samoan Passage and adjacent regions. *J. Geophys. Res*, 101:14039–14055, 1996.

F. Röske. An atlas of surface fluxes based on the ECMWF Re-analysis - a climatological dataset to force global ocean circulation models. Technical Report 323, MPI Hamburg, 2001.

J.W. Sandström. Dynamische Versuche mit Meerwasser. *Annal. Hydrogr. Marit. Meteorol.*, 36:6–23, 1908.

J.W. Sandström. Meteorologische Studien in Schwedischen Hochgebirge. *Goteborgs Kungl. Vensk. Vitterh.-Samh. Handingar*, 27:1–48, 1916.

P.M. Saunders. Flow through discovery gap. *J. Phys. Oceanogr.*, 17:631–643, 1987.

R. Sausen, K. Barthel, and K. Hasselmann. Coupled ocean-atmosphere models with flux correction. *Climate Dynamics*, 2:145–163, 1988.

R. Sausen and R. Voss. Techniques for asynchronous and periodically synchronous coupling of atmosphere and ocean models. *Climate Dynamics*, 12:313–323, 1996.

W.J. Schmitz. On the world ocean circulation: volumes I and II. Technical Report WHOI-96-08, Woods Hole Oceanographic Institution, 1996.

J.R. Scott. *The Role of Mixing and Geothermal Heating and Surface Buoyancy Forcing in Ocean Meridional Overturning Dynamics*. PhD thesis, MIT, Department of Earth, Atmospheric and Planetary Sciences, 2000.

J.R. Scott and J. Marotzke. The location of diapycnal mixing and the meridional overturning circulation. *J. Phys. Oceanogr.*, 32:3578–3595, 2002.

A.J. Semtner. An oceanic general circulation model with bottom topography. Technical Report 9, Dept of Meteorolgy, UCLA, Los Angeles, CA 90095, U.S.A., 1974.

L. Shaffrey and R. Sutton. The Interannual Variability of Energy Transports within and over the Atlantic Ocean in a coupled Climate Model. *J. Climate*, 17:1433–1448, 2004.

L. Shaffrey and R. Sutton. Bjerknes Compensation and the Decadal Variability of the Energy Transports in a coupled Climate Model. *J. Climate*, 19:1167–1181, 2006.

A.J. Simmons, D.M. Burridge, M. Jarraud, C. Girard, and W. Wergen. The ECMWF medium-range prediction model: Development of the numerical formulations and the impact of increased resolution. *Meteorol. Atmos. Phys.*, 40: 28–40, 1989.

H.L. Simmons, S.R. Jayne, L.C. St. Laurent, and A.J. Weaver. Tidally driven mixing in a numerical model of the ocean general circulation. *Ocean Modelling*, 6:245–263, 2004.

B. Sinha and R. Smith. Development of a fast Coupled General Circulation Model (FORTE) for climate studies, implemented using the OASIS coupler. Internal Document No.81, Southampton Oceanography Centre, 2002.

J. Slingo. The development and verification of a cloud prediction scheme for the ECMWF model. *Quaterly Journal of the Royal Meteorological Society*, 113:899–927, 1987.

R.S. Smith. *Ocean circulation and climate dynamics under idealised continental configurations in a coupled ocean-atmosphere model*. PhD thesis, University of Southampton, 2004.

R.S. Smith, C. Dubois, and J. Marotzke. Global Climate and ocean circulation on an aquaplanet AOGCM. *J. Climate*, accepted, 2006.

H. Stommel. The westward intensification of wind-driven ocean currents. *Trans. Amer. Geophys. Union*, 29:202–206, 1948.

H. Stommel. Thermohaline convection with two stables regime of flow. *Tellus*, 13: 224–230, 1961.

P.H. Stone. Constraints on dynamical transports of energy on a spherical planet. *Dynamics of Atmospheres and Oceans*, 2:123–139, 1978.

H.U. Sverdrup. Wind-driven currents in a baroclinic ocean; with application to the equatorial currents of the eastern Pacific. *Proc. Nat. Acad. Sci. Wash*, 33:318–326, 1947.

L.D. Talley. Shallow, intermediate, and deep overturning components of the global heat budget. *J. Phys. Oceanogr.*, 20:1648–1760, 2003.

L. Terray, S. Valcke, and A. Piacentini. OASIS 2.2, Ocean atmosphere sea ice soil user's guide and reference manual. Technical Report TR/CGMC/98-05, CERFACS, Toulouse, 1998.

L. Terray, S. Valcke, and A. Piacentini. OASIS 2.3 user's guide. Technical Report TR/CGM/99-37, CERFACS, Toulouse, 1999.

J.R. Toggweiler and B. Samuels. Effects of Drake Passage on the global thermohaline circulation. *Deep-Sea Research*, 42(4):477–500, 1995.

J.R. Toggweiler and B. Samuels. On the ocean's large-scale circulation near the limit of no vertical mixing. *J. Phys. Oceanogr.*, 28:1832–1852, 1998.

J. Toole and T.J. McDougall. *Ocean Circulation and Climate*, chapter Stirring and mixing in the ocean interior, pages 337–356. Academic Press, 2001.

J.M. Toole, K.L. Polzin, and R.W. Schmitt. Estimates of diapycnal mixing in the abyssal ocean. *Science*, 264:1120–1123, 1994.

K.E. Trenberth and J.M. Caron. Estimates of meridional atmosphere and ocean heat transport. *J. Climate*, 14:3433–3443, 2001.

H. Tsujino and N. Suginohara. Thermohaline Circulation Enhanced by Wind Forcing. *J. Climate*, 14:3433–3443, 2001.

UNESCO. Algorithms for computation of fundamental properties of seawater. Technical Papers in Marine Science 44, UNESCO, 1983.

M. Vellinga and R.A. Wood. Global climatic impacts of a collapse of the Atlantic Thermohaline Circulation. *Climatic change*, 54:251–267, 2002.

G. Veronis. *The role of models in tracer studies. Numerical Models of the Ocean Circulation.* National Academy of Sciences, 1975.

B.A. Warren. Why is no deep water formed in the North Pacific? *J. Marine Res.*, 41:327–347, 1983.

A.J. Weaver and T.M.C. Hughes. On the incompatibility of ocean and atmosphere models and the need for flux adjustments. *Climate Dynamics*, 12:141–170, 1996.

D.J. Webb. An ocean model code for array processor computers. *Computers and Geosciences*, 22(5):569–578, 1996.

D.J. Webb and N. Suginohara. Vertical mixing in the deep ocean. *Nature*, 409:37, 2001.

S.L. Weber. Parameter sensitivity of a coupled atmosphere-ocean model. *Climate Dynamics*, 14:201–212, 1998.

P. Welander. The thermocline problem. *Philosophical Transactions of the Royal Society of London. Series A, Mathematical and Physical Sciences*, 270:415–421, 1971.

N.C. Wells. *The Atmosphere and Ocean: A Physical Introduction.* John Wiley and Sons, 1997.

P. Wetzel, H. Haak, J. Jungclaus, and E. Maier-Reimer. The Max-Planck-Institute Global Ocean/Sea-Ice Model MPI-OM. Internal Document, Max-Planck-Institute for Meteorology, 2005.

J.A. Whitehead and L.V. Worthington. The flux and mixing rates of Antarctic Bottom Water within the North Atlantic. *J. Geophys. Res*, 87:7903–7924, 1982.

D.G. Wright and T.F Stocker. Sensitivities of a zonally averaged global ocean circulation model. *J. Geophys. Res*, 97:12707–12730, 1992.

C. Wunsch. The work done by the wind on the oceanic general circulation. *J. Phys. Oceanogr.*, 28:2331–2339, 1998.

C. Wunsch. What is the thermohaline circulation. *Science*, 298:1179–1181, 2002.

C. Wunsch and R. Ferrari. Vertical mixing, energy, and the general circulation of the oceans. *Annu. Rev. Fluid Mech.*, 36:281–314, 2004.

J. Zhang, R.W. Schmitt, and R.X. Huang. The relative influence of diapycnal mixing and hydrological forcing on the stability of the thermohaline circulation. *J. Phys. Oceanogr.*, 29(6):1096–1108, 1999.